UCLouvain

École polytechnique de Louvain

Operational modal analysis and seismic assessment of a tall brick chimney

Author: **Loïck Rosière**
Supervisors: **Prof. João Saraiva Esteves Pacheco De Almeida, Prof. Alexandre Costa**
Readers: **Alex Bertholet, Catherine Doneux, Ryan Hoult**
Academic year 2021–2022
Master [120] in Civil Engineering

"All models are wrong, but some are useful."

George E. P. Box

Abstract

In Western Europe, masonry chimneys were widely used in industrial settings during the 19th century, then gradually abandoned or destroyed from the beginning of the 20th century. Some of these structures are still visible today, but most have been neglected. Interest has developed in the preservation of these chimneys as a cultural heritage. This master thesis presents the seismic evaluation of two masonry chimneys in the surroundings of Porto, Portugal. An in situ investigation is performed using two forms of modal analysis (EMA and OMA) to determine their dynamic structural properties. Then, four different fiber element numerical models are developed and calibrated. The structure is then evaluated by a first analysis with the response spectrum method suggested by Eurocode 8, followed by a non-linear time analysis. The advantages and disadvantages of these two methods are discussed. Finally, the model is compared to the results of a finite element model of shell type.

Acknowledgments

I would like to thank my two supervisors, Prof. João Saraiva Esteves Pacheco De Almeida and Prof. Alexandre Costa, without whom this project could no have been done. I would like to thank them for their availability and kindness. I would also like to acknowledge the participation of Mr João Miranda Guedes who joined us for a coupled weeks to share his experience on masonry chimneys.
I thank you all for your cheerfulness and your wise advice.

I greatly thank my readers, Mr Alex Bertholet, Mme Catherine Doneux and Mr Ryan Hoult, who took some of their precious time to evaluate my work.
But also Charline who took a lot of her time to review my work.

From the LEMSC laboratory in Louvain-la-Neuve, I thank Christophe Bayart, Alex Bertholet and Antoine Bietlot who did everythig they could to help me with my experiments.

I thank particularly Alexandra Carvalho from LNEC, who provided us the accelerograms of representative seismic action in Porto.

A particular mention to the Erasmus+ program which financially supported my internship in Porto.

And finally, I would like to thank all the NCREP team members, who warmly welcomed me for two months into their office. Especially Valter and Filipe who taught me a lot during our field investigations. I do not want to leave out Ângelo, next to whom I have been sitting for two months, but also Bruno, Tiago, Carlos, João, Jorge, Lorena, Luís, Nuno and finally Renata. You all taught me something in your own way and I would like to thank you for that. Obrigado!

List of Figures

2.1 Chimney parts and archives (Guedes et al. 2019). 6
2.2 Pictures of two chimneys. 7
2.3 Pictures illustrating several degradations (López-Patiño et al. 2017). 11
2.4 One system (a) is a combination of a (b) stiffness component; (c) damping component (d) mass component (Anil K. Chopra 2012). . 12
2.5 Cantilever beam with uniform section and distributed mass (Anil K. Chopra 2012). 14
2.6 Natural vibration modes of uniform cantilever beam (Anil K. Chopra 2012) 15
2.7 (a) ground acceleration; (b) deformation for three systems with different natural periods; (c) deformation response spectrum for $\xi = 2\%$ (Anil K. Chopra 2012). 16
2.8 (a) deformation response spectrum; (b) pseudo-velocity response spectrum; (c) pseudo-acceleration response spectrum; for $\xi = 2\%$ (Anil K. Chopra 2012). 17
2.9 Damping models. 20
2.10 Steel plate used for the experiment. Dimensions on the picture. . . 22
2.11 Steel plate OMA test setup. 23
2.12 ARTeMIS steel plate geometry for the OMA test setup. 24
2.13 Relationship between the time-doamin and the frequency-doamin (Qingkai Kong, Timmy Siauw, and Alexandre M. Bayen 2021). . . . 25
2.14 Results of Singular value decomposition. 26
2.15 Mode shape associated to the first natural frequency. 27
2.16 Frequency Response Function (Schwarz and Richardson 1999). . . . 28
2.17 Pictures of EMA test setups (Linnet Gjelstrup 2021). 29
2.18 ARTeMIS steel plate geometry for the EMA test setup. 30
2.19 Results of Complex Model Indicator Function. 30
2.20 Mode shape associated to the first natural frequency found with OMA. 31
2.21 First mode shape of the steel plate. 32

2.22 2 accelerometers: Recovib Tiny on the left and PCB 393A03 with a rubber protection on the right. The Recovib Tiny dimensions are $33,439,6\ mm$. 33
2.23 Impact hammers from PCB Piezotronics. The biggest one has a length of 89 cm and weights $5,5\ kg$. 35

3.1 Location of the chimney in Aguas Santas (*www.google.com/maps*). . 38
3.2 Pictures of chimney in Aguas Santas. 39
3.3 Sealed plaque indicating the year of construction. 39
3.4 Pictures of chimney's bricks dimensions in Aguas Santas. 40
3.5 Pictures of chimney's damages in Aguas Santas. 40
3.6 Stick diagram for the chimney in Aguas Santas. 41
3.7 Plot of SVD results of the chimney in Aguas Santas. Results from FDD computation. 42
3.8 Impact hammer used for the experiment. 43
3.9 Picture of the experiment in Aguas Santas. 44
3.10 CMIF plot for the chimney in Aguas Santas. 45
3.11 Location of the chimney in Universidade Lusíada. 45
3.12 Pictures of chimney in Universidade Lusíada. 46
3.13 Demarcation between the bricks of two different colors. 47
3.14 Drawings of the chimney in Lusíada. 48
3.15 Sketch of the OMA test setup. Dimensions in meter, sensors in red. 49
3.16 Mounting of the accelerometers on the chimney. 50
3.17 Time-domain accelerations. 50
3.18 SVD plot for the chimney in Lusíada. 51
3.19 Mode shape orientation regarding the chimney deformation. 51
3.20 Sketch of the EMA test setups in Lusíada. 54
3.21 CMIF plot for the chimney in Lusíada. 55
3.22 Quad view of the mode shapes found with the EMA and their associated frequencies. 56

4.1 Cross section of the base used for the numerical model. 60
4.2 Cross section of the stack used in the numerical model. 61
4.3 Mander et al. constitutive model. 62
4.4 Discretization of the number of elements. 64
4.5 Model 1 dimensions and numerical view. 66
4.6 Model 2 dimensions and numerical view. 67
4.7 Static diagrams. 68
4.8 Model 4 dimensions and numerical view. 69
4.9 Cross section of Model 3 and Model 4. 70

6.1 Top view cross section and Model 4. 84
6.2 Stress distribution due to self-weight in all fibers. 85
6.3 Design spectrum for Porto 86
6.4 Envelope of stress distribution from the RSA of Model 4 in Porto. . 88
6.5 Relative displacement from the RSA of Model 4 in Porto. 89
6.6 First and second mode shapes of Model 4. 90
6.7 Elastic spectra of Porto. 91
6.8 Ground acceleration for the analysis in Porto. 92
6.9 Ground (in orange) and top node (in blue) displacements relative to initial node coordinates. Assessment in Porto. 94
6.10 Nodal displacements at $t = 13,815\ s$. Assessment in Porto. 95
6.11 Hysteretic curve of the base shear in $[kN]$ over the top node displacement in the Y-axis $[m]$. 96
6.12 Stresses $[kPa]$ over time $[s]$ for the fibers in the $+Y$-direction. The maximum value is $\sigma_t = 40\ kPa$ and the minimum value is $_c = -890\ kPa$. Assessment in Porto. 97
6.13 Strains $[m/m]$ over time $[s]$ for the fibers in the $-Y$-direction. The maximum value is $\varepsilon_t = 0,00098\ m/m$ and the minimum value is $\varepsilon_c = -0,00032\ m/m$. Assessment in Porto. 97
6.14 Stress and strain distribution along the height for the assessment in Porto. 98
6.15 Design spectrum for Porto 100
6.16 Envelope of stress distribution from the RSA of Model 4 in Sagres. 101
6.17 Relative displacement from the RSA of Model 4 in Sagres. 102
6.18 Elastic spectra of Sagres. 103
6.19 Ground (in orange) and top node (in blue) displacements relative to initial node coordinates. Assessment in Sagres. 105
6.20 Nodal relative displacements at $t = 36,67\ s$. Assessment in Sagres. . 106
6.21 Hysteretic curve of the base shear in $[kN]$ over the top node displacement in the Y-axis $[m]$. Assessment in Sagres. 107
6.22 Stresses $[kPa]$ over time $[s]$ for the fibers in the $+Y$-direction. The maximum value is $\sigma_t = 40\ kPa$ and the minimum value is $_c = -2921\ kPa$. Assessment in Sagres. 108
6.23 Strains $[m/m]$ over time $[s]$ for the fibers in the $-Y$-direction. The maximum value is $\varepsilon_t = 0,0075\ m/m$ and the minimum value is $\varepsilon_c = -0,001\ m/m$. Assessment in Sagres. 108
6.24 Stress and strain distribution along the height for the assessment in Sagres. 109
6.25 NCREP model of the chimney in Lusíada. 112
6.26 View of Model 5. 113

6.27 Top views. . . . 113
6.28 Fourth vibration mode shape for Model 4 and Model 6. . . . 115
6.29 Stress envelopes computed with RSA. . . . 116
6.30 Stresses $[kPa]$ over time $[s]$ for the fibers in the $+Y$-direction. The maximum value is $\sigma_t = 40\ kPa$ and the minimum value is $_c = -651\ kPa$. . . . 117
6.31 Stress $[kPa]$ over time $[s]$ for the fibers in the $-Y$-direction. The maximum value is $\sigma_t = 40\ kPa$ and the minimum value is $\sigma_c = -291\ m/m$. . . . 117
6.32 Stresses distributions. . . . 119

8.1 Typical soil elastic properties 130
8.2 Table describing the different soil type assumed in the Eurocode 8 . 132
8.3 Maps providing the value of PGA to use in Portugal, Costa, Sousa, and Carvalho 2008. . . . 133
8.4 Serie 1. . . . 136
8.5 Serie 2. . . . 136
8.6 Serie 3. . . . 137
8.7 Serie 4. . . . 137
8.8 Serie 5. . . . 138
8.9 Serie 6. . . . 138
8.10 Serie 7. . . . 139
8.11 Serie 8. . . . 139
8.12 Serie 1. . . . 140
8.13 Serie 2. . . . 141
8.14 Serie 3. . . . 141
8.15 Serie 4. . . . 142
8.16 Serie 5. . . . 142
8.17 Serie 6. . . . 143
8.18 Serie 7. . . . 143
8.19 Serie 8. . . . 144

List of Tables

2.1 Natural frequencies of uniform cantilever beam 15
2.2 Theoretical resonance frequencies of the steel plate computed with the relations given in table 2.1. 21
2.3 Results from OMA test on steel plate. 27
2.4 Results from EMA test on steel plate. 31
2.5 Comparion of results between the theoretical computation, the OMA model and the EMA model. 32
2.6 Comparison of accelerometers specifications. 34

3.1 Natural frequencies identified with OMA method in Aguas Santas. . 42
3.2 Natural frequencies identified with OMA method. 51
3.3 Frequencies and mode shapes of the chimney in Lusíada (1/2). . . . 52
3.4 Frequencies and mode shapes of the chimney in Lusíada (2/2). . . . 53
3.5 Natural frequencies identified with EMA method. 55

4.1 Frequencies obtained with the same model declined with different number of elements. 63

5.1 Parameters used for Model 1. 73
5.2 Fitness functions results of Model 1. 73
5.3 Numerical frequencies and their associated mode for Model 1. . . . 73
5.4 MAC matrix of Model 1. 73
5.5 Parameters used for Model 2. 75
5.6 Fitness functions results of Model 2. 75
5.7 Numerical frequencies and their associated mode for Model 2. . . . 75
5.8 MAC matrix of Model 2. 75
5.9 Parameters used for Model 3. 77
5.10 Fitness functions results of Model 3. 77
5.11 Numerical frequencies and their associated mode for Model 3. . . . 77
5.12 MAC matrix of Model 3. 77
5.13 Parameters used for Model 4. 79

5.14 Fitness functions results of Model 4. 79
5.15 Numerical frequencies and their associated mode for Model 4. . . . 79
5.16 MAC matrix of Model 4. 79
5.17 Comparative table of the calibration results. 81
5.18 Comparison of computed frequencies in Model 3 and Model 4. . . . 82

6.1 Summary of the values computed by the response spectrum analysis (RSA) and the dynamic time-history analysis (DTHA) for the chimney in Lusíada with the seismic conditions of Porto. 99
6.2 Summary of the values computed by the response spectrum analysis (RSA) and the dynamic time-history analysis (DTHA) for the chimney in Lusíada with the seismic conditions of Sagres. 110
6.3 NCREP model: material properties. 112
6.4 Model 6: material properties. 114
6.5 Frequencies for the NCREP model, Model 5 and Model 6. 114

8.1 Seismic parameters depending on the type of seismic action and soil. 132
8.2 Table providing the value of PGA to use in Portugal, Costa, Sousa, and Carvalho 2008. 134
8.3 Table providing the value of importance factor γ_I. 134

Contents

Abstract **I**

Acknowledgments **II**

List of figures **VI**

List of tables **VIII**

1 Introduction **1**
1.1 Context . . . 1
1.2 Goals . . . 2
1.3 Thesis organization . . . 2

2 Literature review **5**
2.1 Former industrial masonry chimneys . . . 5
2.1.1 Interest . . . 5
2.1.2 Structure . . . 5
2.1.3 Material . . . 8
2.1.4 Pathologies . . . 9
2.2 Principles of seismic analysis . . . 10
2.2.1 Principles of structural dynamics . . . 10
2.2.2 Response spectrum analysis . . . 15
2.2.3 Dynamic time-history analysis . . . 19
2.3 Modal analysis . . . 20
2.3.1 Illustration model: description and geometry . . . 21
2.3.2 Operational Modal Analysis - OMA . . . 21
2.3.3 Experimental Modal Analysis - EMA . . . 27
2.3.4 Comparison of methods . . . 31
2.4 Transducers . . . 33
2.4.1 Accelerometers . . . 33
2.4.2 Impact hammer . . . 34

3 In-situ identification **37**
3.1 Chimney in Aguas Santas . . . 37
3.1.1 Visual inspection . . . 38
3.1.2 In situ investigation . . . 41
3.2 Chimney in Universidade Lusíada . . . 45
3.2.1 Visual inspection . . . 45
3.2.2 In-situ investigation . . . 48
3.3 Conclusion for both investigations . . . 56

4 Numerical model **59**
4.1 Structural assumptions . . . 60
4.1.1 Sections geometry . . . 60
4.1.2 Material constitutive model . . . 61
4.1.3 Number of elements . . . 63
4.2 Model 1 . . . 63
4.3 Model 2 . . . 66
4.4 Model 3 . . . 67
4.5 Model 4 . . . 68
4.6 Conclusion . . . 69

5 Calibration **71**
5.1 Fitness functions . . . 71
5.2 Models . . . 72
5.2.1 Model 1 . . . 72
5.2.2 Model 2 . . . 74
5.2.3 Model 3 . . . 76
5.2.4 Model 4 . . . 78
5.3 Discussion of the results . . . 81

6 Seismic assessment **83**
6.1 Behavior under self-weight . . . 83
6.2 Assessment in Porto . . . 86
6.2.1 Response spectrum analysis . . . 86
6.2.2 Dynamic time-history analysis . . . 90
6.2.3 Conclusion . . . 98
6.3 Assessment in Sagres . . . 99
6.3.1 Response spectrum analysis . . . 100
6.3.2 Dynamic time-history analysis . . . 102
6.3.3 Conclusion . . . 109
6.4 Comparison with shell elements . . . 110
6.4.1 The model in shell elements . . . 111

6.4.2 The model in fiber elements . . . 113
6.4.3 Response spectrum analysis . . . 115
6.4.4 Dynamic time-history analysis . . . 116
6.4.5 Conclusion . . . 119

7 Conclusion **121**

Bibliography **122**

8 Appendices **125**
A Chimney in Aguas Santas: Mode shapes from OMA. . . . 125
A.1 $f_{1,x} = 0,79\ Hz$ . . . 125
A.2 $f_{1,y} = 0,85\ Hz$ . . . 126
A.3 $f_{2,x} = 2,66\ Hz$ . . . 126
A.4 $f_{2,y} = 2,95\ Hz$ . . . 127
A.5 $f_{3,x} = 5,69\ Hz$ . . . 127
A.6 $f_{3,y} = 6,40\ Hz$ . . . 128
B Derivation of soil's properties . . . 129
C Computation of the design spectrum following EC8 . . . 131
D Set of ground accelerations for the analysis in Porto . . . 136
E Set of ground accelerations for the analysis in Sagres . . . 140
F Mode shapes of Model 4 and Model 6 compared with the experimental results . . . 145

Chapter 1

Introduction

1.1 Context

The European industrial revolution in the 19^{th} century saw the rise of many industrial brick masonry chimneys. At the time they were used to evacuate the fumes and gases resulting from industrial processes. Nowadays, the change in the European economy closed many of those factories and most of them were taken down. Meanwhile, a lot of chimneys were kept in place as historical landmarks, even protected by the law in some regions.
While at the time of their construction, these impressive structures were at the heart of a thriving industry, many are now abandoned and left to face the elements alone. Most of these chimneys are more than a hundred years old and many have suffered degradation over time. It is in this context that the interest in their stability began in order to keep these marks of the past within new urban expansions.

As those structures are very flexible, they can be sensitive to dynamic actions like wind and earthquakes. Many studies published assessed their capacity to sustain seismic actions and sometimes suggest structural reinforcements.

This master thesis analyses two chimneys located in the surroundings of Porto, Portugal, to see if they can both sustain a seismic event. Access to both structures was made possible thanks to the collaboration of NCREP, a consultancy firm based in Porto.

1.2 Goals

Many studies assessing masonry chimneys are published. Most of those investigations perform ambient vibration testing and model the chimneys with finite shell elements to study the structural behavior under the assumption that its material behaves elastically.
During those investigations, engineers must first determine the structural natural frequencies. In order to do so, they use a technique called ambient vibration testing or operational modal analysis. The technique lies in the punctual recording of the structure's vibrations with a set of accelerometers. The position of those accelerometers is usually set at the top of the structure needing an elevation platform to access it.
Then they determine the material properties of the model by calibrating it so that its natural frequencies are identical or close to those acquired experimentally.

The main goal of this thesis is to perform the seismic assessment of a brick masonry chimney to determine if it needs or not any structural reinforcements. In parallel with this work, two other objectives are aimed.
The first one is to perform the dynamic identification on a ground level. To do so the method of experimental modal analysis is applied. This method does not require a lifting platform, the entire experiment can be performed at the base of the structure. This goal is of interest in order to reduce the duration and the cost of the field investigation.
The second point of research of this thesis is in the calculation method of the model. A fiber element-based model is developed in order to study the nonlinear behavior of the structure. The calibration of the model is based on vibration modes in addition to the natural frequencies.

1.3 Thesis organization

This thesis is subdivided in 6 different chapters.

1. The first chapter, chapter 2, is a brief review of the knowledge held on masonry chimneys as well as a concise explanation of the theoretical concepts discussed throughout the thesis.

2. Chapter 3 describes the in-situ tests performed on the chimneys and presents the comparison between a different investigation methods.

3. The third part, chapter 4, details the assumptions made to create the numerical models.

4. The calibration of numerical models in order to match the characteristics derived in-situ is performed in chapter 5.

5. Chapter 6 starts with the seismic analysis of the chimney at its location and then assess the chimney in the Portuguese region where the most severe earthquakes can strike. The section ends with a comparison between the assessments of a model made of shell elements and another made of fiber elements.

6. Chapter 7 derives the main conclusions from the results of this work.

Chapter 2

Literature review

This chapter is a small review of the theoretical concepts covered in this thesis. Starting with an introduction to what is an industrial masonry chimney, the chapter continues restating the basis of structural analysis. Afterward, an explanation of modal analysis methods is illustrated with a laboratory example. To finish this chapter, the different transducers used during the field investigation are presented.

2.1 Former industrial masonry chimneys

2.1.1 Interest

In Europe, the end of the nineteenth century saw the rise of many industrial masonry chimneys. The change in industrial process and the need for mass production pushed industries to equip their factories with those high structures to efficiently evacuate fumes. With the decline of this same industry, the technological advances, and the relocation of industries, most of the factories were destroyed by the end of the twentieth century. However, even if the main buildings went down, many chimneys were left in place, as marks from the past. Degraded by time, it has now become of interest to study their stability in order to preserve this cultural heritage.

2.1.2 Structure

From many observations, chimneys can be seen as made of four different parts, the foundation, the base, the stack, and the crown.
According to archive documents displayed in Figure 2.1b, *the foundation* is usually made of a shallow concrete slab directly poured onto the soil with a massive block of masonry bricks on top of it.

The base is the bottom part linking the structure to its foundation, it can take several shapes but is most commonly circular or square. On some chimneys, the base is nonexistent, in that case, the stack is directly linked to the foundation as in Figure 2.2. *The stack* is the main body of the structure, often with an external truncated conical shape. The circular shape was used to reduce the impact of the wind on the structure and to reduce the amount of material to use.
Finally, *the crown* finishes the top of the chimney. Its function is only decorative and is achieved by setting the bricks in a different pattern from the stack.

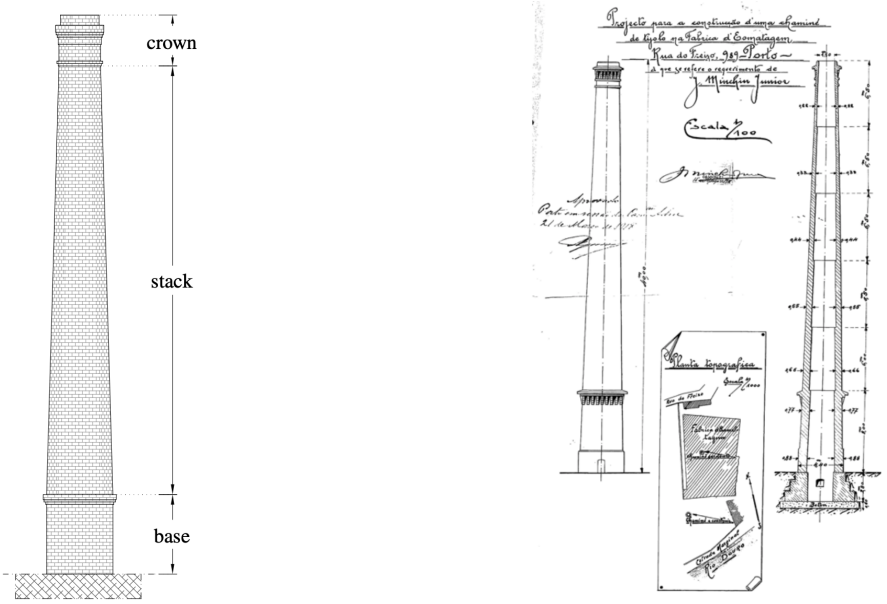

(a) Different parts of the chimney.

(b) Drawings of a chimney from archives.

Figure 2.1: Chimney parts and archives (Guedes et al. 2019).

(a) Chimney without a base.

(b) Chimney with a base.

Figure 2.2: Pictures of two chimneys.

The total height of those structures can vary from 16 m to 50 m and can sometimes reach up to 100 m (Pallarés, Ivorra, et al. 2011 and Guedes et al. 2019). The height was depending on the type of industry determining the type of gas to evacuate; the prevailing wind to sustain them; the proximity to inhabited buildings to make sure the fumes would not disturb the neighborhood.

Regarding the stack properties, as mentioned previously, its cross section is usually hollow circular. The tapered shape is achieved by dividing the stack into different parts, called sections, of constant thickness and equal height. The number of parts and their heights depend on the total height of the chimney. The lowest section is the thicker one and the top one the thinnest, usually two bricks thick, i.e. 22 cm. When a crown is present, the visual aspect can look wider.
The reduction in width between two sections is of one brick and the change within the section was made by reducing the thickness of the joints between two brick rows. Figure 2.1b shows an archive drawing describing the cross-section of the chimney.

In terms of structural design, the chimney's dimensions were computed taking into account only its self-weight and the action of the wind (Guedes et al. 2019). Globally, this means that the stabilizing forces due to the self-weight need to be greater than the overturning moment due to the action of the wind. To have a

steady structure and due to the poor tensile strength of the masonry, the designers have made sure that the resulting forces stay in the core of the section for each level of the structure, to make sure each section would be compressed at all times.

A research showed certain relations between geometrical properties. The research was carried out on ten different chimneys (Guedes et al. 2019).

- The slope of the stack vary from chimney to chimney but the literature shows that slopes from 1.8% to 2.5%.
- The structure slenderness ratio is changing between 9 to 13.

2.1.3 Material

Red bricks were used because they were widely available at that time and their technology was clearly understood. Masonry buildings do not demand large equipment thanks to their small individual size. Bricks also have good mechanical and thermal properties, an asset for a structure containing hot gases.
Before the start of the massive use of concrete cement at the end of the nineteenth century, joints were made of lime cement. The latter is less prone to cracking and can "self-heal" over time absorbing carbon dioxide but has less strength than concrete cement. Visually, the lime mortar has a whiter finish, it can be therefore noticed when the concrete mortar was used for repair.

As masonry is a composite material, its properties are not as easy to determine as a monolithic material. This work does not contain any laboratory testing, however, some order of magnitude can be found in the literature (Guedes et al. 2019, Pallarés, Agüero, and Martín 2006, Pallarés, Ivorra, et al. 2011, Sancibrian et al. 2017, Masciotta et al. 2017, Minghini, Milani, and Tralli 2014, Ramos et al. 2013). Sometimes, steel rings can be placed around the stack. Those elements are used as reinforcement for the masonry. The values hereunder will be used later on in this thesis to define masonry:

- Density : $\gamma = [16; 19]\ \frac{kN}{m^3}$
- Modulus of elasticity : $E = [2,5; 6,5]\, GPa$
- Compressive strength : $f_c = \frac{E}{[700;1000]}$
- Tensile strength : $f_t = [0; 40]\, kPa$
- Poisson ratio : $\nu = 0,2$

2.1.4 Pathologies

Damages in brick masonry chimneys can be due to several actions during their lifetime. An investigation over 538 chimneys classifies the actions inducing damages on chimneys (López-Patiño et al. 2017). They retrieved that most of those actions are namely:

Actions on material The environment can affect the bricks, the mortar, and the steel, often used for reinforcement.
The phenomena of efflorescence, the crystallization of soluble salts present in the air, especially in coastal areas, from which water can gain the structure by capillary action, was found the most common. The phenomenon of flaking of the bricks is also often noticed, this phenomenon is illustrated in Figure 2.3a.
The chemical reaction between the chimney's materials and the fumes and hot gases extracted can also induce some degradation of the material.
As it is for steel, it is mostly degraded due to corrosion. As the steel corrodes, it gains volume that can result in additional stresses on the masonry inducing cracks.

Wind Prevailing winds can have a high impact on the chimney's deformation. A study has shown that several chimneys have deformed in the same direction in the city of Oliva, Spain (Pallarés, Ivorra, et al. 2011). The wind direction affects the drying of the mortar, which makes the chimney take a certain shape.

Temperature variations The biggest temperature gradients are the ones due to the difference between the high-temperature gases inside the structure and the outside temperature. Cracks induced by this temperature variation are found near the base, where the gases are the hottest, as shown in Figure 2.3b.

Lightning strikes As chimneys are prominent structures, they are prone to lightning. The latter often induces large vertical cracks in the structure. Figure 2.3c illustrates this phenomena. However, nowadays, chimneys are usually equipped with lightning rods to avoid those degradations.

Living organism If the chimney is abandoned, the vegetation can start growing on it, and sometimes insects and birds can transform it into their new habitat. The risk with the vegetation and the insect is that it destroys the masonry joints, reducing it strength.
Concerning birds, a nest at the top of the crown can sometimes result in a consequent overload, but also their drippings are threatening the masonry,

they contain some chemical compounds that can react with the mortar, removing it.

Earthquake Seismic actions on chimneys can result sometimes in large cracks and masonry shifts which induce important changes in the materials' properties and structure's geometry. In worst cases, earthquakes may cause the partial or total collapse of the chimney. To avoid those catastrophic results, recent years saw an improvement in the characterization and the assessment of brick masonry chimneys.

2.2 Principles of seismic analysis

2.2.1 Principles of structural dynamics

This work uses notions from structural dynamics, this section has the purpose of reminding the reader of those principles to ease his comprehension.

Newton's second law states that the sum of the forces acting on a system is equal to the product of the system's mass with its acceleration.

$$\sum \mathbf{F}(t) = m \cdot \ddot{u}(t) \tag{2.1}$$

With $\mathbf{F}$ the vector of forces acting on the system, m the mass (assumed constant in time), and $\ddot{u}$ the acceleration. Reformulating this equation separating the external forces from the resisting forces:

$$\sum \mathbf{F} = m \cdot \ddot{u} \Leftrightarrow p(t) - p_r(t) = m \cdot \ddot{u}(t) \Rightarrow m \cdot \ddot{u}(t) + p_r(t) = p(t) \tag{2.2}$$

With $p_r(t)$ the resisting forces of the system and $p(t)$ the external forces acting on the system.
The resisting forces can be separated in two different terms: one related to the displacement f_S and the other to the velocity f_D.

$$p_r(t) = f_S(u(t)) + f_D(\dot{u}(t)) \tag{2.3}$$

The displacement-related component $f_S(u(t)) = k \cdot u(t)$ has a lateral stiffness k constant if the system is linear elastic. If not, the system is called inelastic and the lateral stiffness depends on the displacement $k(u)$.

The velocity-related component $f_D(\dot{u}(t)) = c \cdot \dot{u}(t)$ has a viscous damping coefficient c representing the energy dissipation through the structure.

(a) Flaking of the masonry.

(b) Cracks due to temperature gradients.

(c) Cracks due to lightning strikes.

Figure 2.3: Pictures illustrating several degradations (López-Patiño et al. 2017).

Substituting those terms into equation 2.2, the so-called *Equation of motion* for a linear elastic single degree of freedom is obtained:

$$m \cdot \ddot{u}(t) + c \cdot \dot{u}(t) + k \cdot u(t) = p(t) \tag{2.4}$$

Figure 2.4 illustrates the different components of the structural response with a simple frame. The term f_I refers to the acceleration component, $f_I = m \cdot \ddot{u}(t)$.

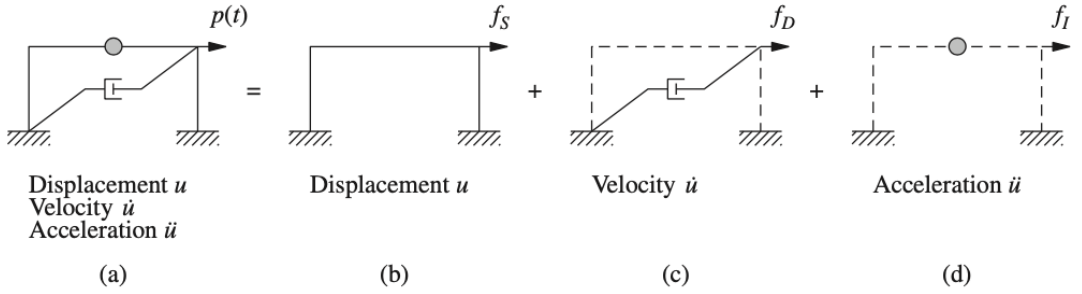

Figure 2.4: One system (a) is a combination of a (b) stiffness component; (c) damping component (d) mass component (Anil K. Chopra 2012).

Single degree of freedom - SDoF

The problem of a single degree of freedom system under free vibration can be expressed as

$$\begin{cases} m \cdot \ddot{u}(t) + c \cdot \dot{u}(t) + k \cdot u(t) = 0 \\ u(0) = u_0 \\ \dot{u}(0) = \dot{u}_0 \end{cases} \tag{2.5}$$

If we divide the first equation by the mass, we obtain

$$\ddot{u}(t) + 2 \cdot \xi \cdot \omega \cdot \dot{u}(t) + \omega^2 \cdot u(t) = 0 \tag{2.6}$$

Where $\omega = \sqrt{\frac{k}{m}}$ is the natural circular frequency and $\xi = \frac{c}{2m\omega}$ the damping ratio. The natural cyclic frequency can be derived as $f = \frac{\omega}{2\pi}\ [Hz]$, as well as the natural period of vibration $T = \frac{1}{f}\ [s]$.

For an undamped system under free vibrations, when $c = 0$, the problem can be expressed as follows:

$$\begin{cases} m \cdot \ddot{u}(t) + k \cdot u(t) = 0 \\ u(0) = u_0 \\ \dot{u}(0) = \dot{u}_0 \end{cases} \tag{2.7}$$

Dividing the first equation by the mass, it becomes

$$\ddot{u}(t) + \omega^2 \cdot u(t) = 0 \tag{2.8}$$

The solution of this system is called a simple harmonic motion, equation 2.9.

$$u(t) = u(0)cos(\omega t) + \frac{\dot{u}(0)}{\omega} sin(\omega t) \tag{2.9}$$

Multiple degrees of freedom - MDoF

Multiple degrees of freedom systems can be expressed as a linear combination of SDoF systems.

$$\mathbf{M} \cdot \ddot{\mathbf{U}}(t) + \mathbf{C} \cdot \dot{\mathbf{U}}(t) + \mathbf{K} \cdot \mathbf{U}(t) = \mathbf{P}(t) \tag{2.10}$$

Where $\mathbf{M}$, $\mathbf{C}$ and $\mathbf{K}$ are respectively the mass, damping, and stiffness matrices.

The problem of a linear elastic undamped MDoF system of N degrees of freedom is expressed as follows:

$$\begin{cases} \mathbf{M}\ddot{\mathbf{U}}(t) + \mathbf{K}\mathbf{U}(t) = 0 \\ \mathbf{U}(t=0) = \mathbf{U}(0) \\ \ddot{\mathbf{U}}(t=0) = \ddot{\mathbf{U}}(0) \end{cases} \tag{2.11}$$

The general solution of this problem is

$$\mathbf{U}(t) = \phi \cdot (Acos(\omega t) + Bsin(\omega t)) \tag{2.12}$$

With this solution injected in the first equation, a classical eigenvalue equation is obtained:

$$\mathbf{K} \cdot \phi_i = \omega_i^2 \cdot \mathbf{M} \cdot \phi_i \tag{2.13}$$

The non trivial solution are given by the characteristic equation:

$$det\left[\mathbf{K} - \omega_i^2 \mathbf{M}\right] = 0 \tag{2.14}$$

Where ω_i and ϕ_i are the natural frequency and modes of vibration associated with the i^{th} mode. The number of modes is equal to the number of degrees of freedom.

To define the dynamic parameter of a structure, such as natural frequencies and modes of vibration, engineers can exploit modal analysis. This study is based on tests performed directly on the structure of interest. It exists under two forms, which are detailed and illustrated with an example in section 2.3.

Distributed mass

For an undamped system with a distributed mass and uniform stiffness under free vibration, the following solution defines the modes of vibration (Anil K. Chopra 2012):

$$\phi(x) = C_1 \sin \beta x + C_2 \cos \beta x + C_3 \sinh \beta x + C_4 \cosh \beta x \tag{2.15}$$

where $\beta^4 = \frac{\omega^2 m}{EI}$. C_1, C_2, C_3 and C_4 are constants determined by the boundary conditions, m is the distributed mass with units of [mass/length], E is the elastic modulus and I the moment of inertia.

In the case of a straight cantilever beam, as illustrated in figure 2.5, the boundary condition at $x = 0$ is that the displacement and the rotation are both nulls. And at $x = L$, both the bending moment and the shear are equal to zero.

$$\begin{cases} u(0,t) = 0 \\ \dot{u}(0,t) = 0 \\ M(L,t) = 0 \\ V(L,t) = 0 \end{cases} \tag{2.16}$$

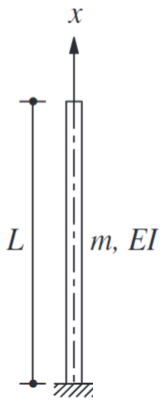

Figure 2.5: Cantilever beam with uniform section and distributed mass (Anil K. Chopra 2012).

After a bit of mathematics, the expression of the first four natural frequencies and their mode of vibration is obtained (Anil K. Chopra 2012). Table 2.1 and figure 2.6 displays those results. The equation giving the vibration modes is

$$\phi_n(x) = C_1 \left[\cosh \beta_n x - \cos \beta_n x - \frac{\cosh \beta_n L + \cos \beta_n L}{\sinh \beta_n L + \sin \beta_n L} \left(\sinh \beta_n x - \sin \beta_n x \right) \right] \tag{2.17}$$

where C_1 is an arbitrary constant.

Table 2.1: Natural frequencies of uniform cantilever beam

n	1	2	3	4
$\beta \cdot L$	1,8751	4,6941	7,8549	10,996
ω	$\frac{3{,}516}{L^2}\sqrt{\frac{EI}{m}}$	$\frac{22{,}03}{L^2}\sqrt{\frac{EI}{m}}$	$\frac{61{,}70}{L^2}\sqrt{\frac{EI}{m}}$	$\frac{120{,}9}{L^2}\sqrt{\frac{EI}{m}}$

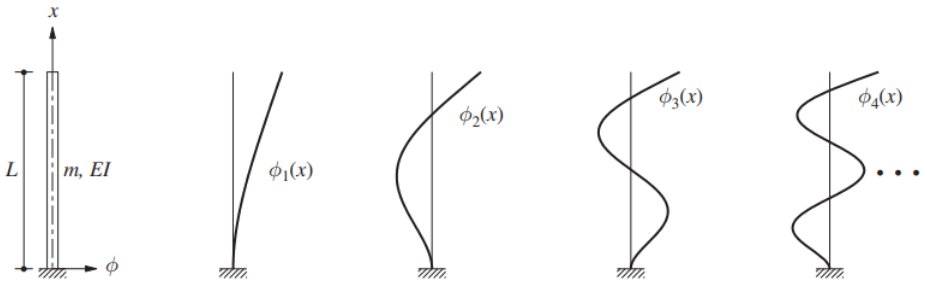

Figure 2.6: Natural vibration modes of uniform cantilever beam (Anil K. Chopra 2012)

2.2.2 Response spectrum analysis

Principle of the analysis

As the response of a MDoF is a combination of responses of several SDoF, the study of this one is of interest.

When a SDoF is subject to a ground motion, its displacement response history $u(t)$ can be evaluated, and using static analysis, its internal forces can be retrieved. This technique is called the *equivalent static force method*.

$$p_{eq}(t) = k \cdot u(t) = m \cdot \omega^2 \cdot u(t) = m \cdot A(t) \tag{2.18}$$

Where p_{eq} is the equivalent force acting on the system, m is the total mass of the system and $A(t) = \omega^2 \cdot u(t)$ is called the pseudo-acceleration. A is different from the acceleration of the system but has the units of acceleration, that is why it is called "pseudo".

The response spectrum of a linear SDoF system plots a peak response quantity, for a specified damping ratio ξ, as a function of its natural vibration frequency, for a given excitation. It summarizes the peak response of any linear SDoF systems

(any T and ξ) for a particular ground motion.
The example displayed in figure 2.7 shows how the peak deformations of three different systems, with the same damping ratio but different natural vibration periods, are obtained with the deformation response spectrum.

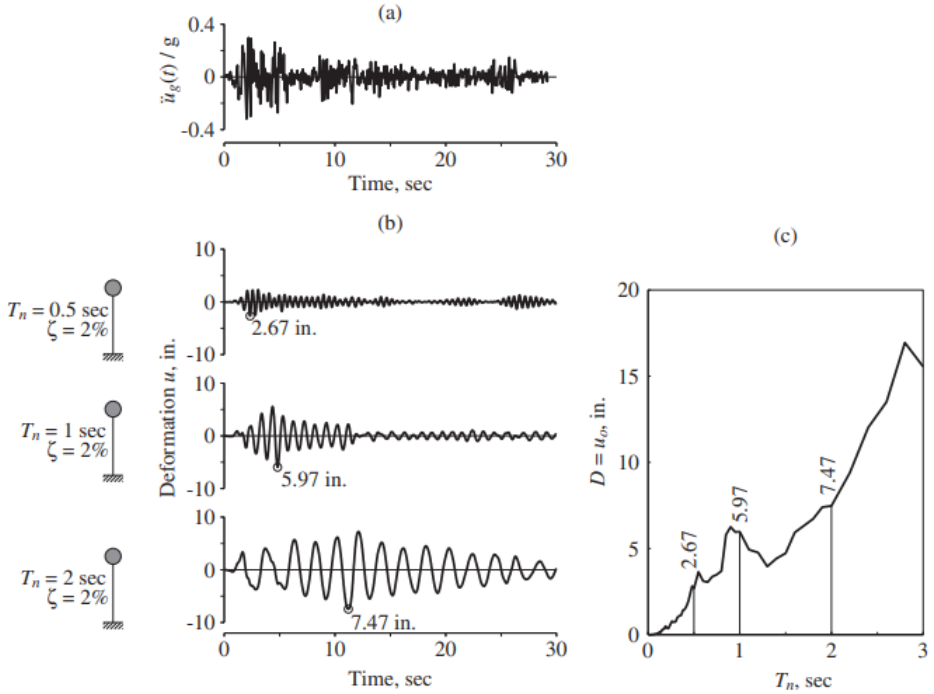

Figure 2.7: (a) ground acceleration; (b) deformation for three systems with different natural periods; (c) deformation response spectrum for $\xi = 2\%$ (Anil K. Chopra 2012).

In earthquake engineering, the most commonly used spectrum is the one representing the pseudo-acceleration $A(t)$ as a function of the natural vibration period of the system T. This value is preferred because the product of the pseudo-acceleration with the total mass of the structure gives directly the peak base shear of the system.

It exists a simple relationship between the response spectra of deformation, pseudo-velocity and pseudo-acceleration.

$$A(t) = \omega_n \cdot V(t) = \omega_n^2 \cdot D(t) \tag{2.19}$$

The three quantities from the previous example are displayed in figure 2.8.

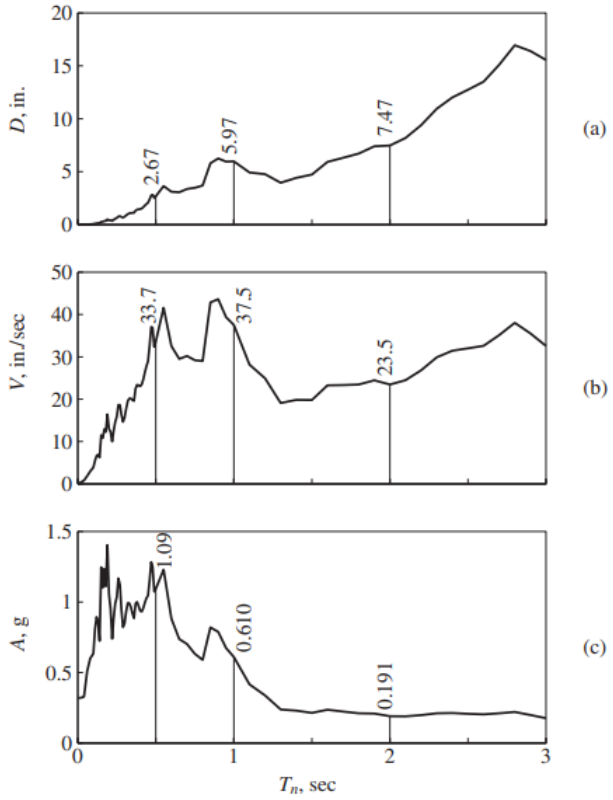

Figure 2.8: (a) deformation response spectrum; (b) pseudo-velocity response spectrum; (c) pseudo-acceleration response spectrum; for $\xi = 2\%$ (Anil K. Chopra 2012).

Application to a MDoF system

The Response Spectrum Analysis is a linear elastic static-(pseudo) dynamic statistical analysis method. It is called (pseudo) dynamic because the analysis gives the peak response of the system based on the response spectrum of a ground motion. For each natural mode, an equivalent static force distribution will be computed and finally put together using a statistical combination rule.

Recall equation 2.10, expressing an elastic multiple degrees of freedom system. When the MDoF system is subjected to a ground motion, the expression can be written as (Anil K. Chopra 2012 and João Almeida 2021):

$$\mathbf{MU}(t) + \mathbf{CU}(t) + \mathbf{KU}(t) = -\mathbf{MJ}\ddot{u}_g(t) \tag{2.20}$$

Where $\mathbf{J}$ denotes the ground motion influence vector. It gives the displacement of each degree of freedom when the system is subjected to a unit ground displacement.

The action of the ground motion on the structure can be expressed as a force distribution on the structure. The contribution to this spatial distribution of effective earthquake forces given by a certain mode j is noted $\mathbf{P}_{ref,j}$. It is defined as follows:

$$\boldsymbol{P}_{ref,j} = \Gamma_j \boldsymbol{M} \phi_j \tag{2.21}$$

Γ_j is called the modal participation factor of the mode j. The modal participation factor for each mode is given by:

$$\Gamma_j = \frac{\phi_j^T \mathbf{MJ}}{\phi_j^T \mathbf{M} \phi_j} \tag{2.22}$$

Given the pseudo-acceleration endured by the structure, retrieved from the pseudo-acceleration response spectrum of the ground motion, it is possible to compute the contribution of the j-th mode to the maximal value of the total displacement as:

$$q_{j,\max} = \Gamma_j \cdot \frac{1}{\omega_j^2} \cdot S_{pa}\left(\omega_j, \xi_j\right) \tag{2.23}$$

However, all the maximum values are not reached at the same time, this is why they need to be combined with a statistical combination rule.
The Square-Root-of-Sum-of-Squares (SRSS) method can produce a good estimate of the displacement when the modes are well separated, this is the method used later in the thesis. The total displacement corresponding to the i-th degree of freedom is computed as follows:

$$\mathrm{U}_{i,\max} \approx \sqrt{\sum_{j=1}^{N} \left(\phi_{ij} q_{j,\max}\right)^2} \tag{2.24}$$

The spectra in Eurocode 8

The European codes created a parametric spectrum based on a statistical analysis of the history of ground motion recordings available, to be able to assess a response spectrum analysis on a specific location. They named it the *Design Spectrum.*
The design spectrum is to be used to design new buildings but also to assess the safety of existing structures.

The parameters needed for the Design Spectrum are:

- The soil type: the type of soil underneath the structure influences the seismic waves propagation.
- The peak ground acceleration a_{gR}: that is the maximum ground acceleration that can occur to a certain location.

- The damping ratio ξ: a nominal damping ratio of $\xi = 5\%$ is commonly used.
- The importance factor γ_I: it depends on the type of structures studied.
- The behavior factor q: takes into account that the structure will not respond perfectly elastically.

Then the design spectrum can be obtained with the following equations:

$$\begin{aligned}
&0 \leq T \leq T_{\mathrm{B}} : S_{\mathrm{d}}(T) = a_{\mathrm{g}} \cdot S \cdot \left[\frac{2}{3} + \frac{T}{T_{\mathrm{B}}} \cdot \left(\frac{2,5}{q} - \frac{2}{3}\right)\right] \\
&T_{\mathrm{B}} \leq T \leq T_{\mathrm{C}} : S_{\mathrm{d}}(T) = a_{\mathrm{g}} \cdot S \cdot \frac{2,5}{q} \\
&T_{\mathrm{C}} \leq T \leq T_{\mathrm{D}} : S_{\mathrm{d}}(T) \begin{cases} = a_{\mathrm{g}} \cdot S \cdot \frac{2,5}{q} \cdot \left[\frac{T_{\mathrm{C}}}{T}\right] \\ \geq \beta \cdot a_{\mathrm{g}} \end{cases} \\
&T_{\mathrm{D}} \leq T : \quad S_{\mathrm{d}}(T) \begin{cases} = a_{\mathrm{g}} \cdot S \cdot \frac{2,5}{q} \cdot \left[\frac{T_{\mathrm{C}} T_{\mathrm{D}}}{T^2}\right] \\ \geq \beta \cdot a_{\mathrm{g}} \end{cases}
\end{aligned} \tag{2.25}$$

Where T is the vibration period; $S_d(T)$ is the design spectrum; S, T_B, T_C and T_D are parameters depending on the soil type; and $a_g = a_{gR} \cdot \gamma_I$.
β is the lower bound factor, the recommended value is $0,2$.

The displacement values obtained with this method will have to be corrected as the Response Spectrum Analysis bases its computation on the hypothesis that the structure will behave elastically.

$$d_s = q_d \cdot d_e \tag{2.26}$$

d_s is the displacement of a point of the structure due to seismic action. q_d is the coefficient of displacement behavior, equal to q unless specified otherwise. d_e is the displacement of a point of the structure computed using the Design Spectrum.

2.2.3 Dynamic time-history analysis

The dynamic time-history analysis is a nonlinear method used to predict the inelastic behavior of a system subjected to a ground motion. Using certain algorithms, the equation of motions is directly numerically integrated. This method can only be achieved numerically and can be time-consuming.
The only input needed is a discretized ground acceleration and its point of action on the structure. The software will output the response of the structure for each time step.

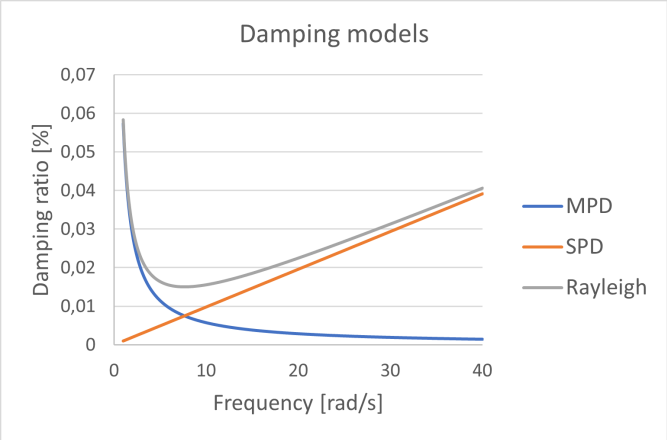

Figure 2.9: Damping models.

To model energy dissipation, a damping model needs to be assigned to the structure. There exist three models: mass-proportional damping, stiffness-proportional damping, and Rayleigh damping, which combines the two. Figure 2.9 illustrates the relation between the three models.
The Rayleigh damping defines the damping matrix as a function of the mass matrix $\mathbf{M}$ and the stiffness matrix $\mathbf{K}$ as follows

$$\mathbf{C} = \alpha\mathbf{M} + \beta\mathbf{K} \tag{2.27}$$

where α and β are both two scalars with units of $[1/s]$.
As the damping ratio of the i-th mode is defined such as

$$\xi_i = \frac{\alpha}{2}\frac{1}{\omega_i} + \frac{\beta}{2}\omega_i \tag{2.28}$$

The coefficients α and β can be determined with the specified frequencies and damping ratios of only two modes (Anil K. Chopra 2012 and Alipour, Zareian, and Student 2008):

$$\frac{1}{2}\begin{bmatrix} 1/\omega_i & \omega_i \\ 1/\omega_j & \omega_j \end{bmatrix}\begin{Bmatrix} \alpha \\ \beta \end{Bmatrix} = \begin{Bmatrix} \xi_i \\ \xi_j \end{Bmatrix} \tag{2.29}$$

2.3 Modal analysis

This section explains the purpose of modal analysis and the use of the modal identification software ARTeMIS Modal. To this end, an example of a cantilever metallic plate is presented. All experiences were realized in the LEMSC laboratory in Louvain-la-Neuve, Belgium.

Table 2.2: Theoretical resonance frequencies of the steel plate computed with the relations given in table 2.1.

$f_1\ [Hz]$	$f_2\ [Hz]$	$f_3\ [Hz]$	$f_4\ [Hz]$
2,04	12,81	35,89	70,32

2.3.1 Illustration model: description and geometry

Since the final goal is to study masonry chimneys, a vertical cantilever steel plate was chosen to perform preliminary experiments. The literature shows that a typical industrial chimney of about 20 m height has natural resonance frequencies associated with its first mode around 1 Hz and its second mode around 4 Hz (Costa, Sousa, and Carvalho 2008, Guedes et al. 2019, Sancibrian et al. 2017). To determine the plate's dimensions, the equations detailed in section 2.2.1 are used, using a Young modulus of 200 GPa and a density of 7800 kg/m^3 for the steel. The final geometry, displayed in figure 2.10 chosen was a plate of 2 m high, $0,17$ m wide with a thickness of $0,01$ m. The theoretical frequencies, computed with the relations given in table 2.1, are displayed in table 2.2.

A good rule of thumb is that the mass of the object should be ten times greater than the total mass of the sensors, for them not to interfere with the natural frequencies values (Linnet Gjelstrup 2021). The sensors used for this experiment are the model 393A03 from PCB Piezotronics. The steel plate mass over two PCB accelerometers gives

$$\frac{m_{\text{steel plate}}}{2 \cdot m_{\text{PCB}}} = \frac{2\ m \cdot 0,17\ m \cdot 0,01\ m \cdot 7800\ kg/m^3}{2 \cdot 0,302\ kg} = 43,9 \tag{2.30}$$

The ratio is well verified.

The goal is to verify if the frequencies computed analytically match the one experimentally obtained. Two different test setups are presented in the following sections. The first one is a test using ambient vibrations with three wireless accelerometers located near the base. The second one is an EMA test using 2 wired accelerometers and one impact hammer.

2.3.2 Operational Modal Analysis - OMA

The Operational Modal Analysis, or output-only or ambient analysis, aims to determine the inherent properties of a structure only by measuring the response of this one to an unmeasured excitation. This type of modal analysis is used on civil engineering structures because it can be performed in situ without interrupting the use of the structure (which can be convenient for a bridge for example) and under

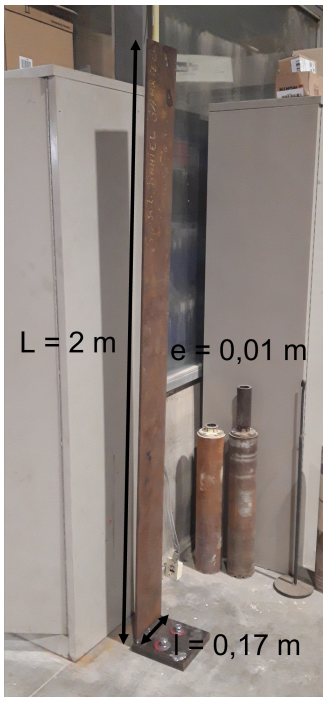

Figure 2.10: Steel plate used for the experiment. Dimensions on the picture.

operating conditions. Moreover, those structures are constantly naturally excited by the wind.

Three sensors, Micromega Recovib Tiny, are used in this experiment. To make sure the lower frequencies can be well defined, it is suggested to use a minimum recording time of (Santoro, Bassoli, and Vincenzi 2021): $t = \frac{1000}{f_1}$. Since the first theoretical frequency is $f_1 = 2,04\ Hz$, the minimum recording time should be $t = \frac{1000}{2,04} = 490\ s = 8\ min\ 10\ s$. To ease the process the sensors are configured for a $9\ min$ recording. They were then placed magnetically in the first third of the structure. The idea is to verify that we can obtain enough data from the bottom of the structure, to see if this situation would be feasible on a chimney where sometimes the top part is not accessible. Figure 2.11 shows the cantilever steel plate with the two accelerometers in place at $h = 0\ m$, $h = 0,33\ m$ and $h = 0,67\ m$.

Figure 2.11: Steel plate OMA test setup.

Using ARTeMIS Modal, the natural frequencies and mode shapes are extracted from the data.
The geometry of the plate can be modeled as a vertical straight line between two nodes, with a node for each point of measure. Figure 2.12 shows the stick model created in ARTeMIS with arrows representing the DoF of the accelerations recorded.

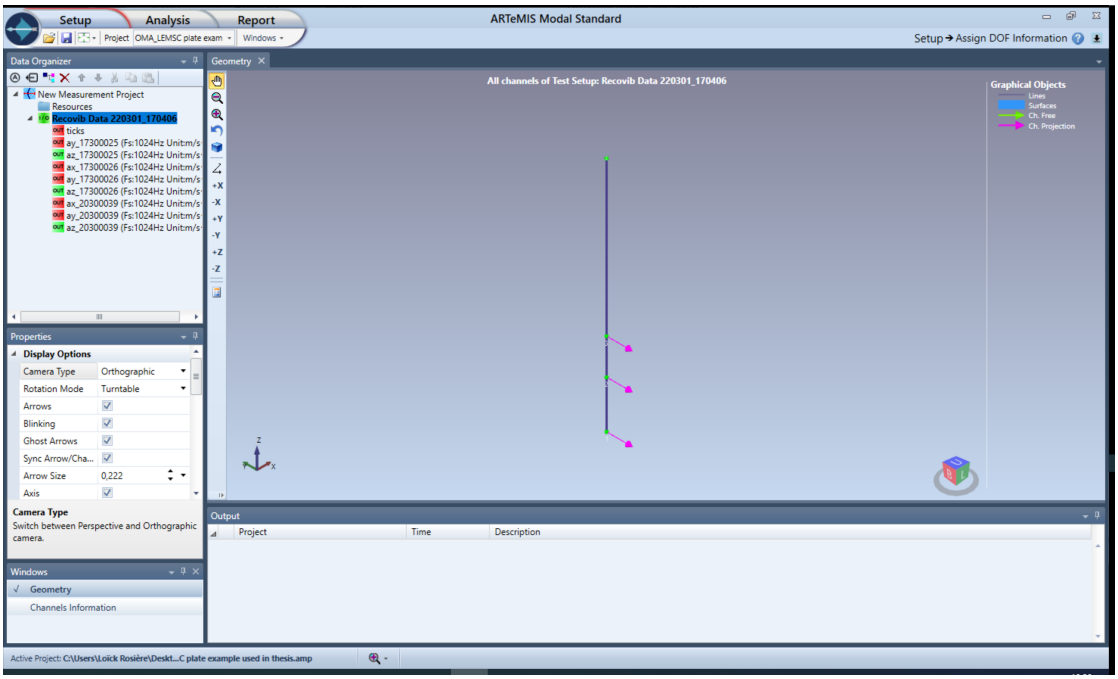

Figure 2.12: ARTeMIS steel plate geometry for the OMA test setup.

Signal processing Once the time-domain accelerations are recorded, a Discrete Fourier Analysis is performed to obtain acceleration spectral density matrices. This analysis is pursued by specifying the frequency range, which can only be a fraction of the original sampling frequency. The frequency range delimits the boundaries within which the computations are performed. In this case, the sampling frequency is 1024 Hz, and the highest theoretical natural frequency searched for is $70,32$ Hz. So a frequency range of $[0; 102,4]$ Hz is sufficient. Figure 2.13 shows the principle of the DFT, the relationship between the time-domain and the frequency-domain.

A spectral density matrix is calculated for each measurement taken and the size of those matrices is $n \times n$, where n is the number of sensors. So in this experiment, only one spectral density matrix per frequency is computed with a size of 3×3. Each matrix is composed of power and cross-spectral densities:

$$[G_{yy}(j\omega)]_i = \begin{bmatrix} \text{PSD}_{11}(j\omega) & \text{CSD}_{12}(j\omega) & \text{CSD}_{13}(j\omega) \\ \text{CSD}_{21}(j\omega) & \text{PSD}_{22}(j\omega) & \text{CSD}_{23}(j\omega) \\ \text{CSD}_{31}(j\omega) & \text{CSD}_{32}(j\omega) & \text{PSD}_{33}(j\omega) \end{bmatrix}_i \tag{2.31}$$

where $\text{PSD}(j\omega)$ denotes the power spectral density, which is the magnitude of the auto spectral density, and $\text{CSD}(j\omega)$ the cross-spectral density. The index i refers to the test setup.

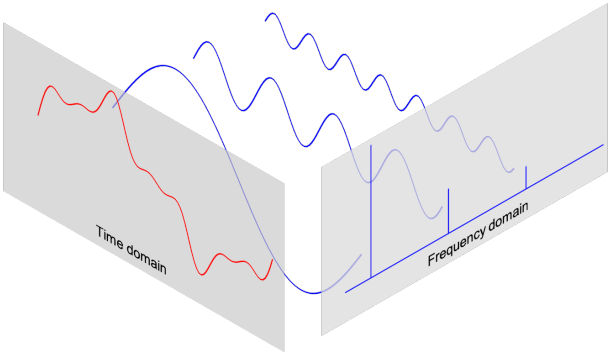

Figure 2.13: Relationship between the time-doamin and the frequency-doamin (Qingkai Kong, Timmy Siauw, and Alexandre M. Bayen 2021).

Singular Value Decomposition A Singular Value Decomposition is a mathematical tool used to factorize a real or complex matrix into two unitary matrices and one diagonal matrix. It is expressed as follows:

$$A = U\Sigma V^H \tag{2.32}$$

U and V are unitary which means that $U \cdot U^H = U^H \cdot U = I$ where H denotes the transpose and complex (Hermitian) operator.
Σ is a diagonal matrix, so only the values on its diagonal are different from zero. When the SVD is performed on a spectral density matrix, it is approximated to this expression:

$$\begin{gathered}[G_{yy}(j\omega)] = [\Phi][\Sigma][\Phi]^H \\ \text{with } [\Phi]^H[\Phi] = [I]\end{gathered} \tag{2.33}$$

Where $[\Phi]$ takes the from

$$[\Phi] = [\{\varphi_1\}\{\varphi_2\}\{\varphi_3\}\ldots\{\varphi_r\}] \tag{2.34}$$

and φ are estimates of the mode shapes. The singular values and their corresponding singular vectors are ranked from highest to lowest for each of the spectral density matrices. Figure 2.14 shows the singular values obtained for the example. The blue curve shows the first singular value, it is always above the two others. The number of curves corresponds to the number of measured degrees of freedom, that is why there are three curves in the graph.
It is explained (Batel and Kjaer 2002): "This technique allows us to identify possible coupled modes that are often indiscernible as they appear on the spectral density

functions. If only one mode is dominating at a particular frequency (only the first line will have a peak), then only one singular value will be dominating at this frequency. In the case of close or repeated modes, there will be as many dominating singular values as there are close or repeated modes (repeated peaks in the lower lines)."

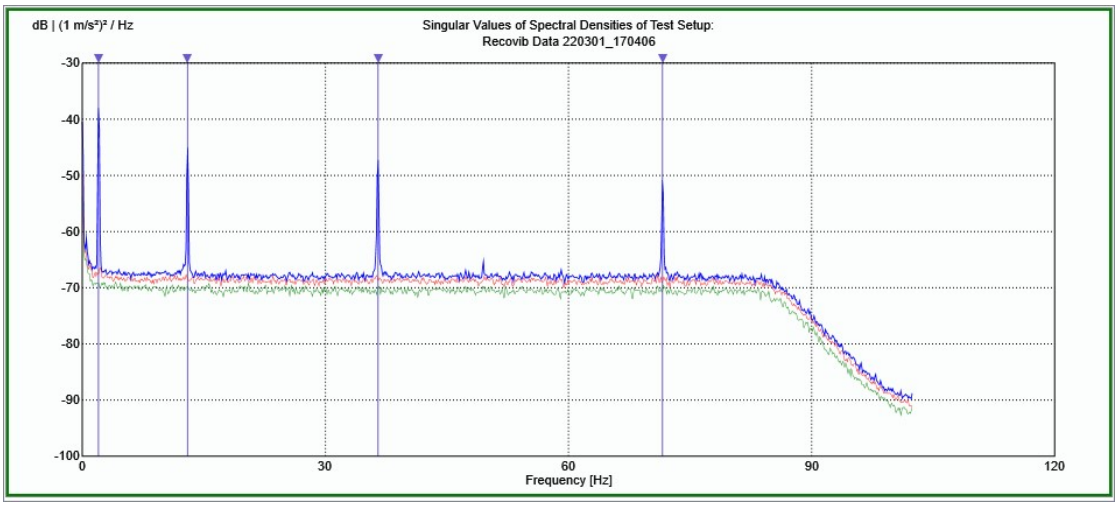

Figure 2.14: Results of Singular value decomposition.

Frequency Domain Decomposition In this case, only one data set was recorded, but when several test setups are measured, the natural frequencies are identified over an average of the SVDs of all data sets.
Table 2.3 shows the SVD and the natural frequencies evaluated with the FDD method. The mode shapes obtained are not totally representative of the real ones of the structure because the DOFs identified are only near the base. However, figure 2.15 displays the mode shape associated with the first natural frequency of 2 Hz and a smooth curve, starting from the bottom, can be observed when connecting the dots, matching the theoretical mode for that part (see figure 2.6 in section 2.2.1). It should be noted that the OMA does not provide scaled mode shapes. So no identification of modal mass is possible.

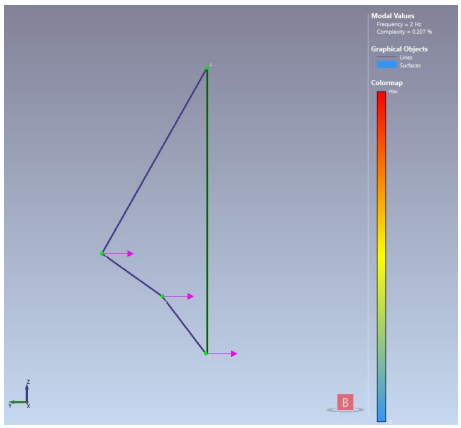

Figure 2.15: Mode shape associated to the first natural frequency $f_1 = 2,0\ Hz$. The green line is the undeformed structure.

Table 2.3: Results from OMA test on steel plate.

$f_1\ [Hz]$	$f_1\ [Hz]$	$f_1\ [Hz]$	$f_1\ [Hz]$	SVD
$2,0$	$13,0$	$36,5$	$71,6$	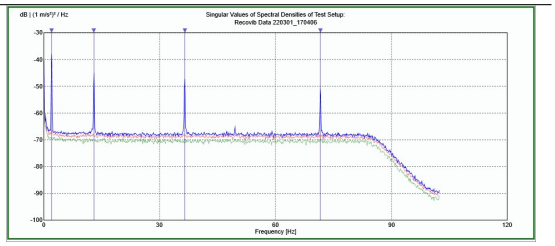

2.3.3 Experimental Modal Analysis - EMA

In EMA, both excitation (input) and responses (output) are measured. The principle of the analysis is to derive modal parameters using the frequency response function (FRF). This type of analysis can be performed either in a laboratory or directly in the field.
The FRF is an indicator of the relationship between one input and one output as a function of frequency. Figure 2.16 shows a schematic bloc of the FRF $[H(\omega)]$, which can be defined as the ratio between the Fourier transform of the output signal $X(\omega)$ and the one of the input signal $Y(\omega)$. The FRF describes then a relationship between two specific points on the object.

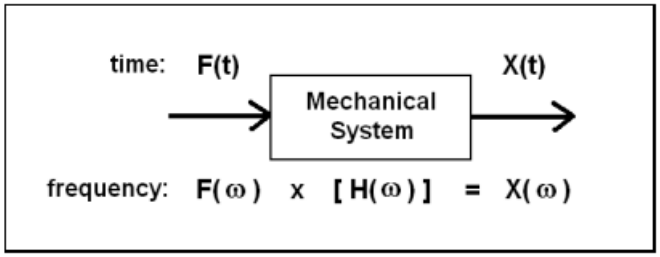

Figure 2.16: Frequency Response Function (Schwarz and Richardson 1999).

Modern algorithms computing FRF's use estimators to reduce the effect of random noise and signal distortion. There are 3 estimators: H_1, H_2 and H_V.

- H_1 assumes that the noise is on the output only.
- H_2 assumes all the noise is on the input signal.
- H_V is a combination of both H_1 and H_2, it assumes that noise is on both input and output signals. It uses the H_1 estimator near anti-resonance and H_2 at resonance frequencies.

Performing a modal test

The EMA can work with either one input and one output (SISO - single input single output), one input and multiple outputs (SIMO - single input multiple outputs), or with multiple inputs and outputs (MIMO - multiple input multiple outputs). Figure 2.17 shows the difference between a SISO and a SIMO test.
The reference DOFs are always the fixed ones.

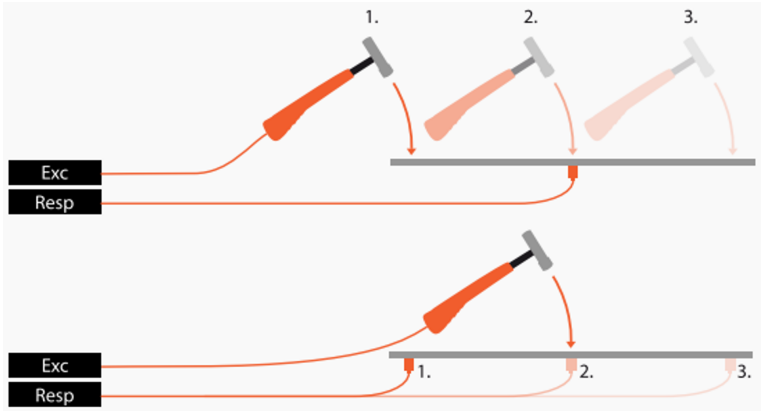

(a) SISO tests with a fixed accelerometer and a rowing hammer at the top and a fixed impact point with a rowing sensor at the bottom.

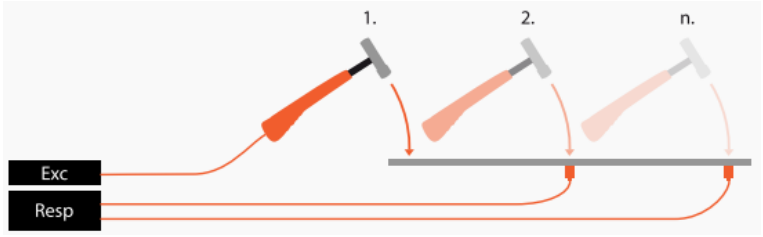

(b) SIMO test.

Figure 2.17: Pictures of EMA test setups (Linnet Gjelstrup 2021).

For this experiment, two PCB accelerometers and one modal hammer all wired to the same acquisition card are being used. The accelerometers are placed at one-third and two-thirds of the plate's height. The plate is hit with the modal hammer at 4 different locations: at the bottom and at $1/4^{th}$, $2/4^{th}$, and $3/4^{th}$ of the height.
A pre-trigger time of 2 seconds is used and the plate's response is recorded for 30 seconds, which makes a total recording time of 32 seconds. The pre-trigger time is a time slot recorded before the impact, to make sure the whole response is recorded.
Figure 2.18 illustrates the geometry model used in ARTeMIS. The blue arrows are the accelerometers and the green arrows with the hammer icons indicate the impact points.
The EMA analysis uses a Complex Mode Indicator Function (CMIF) to process the time-domain data. The CMIF is estimated from a SVD of the Frequency Response Function of the raw data. The main assumption is that, for each frequency, the FRF can be expressed as a sum of modal vectors. The peaks of the CMIF plot indicate the existence of a mode. In figure 2.19, the peaks of the CMIF are identifying the natural frequencies of the plate.

Table 2.4 summarizes the natural frequencies found in this experiment.
The first natural mode of vibration computed with the method is displayed in figure 2.20.

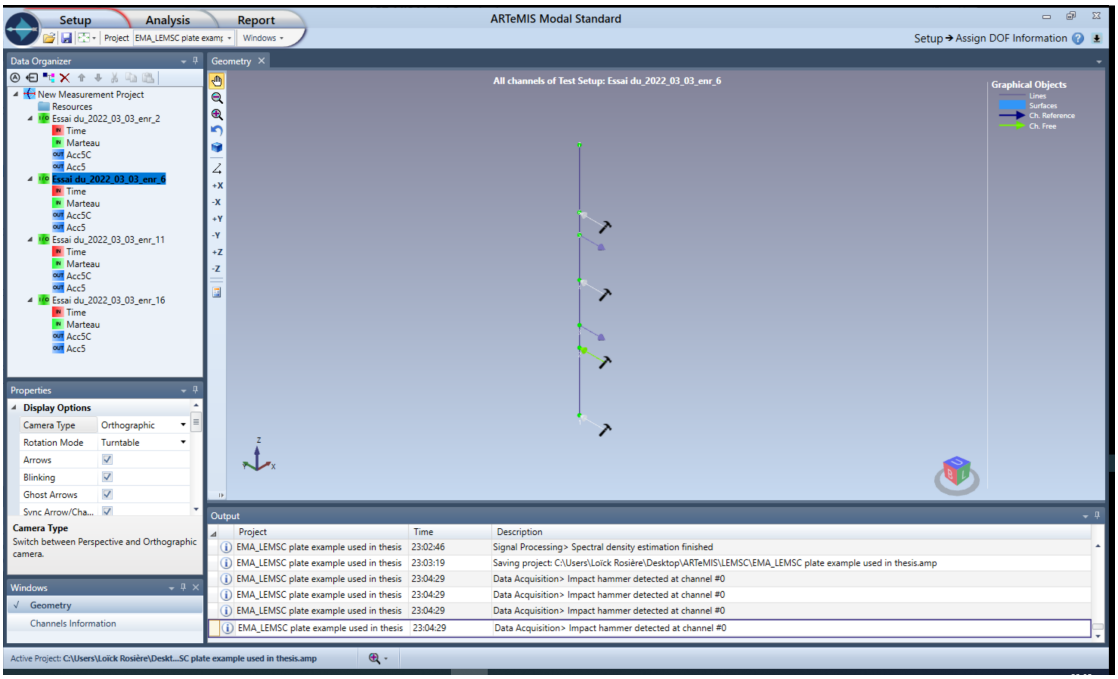

Figure 2.18: ARTeMIS steel plate geometry for the EMA test setup.

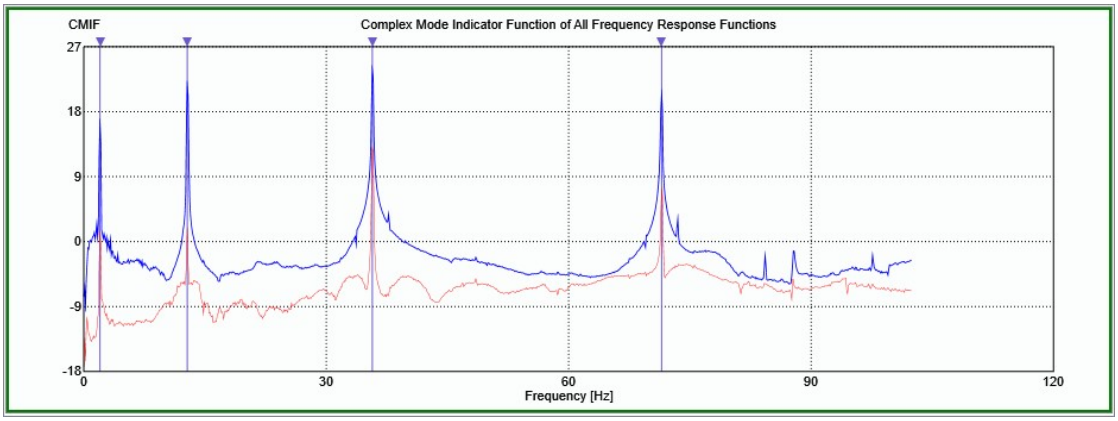

Figure 2.19: Results of Complex Model Indicator Function.

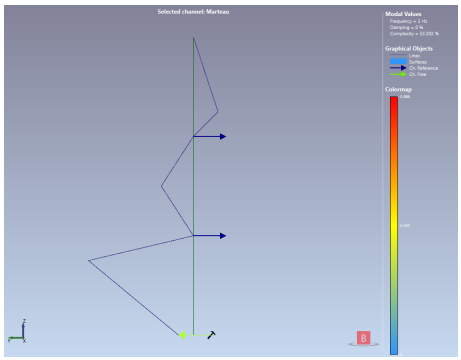

Figure 2.20: Mode shape associated to the first natural frequency $f_1 = 2,0\ Hz$ found with EMA. The green line is the undeformed structure.

Table 2.4: Results from EMA test on steel plate.

$f_1\ [Hz]$	$f_2\ [Hz]$	$f_3\ [Hz]$	$f_4\ [Hz]$	CMIF
$2,000$	$12,831$	$35,728$	$71,499$	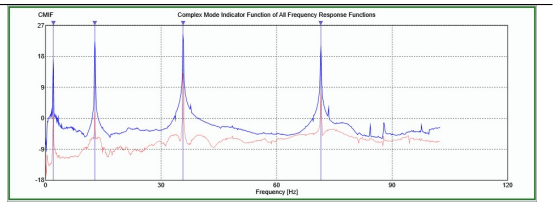

2.3.4 Comparison of methods

In terms of equipment, the data is acquired more easily thanks to the wireless Recovib, but the PCBs could have been used as well. The OMA is a bit simpler since there is no need to synchronize hammer impacts.

In terms of computed frequencies, both techniques are quite close to each other and to the theoretical values. Table 2.5 shows the results of the three computations and the error of the experimental method compared to the analytical one.

Figure 2.21 displays side by side the first mode of vibration computed with the theory (on the left), OMA (in the middle), and EMA (on the right). The mode shape identified with the ambient vibration excitation lack information concerning the top of the structure. This makes sense because no data was collected in that area. Yet for the shape displayed, the bottom part corresponds to what is expected from the theory.
Regarding the shape computed with EMA, more data points are available, how-

ever, the shape is far from what is expected. This can be due to an error in the experimental process or unsuitable equipment. The EMA might be not adapted to detect low-frequency mode shapes.

This experiment shows that the more data points, the more refined the mode shape. If a limited number of sensors is available, those should be placed on the structure at points where the theoretical mode shapes have maximum amplitudes. The conclusion regarding the further experiments is that the EMA might not be suited to investigate chimneys due to limited access to the structure. Impact points can only be made from the ground.

Table 2.5: Comparion of results between the theoretical computation, the OMA model and the EMA model.

Mode	Analytic	OMA	Error OMA	EMA	Error EMA
$f_1\,[Hz]$	$2,04$	$2,00$	$1,9\%$	$2,00$	$1,9\%$
$f_2\,[Hz]$	$12,81$	$13,00$	$1,5\%$	$12,83$	$0,2\%$
$f_3\,[Hz]$	$35,89$	$36,50$	$1,7\%$	$35,73$	$0,5\%$
$f_4\,[Hz]$	$70,32$	$71,60$	$1,9\%$	$71,49$	$1,7\%$

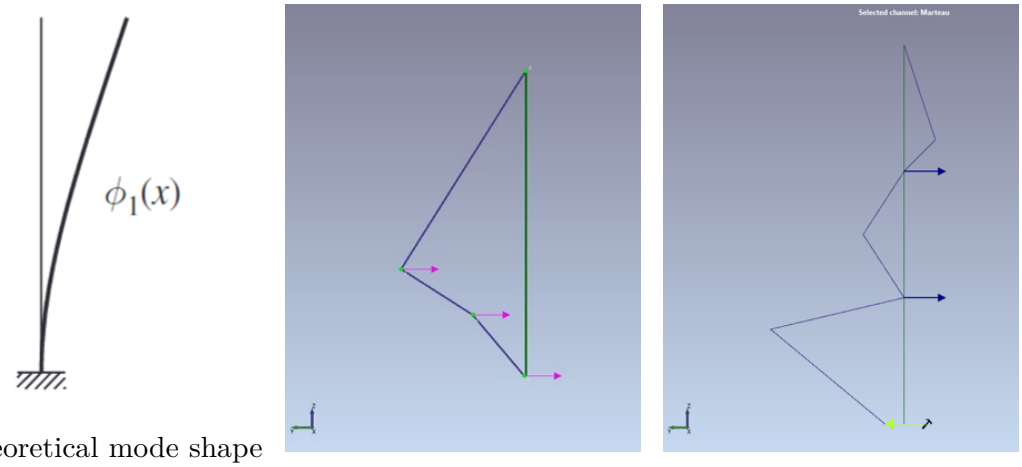

(a) Theoretical mode shape (Anil K. Chopra 2012).

(b) OMA

(c) EMA.

Figure 2.21: First mode shape of the steel plate.

2.4 Transducers

2.4.1 Accelerometers

Transducers used to record accelerations are called accelerometers. There are many techniques to measure accelerations, in this thesis two different types are used: the PCB 393A03 and the Micromega Dynamics Recovib Tiny.

The PCB , on the right in figure 2.22, is a piezoelectric accelerometer, it uses the piezoelectric effect to measure the acceleration. The system consists of a seismic mass over a piezoelectric crystal. The acceleration perceived by the sensor induces the movement of the mass which deforms the crystal, creating an electric signal.

The Recovib Tiny , on the left in figure 2.22, is a Micro Electro Mechanical System (MEMS) accelerometer. It uses a piezoresistive material, e.g. doped silicon, characterized by a piezoresistive coefficient in each direction. By definition, the resistive coefficient of piezoresistive material changes when it undergoes a change in stress. In those sensors, a cantilever seismic mass is attached to its support with piezoresistive elements, used as a gauge, under a continuous voltage. At rest, the system has a certain resistivity, which by Ohm's law, induces a certain current. The movement of the mass induces a deformation of the gauge translated by a change in resistivity, changing the current of the system.

Figure 2.22: 2 accelerometers: Recovib Tiny on the left and PCB 393A03 with a rubber protection on the right. The Recovib Tiny dimensions are $33,439,6\ mm$.

Table 2.6: Comparison of accelerometers specifications.

	PCB 393A03	**Recovib Tiny**
Manufacturer	PCB	Micromega dynamics
Technology	Piezoelectric	Piezoresistive
Mass $[gr]$	210	33,5
Measurements	Relative	Absolute
Axis	Mono-axial	Tri-axial
Measurement range $[g\ pk]$	$+/-5$	$+/-2$
Frequency range $[Hz]$	$0,5$ to 2000	0 to 250
Connectivity	Wired	Data storage

2.4.2 Impact hammer

For EMA, the force of the impact needs to be recorded. For that, a modal hammer is used. It is a hammer with a force sensor in its head, capable of recording the impact force created.
There are many different models of modal hammers, the size, weight, and hardness of the tip depends on its use and on the structure to excite. Manufacturers usually provide a technical sheet to make a choice. Figure 2.23 shows a range of modal hammers from the manufacturer PCB Piezotronics, the largest one has a length of 89 cm. The type of sensor used in those hammers is piezoelectric.
A Piezoelectric sensor consists of a quartz crystal in between two electrodes. The crystal has a high stiffness resulting in very small deformations. When a force is applied to the crystal, the latest is compressed and by the piezoelectric effect, a difference in potential is created. The two electrodes capture this voltage and its magnitude is associated with a force.

Figure 2.23: Impact hammers from PCB Piezotronics. The biggest one has a length of 89 cm and weights $5,5$ kg (*PCB piezotronics, https://www.pcb.com* 2022).

This chapter has helped to understand more deeply the subject at the heart of this thesis. The different theories behind the tools used have been briefly explained to facilitate the reader's understanding.
The notion of industrial masonry chimney has been defined for the purpose of this work. Then a reminder of the theories of the dynamic study of structures was detailed. And finally, the concept of modal analysis in its two different forms was illustrated by an example realized in a laboratory.

Chapter 3

In-situ identification

This chapter presents the field investigation of two different chimneys in the goal of determining their respective modal properties. Both investigations are performed in the surroundings of Porto, Portugal with the help of engineers from the study office NCREP, specialized in structural rehabilitation.

3.1 Chimney in Aguas Santas

The first chimney investigated is located in Aguas Santas in the suburbs of Porto. The red pin on the map in figure 3.1a shows the location of the site around Porto. From a plan point of view, the chimney is located in a wasteland, as shown in figure 3.1b.
This section describes primarily the visual aspects of the chimney and then details the different tests performed in situ in order to determine the chimney's natural frequencies and mode shapes.

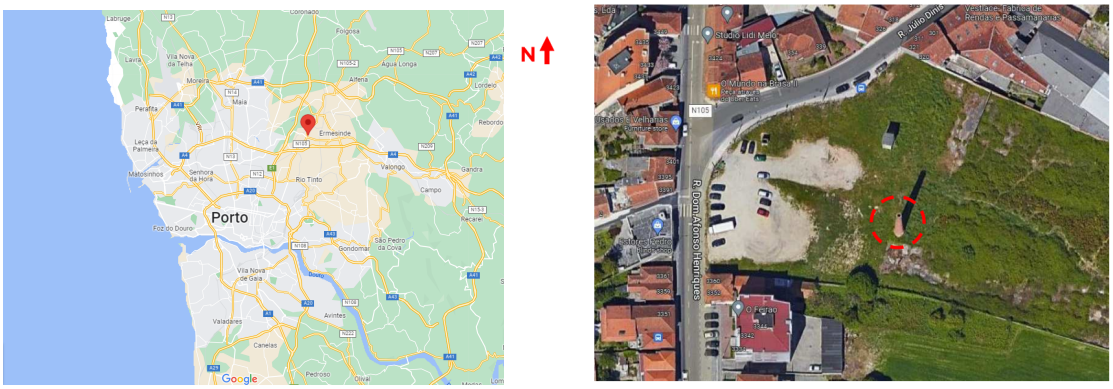

(a) Plan view. (b) Satellite view.

Figure 3.1: Location of the chimney in Aguas Santas (*www.google.com/maps*).

3.1.1 Visual inspection

Geometry Figure 3.2 contains the pictures of the chimney in the four cardinal directions. The chimney has a typical truncated cone shape, it is 30 m high and its largest diameter is $3,30$ m wide at the bottom. The top diameter is $1,2$ m wide. The chimney does not have any base, it is only made of a stack and a crown. Figure 3.3 shows a plaque sealed in the masonry indicating that it was built in 1937. Figure 3.4 shows a tape measure of the bricks indicating they are 20 cm long and 6 cm high.

Damages The bottom of the chimney is covered with ivy up to about 6 m high on the eastern side, the most covered one. The very top of the chimney got also colonized by some vegetation with time, but only just a few weeds as seen in figure 3.5a. The phenomenon is normal since the chimney is not being maintained.
Figure 3.5b shows that some centimeters of joint mortar are missing from the surface. The problem is generalized all around the stack, from the bottom to the top. This problem could have been caused by the washing of the rain, or the normal material degradation over time.
Some areas were restored, some mortar was added to the joints. This effect can be observed in figure 3.5b, where the new mortar has a lighter color than the original one.
A former longitudinal crack can be observed in figure 3.5d. It follows the lightning rod and is only observable because of the lighter color of the new mortar.
Overall, this chimney, which at the time of the investigation was 85 years old, is still in good shape when compared to others found in the literature.

(a) North view. (b) East view. (c) South view. (d) West view.

Figure 3.2: Pictures of chimney in Aguas Santas.

Figure 3.3: Sealed plaque indicating the year of construction.

Figure 3.4: Pictures of chimney's bricks dimensions in Aguas Santas.

(a) Vegetation on the crown.

(b) Missing joint mortar.

(c) Restored area.

(d) Repaired crack.

Figure 3.5: Pictures of chimney's damages in Aguas Santas.

3.1.2 In situ investigation

This section describes the two types of tests made on the structure to determine its modal properties. The chimney was instrumented with two mono-axial PCB 393A03 piezoelectric accelerometers placed at the same point perpendicularly to record two different axes. The accelerometers were set at 7 m high from the ground. Due to the uneven surroundings, it was impossible with the platform provided to reach a higher level.
Figure 3.6 shows the stick diagram model used to model the problem. The two purple arrows indicate the degrees of freedom recorded with the sensors.

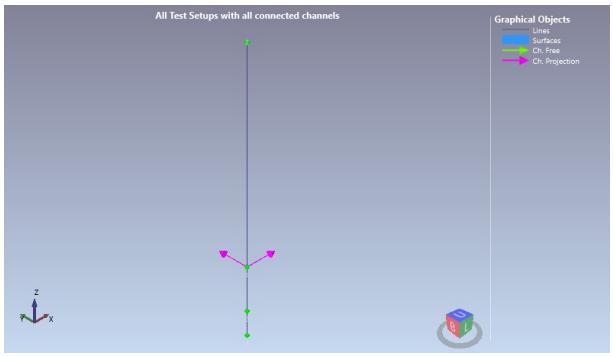

Figure 3.6: Stick diagram for the chimney in Aguas Santas.

OMA

On the first test, only the response from the ambient vibrations perceived by the chimney is recorded during a time slot of 10 min with a sampling frequency of 2048 Hz. The natural frequencies and mode shapes are estimated using the FDD method. With only two accelerometers, the complete mode shape of the chimney cannot be obtained, but still, each mode shape's direction is identified. Figure 3.7 shows the Singular Value Decomposition obtained for the data with peak indicators where the natural frequencies are identified. Table 3.1 displays the natural frequencies values. All mode shapes can be found in Appendix A.

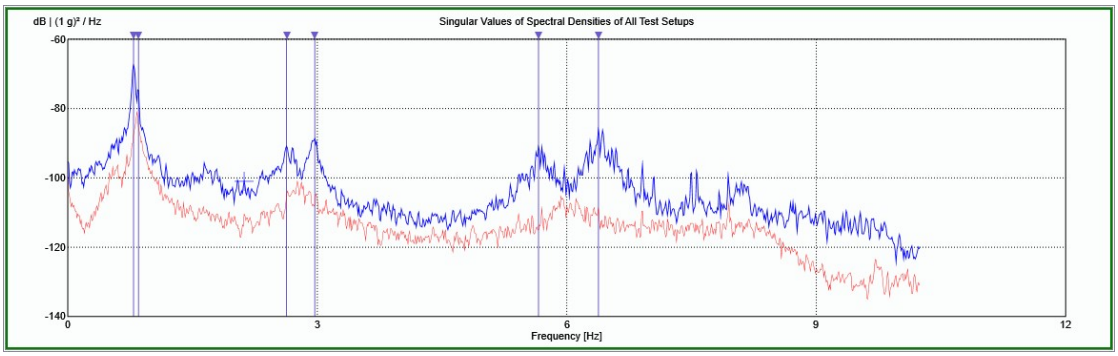

Figure 3.7: Plot of SVD results of the chimney in Aguas Santas. Results from FDD computation.

Table 3.1: Natural frequencies identified with OMA method in Aguas Santas.

$f_{1,x}\ [Hz]$	$0,79$
$f_{1,y}\ [Hz]$	$0,85$
$f_{2,x}\ [Hz]$	$2,66$
$f_{2,y}\ [Hz]$	$2,95$
$f_{3,x}\ [Hz]$	$5,69$
$f_{3,y}\ [Hz]$	$6,40$

EMA

For the second test, an impact hammer is used to artificially excite the chimney. The impact hammer is the model 086D50 from PCB Piezotronics, figure 3.8 shows a picture of this hammer. The accelerometers are still in the same position as previously, at 7 m high from the ground. The impacts are given on a vertical point under the sensors, at a height of 2 m. Picture 3.9 illustrates the experiment, where both the hammer and the wired accelerometers are visible.

Figure 3.8: Impact hammer used for the experiment.

Figure 3.9: Picture of the experiment in Aguas Santas.

To derive the natural frequencies, the CMIF method is used over all the Frequency Response Functions. Unfortunately, as it is visible on figure 3.10, no peak is identifiable.

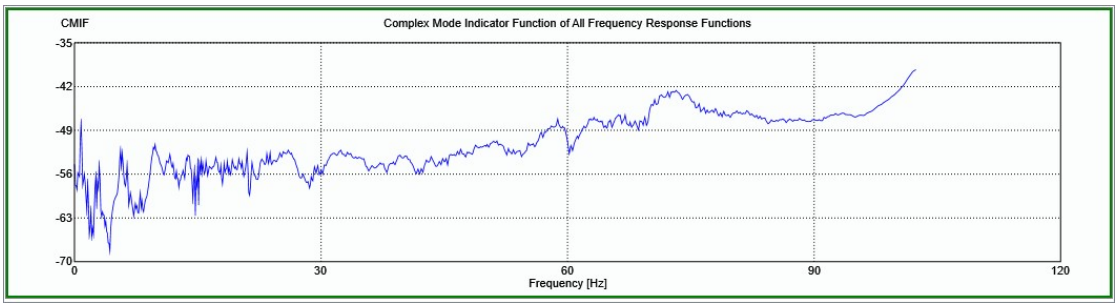

Figure 3.10: CMIF plot for the chimney in Aguas Santas.

3.2 Chimney in Universidade Lusíada

The second chimney is also located northeast of Porto, Portugal. Figure 3.11 indicates the location of the chimney with two different scales. This section describes in a first time the visual observations made during the field investigation and on drawings provided by the site's owner. Then the different in situ tests are performed and their results are detailed.

Figure 3.11: Location of the chimney in Universidade Lusíada (*www.google.com/maps*).

3.2.1 Visual inspection

The chimney is located on university property. From the plan view in figure 3.11, it is observed that the chimney is directly adjacent to a tiny construction and close to a bigger building. Figure 3.12 shows the chimney under the four cardinal directions. The chimney is constituted of three parts: the square base, the truncated conical stack, and an ornamental crown. For more information about the function of each part, please refer to section 2.1.2. The west side of the base is built against a

retaining wall made of stones. On the opposite side, a small opening is visible allowing access into the chimney.

Geometry The base is rectangular parallelepiped with a square base of 2 m and a height of $1,8$ m. It has an opening of $0,4 \times 0,6$ cm on the east side, this was the entry for the fumes. The stack and the crown have a cumulative height of $16,2$ m which gives a total height for the chimney of 18 m. Figure 3.14a is a drawing with the chimney's dimensions. The stack's largest diameter measures $1,6$ m. The opening in the base made it possible to measure the internal diameter of the chimney, which is $0,5$ m. In the picture in figure 3.12d, the axial deformation of the stack towards the southern direction can be noted. The total deformation is 44 cm from the center of the base to the center of the top section, as shown in figure 3.14b.

Material The chimney is made of typical red brick masonry. Along the height, two different colors of bricks can be distinguished. Figure 3.13 shows the separation of those two, the line is located around $11,7$ m high from the ground.

(a) North view. (b) East view. (c) South view. (d) West view.

Figure 3.12: Pictures of chimney in Universidade Lusíada.

Figure 3.13: Demarcation between the bricks of two different colors.

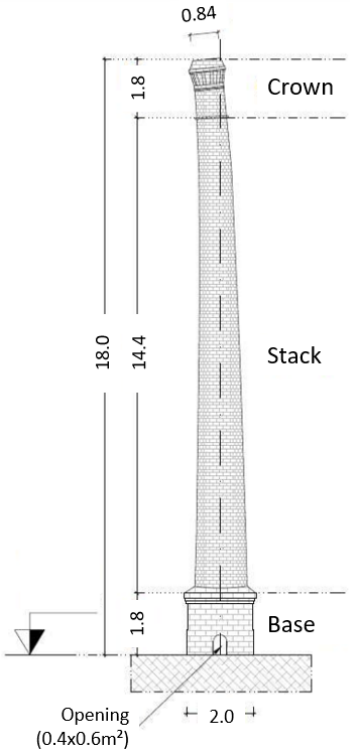

(a) Dimensions in meters of the chimney in Lusíada.

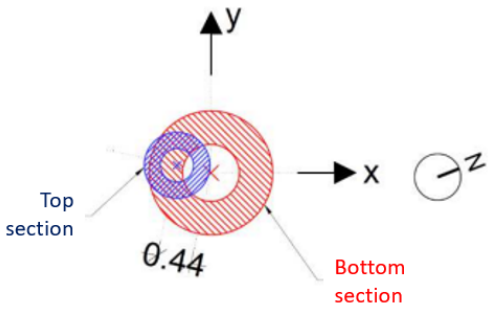

(b) Plan view of the deformation.

Figure 3.14: Drawings of the chimney in Lusíada.

3.2.2 In-situ investigation

OMA

The first test consists of placing a total of seven accelerometers on the structure. Figure 3.15 shows the configuration of the experiment. The nomenclature follows the pattern

$$\text{"Accelerometer}_{\text{index,direction}}\text{"}$$

So a total of three tri-axial Recovib Tiny and four mono-axial PCB 393A03. Figure 3.16 is a picture of the mounting of the sensors on the chimney. For the PCB, an L-shaped steel plate with three holes was screwed into the masonry. The two remaining holes allow the two PCBs to be screwed on the plate. For the Recovib, a steel plate is screwed onto the stack and the sensor is attached to it by two magnets.
Recovib_1, Recovib_2 and Recovib_3 are equally spaced of one third of the total height. PCB_1 and PCB_2 are used as a reference point comparable to Recovib_3 to make it

possible to merge the data captured by PCB_3 and PCB_4 with the one got by the Recovib.
The first frequency for a chimney around 20 m high is about 1 Hz, so in order to catch correctly the low frequencies, the minimum recording time should be

$$t > \frac{1000}{f_1} = \frac{1000}{1\ s} = 1000\ s = 16,67\ min \tag{3.1}$$

The recording time period was set to an even 20 minutes.
An example of the accelerations recorded by the Recovib and PCB are displayed in figure 3.17a and 3.17b respectively. The highest sensitivity of the PCB is well noticed with the reduction of captured noise.

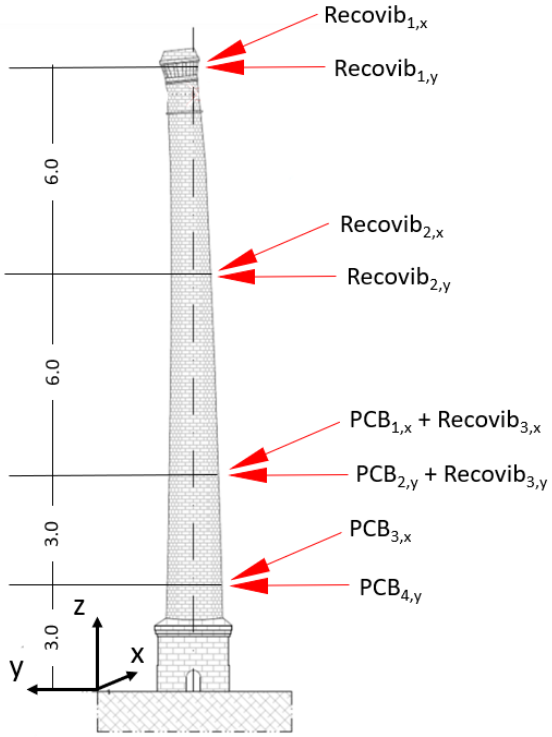

Figure 3.15: Sketch of the OMA test setup. Dimensions in meter, sensors in red.

Figure 3.16: Mounting of the accelerometers on the chimney.

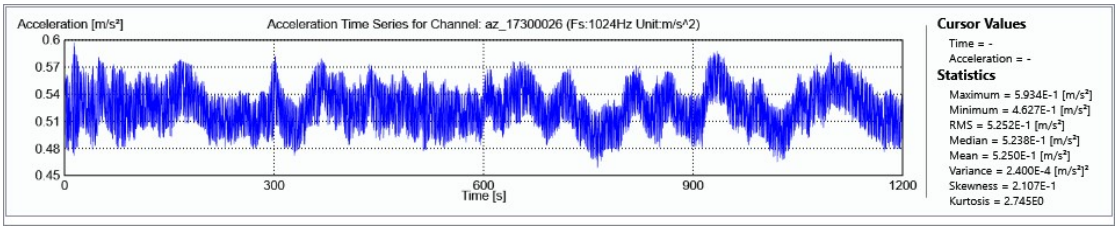

(a) Accelerations recorded in the y-direction by a Recovib Tiny.

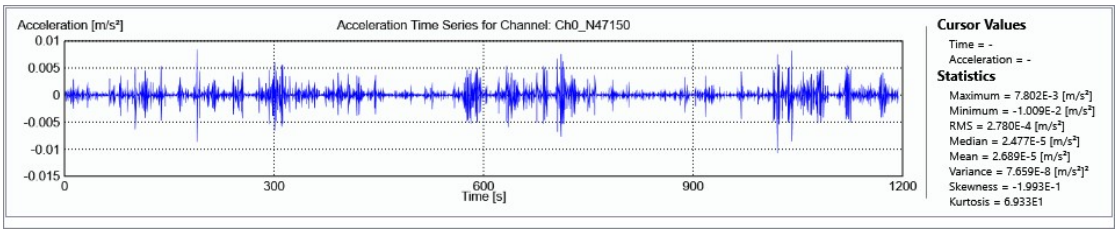

(b) Accelerations recorded in the y-direction by a PCB sensor.

Figure 3.17: Time-domain accelerations.

The SVD of the Spectral densities is plotted in figure 3.18, the FDD method was used to identify the natural frequencies and vibration mode shapes. Table 3.2 summarizes the eight natural frequencies identified. The index 1, as in $f_{1,x}$, refers

to the shape of the first mode and the letter x to its main direction. There are then eight natural frequencies identified for five different vibration mode shapes.

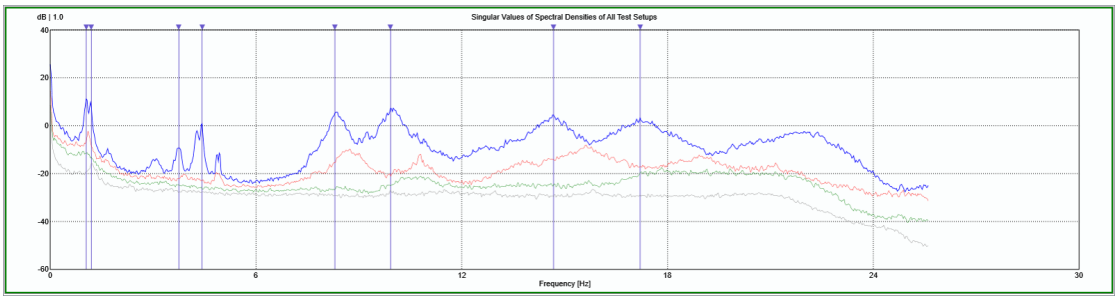

Figure 3.18: SVD plot for the chimney in Lusíada.

Table 3.2: Natural frequencies identified with OMA method.

$f_{1,x}\ [Hz]$	$1,056$
$f_{1,y}\ [Hz]$	$1,175$
$f_{2,x}\ [Hz]$	$3,717$
$f_{2,y}\ [Hz]$	$4,386$
$f_{3,-xy}\ [Hz]$	$8,301$
$f_{3,xy}\ [Hz]$	$9,943$
$f_{4,x}\ [Hz]$	$14,608$
$f_{5,x}\ [Hz]$	$17,200$

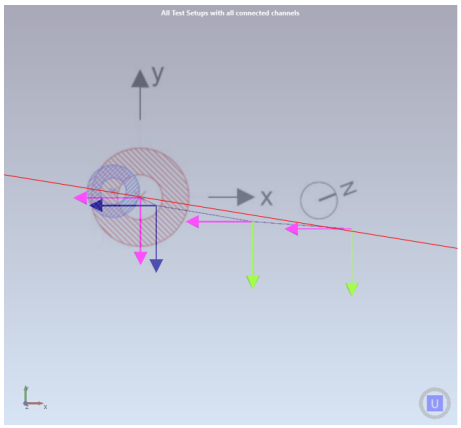

Figure 3.19: Mode shape orientation regarding the chimney deformation.

The visual expressions of the modes of vibration are displayed in table 3.3 and table 3.4. The first column indicates the value of the corresponding natural frequency, the second is the quad view directly provided by the software ARTeMIS modal. The last column displays the modes in a 2D plane for more clarity.
An observation can be made regarding the mode shapes' orientations. Figure 3.19 shows the top view of the chimney's drawing overlaying the top view of the mode shape associated with the frequency $f_{1,x}$. The red line goes through the centers of both the bottom and top sections of the chimney's stack, marking the orientation of the chimney's initial deformation. It is clear that the orientation taken by the shape of the vibration mode is strongly influenced by the initial deformation.
Regarding the mode associated with the frequency $f_{1,y}$, this one takes a shape similar to the first one but with an orientation of 90°.

Table 3.3: Frequencies and mode shapes of the chimney in Lusíada (1/2).

Frequency	Quad view	2D view
$f_{1,x} = 1,056\ Hz$	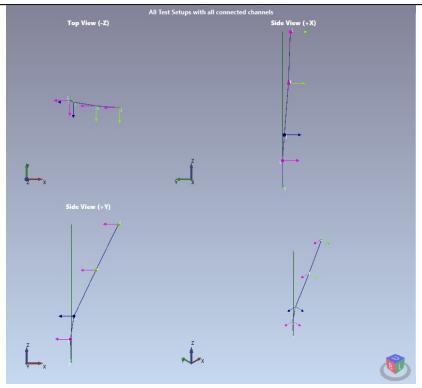	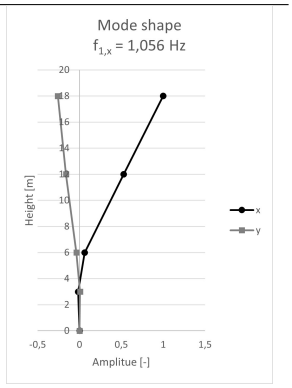
$f_{1,y} = 1,175\ Hz$	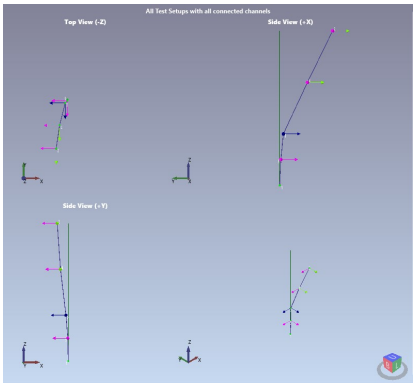	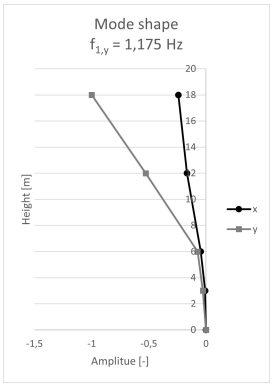
$f_{2,x} = 3,717\ Hz$	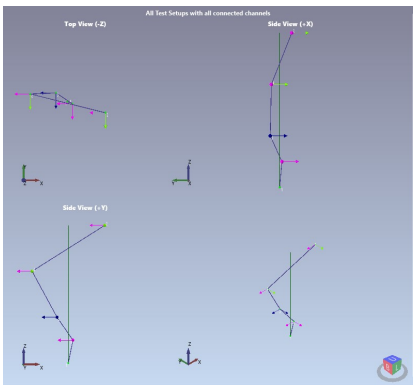	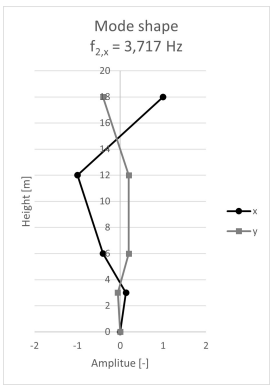
$f_{2,y} = 4,386\ Hz$	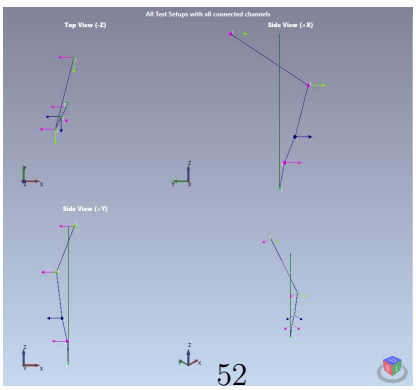	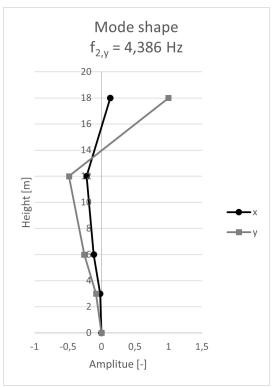

Table 3.4: Frequencies and mode shapes of the chimney in Lusíada (2/2).

Frequency	Quad view	2D view
$f_{3,-xy} = 8,301\ Hz$	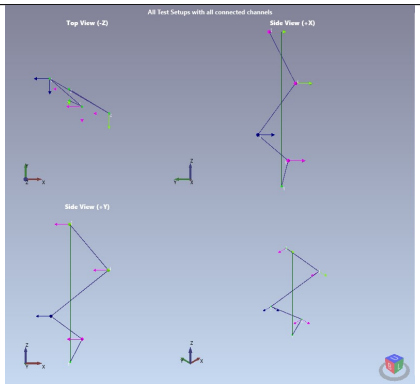	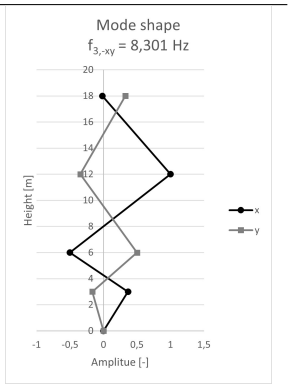
$f_{3,xy} = 9,943$	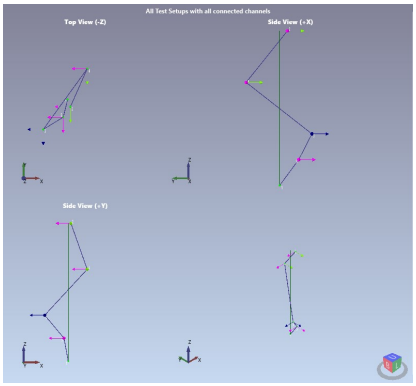	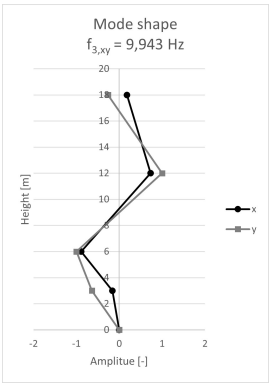
$f_{4,x} = 14,608\ Hz$	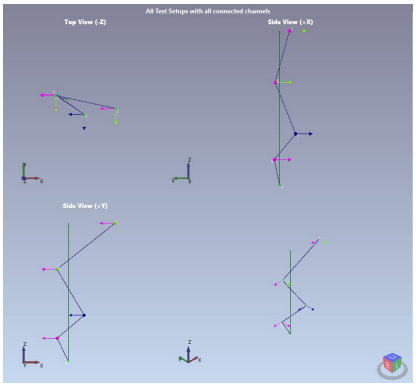	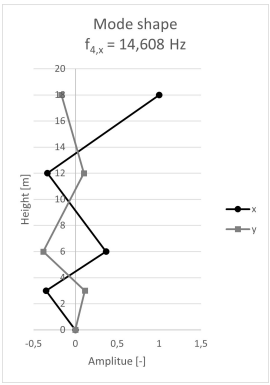
$f_{5,x} = 17,200\ Hz$	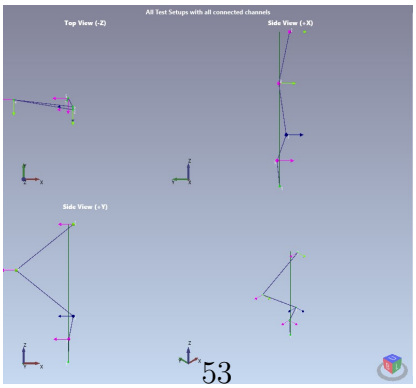	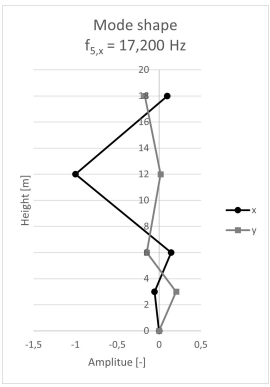

EMA

The following modal test is performed using four PCB 393A03 accelerometers recording the structure's response at two different locations, in two perpendicular directions for each location, one radial and one tangential to the chimney's stack. Three different locations are excited with a modal hammer, the first one on the chimney's base and the two others in between the two recorded points. Figure 3.20 illustrates the experiment. The sketch is not to scale for clarity reasons and the lettered indexes indicate the axis of interest.

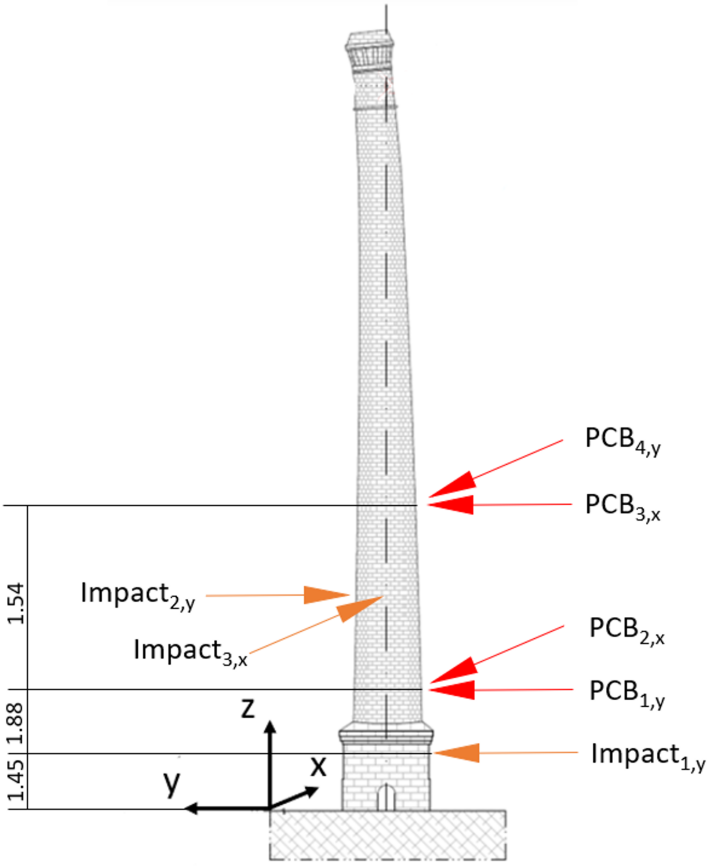

Figure 3.20: Sketch of the EMA test setups in Lusíada. Dimensions in meter, sensors in red, hammer impacts in orange. The sketch is not to scale.

Using the Complex Mode Indicator Function of all the frequency response functions, four natural frequencies and two different modes of vibration are identified. Figure 3.21 displays the CMIF plot. The first SVD line has four slight peaks, more pronounced peaks were expected. The first identified natural mode of vibration has

a related frequency $f_{1,x} = 8,177\ Hz$. Table 3.5 displays the rest of the frequencies identified. Figure 3.22 displays the quad view illustrations of the mode shapes. The only information that can be drawn from those modes are their orientations (from the top view in the left upper corner of each picture). For the shape itself, there is not enough information to know how the structure could vibrate.

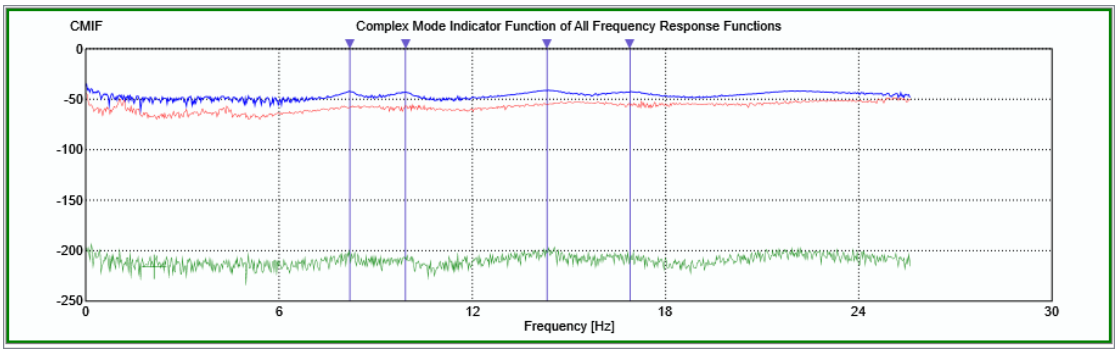

Figure 3.21: CMIF plot for the chimney in Lusíada.

Table 3.5: Natural frequencies identified with EMA method.

$f_{1,x}\ [Hz]$	$8,177$
$f_{1,y}\ [Hz]$	$9,859$
$f_{2,x}\ [Hz]$	$14,339$
$f_{2,y}\ [Hz]$	$16,876$

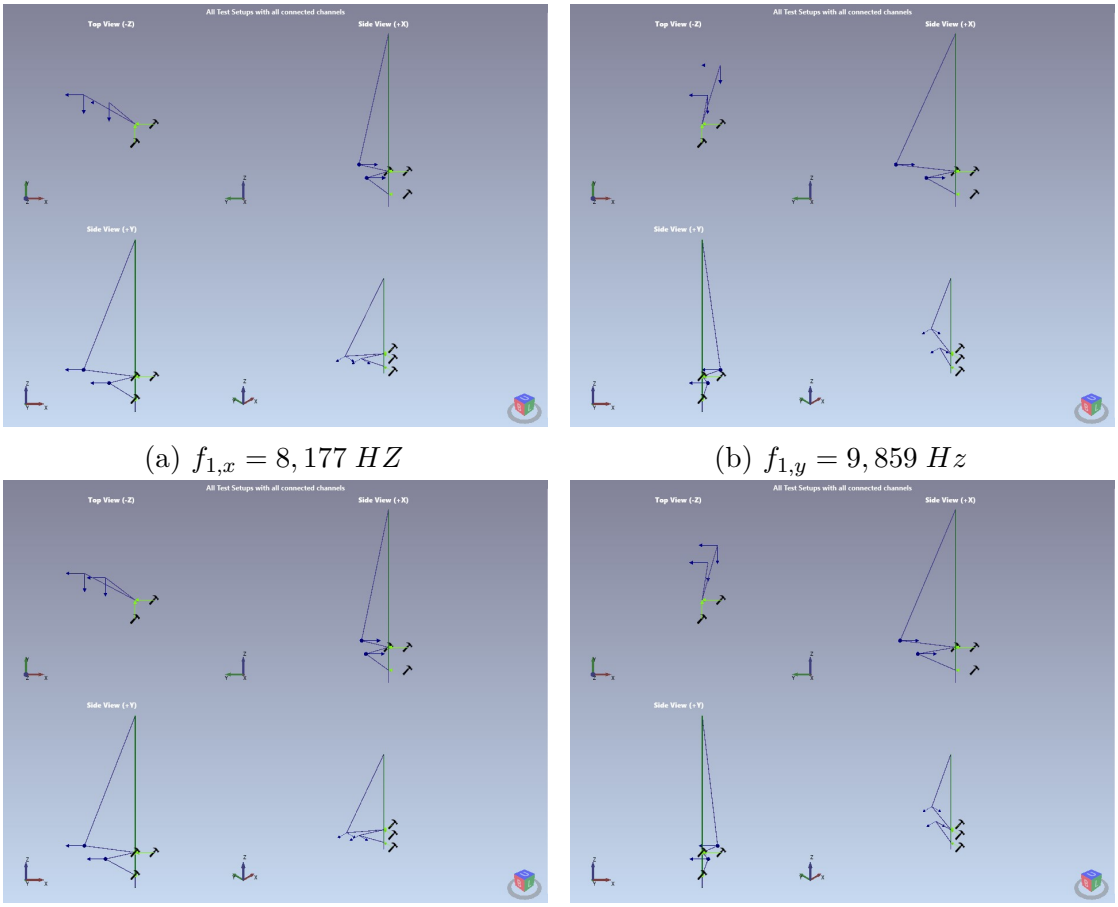

(a) $f_{1,x} = 8,177\ HZ$ (b) $f_{1,y} = 9,859\ Hz$

(c) $f_{2,x} = 14,339\ Hz$ (d) $f_{2,y} = 16,876\ Hz$

Figure 3.22: Quad view of the mode shapes found with the EMA and their associated frequencies.

3.3 Conclusion for both investigations

Aguas Santas

In the first investigation, the operational modal analysis permitted to identify six different natural frequencies. Unfortunately, the lack of sensors did not allow to determine correctly the vibration modes.
The tests with the impact hammer were not conclusive, no natural frequency could be found.

Lusíada

On the chimney in Lusíada, the OMA produced great results with the set of seven accelerometers set along the height of the structure. Natural frequencies and mode shapes could be determined precisely. A link between the initial deformation of the stack and the orientation of the vibration modes was established.
On the other hand, the EMA even with four sensors and three impact points could not identify the lower frequencies. A further study could be considered to determine the cause of this effect.

General

Because one of the purposes of this work is to perform a calibration based on the modes of vibration in addition to the natural frequencies, only the chimney in Lusíada is kept to pursue the work. The data retained to pursue the investigation is the one obtained through operational modal analysis.

Chapter 4

Numerical model

This chapter explains the creation of numerical models for the chimney in Lusíada. It details the assumptions taken on the geometry of the structure, its boundary conditions, and its materials.
For this matter, the Fiber Element-based software SeismoStruct is operated (Seismosoft 2022). The software is able to compute the behavior of frame structures exposed to static or dynamic loading. It takes into account the geometry nonlinearities as well as the nonlinear behavior of materials.

In SeismoStruct, one element is defined by a section between two nodes. There are several *Element Classes* available, for the purpose of this study all structural elements are Beam type elements *Inelastic frame force based element - infrmFB* [1] with five integration sections, as recommended by the developers. When performing a linear elastic analysis, those elements give the same results as an Euler-Bernoulli beam element.

Four models are created, and the assumptions taken regarding the real structure, mainly the geometry and material properties, are detailed in this chapter. The results leading to the determination of the values of their parameters are detailed in chapter 5.

[1] SeismoStruct defines this class as a "force-based 3D beam-column element type capable of modeling members of space frames with geometric and material nonlinearities".

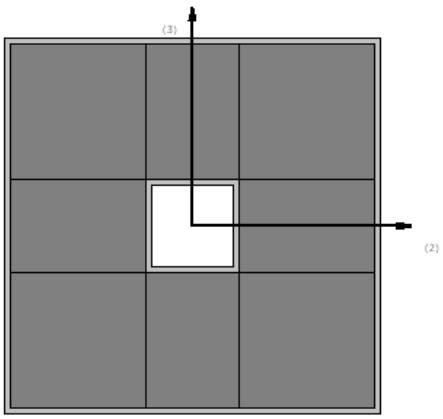

Figure 4.1: Cross section of the base used for the numerical model.

4.1 Structural assumptions

4.1.1 Sections geometry

The base The in-situ investigation, section 3.2, showed that the base of the structure is a parallelepiped rectangle with a square base and a circular hole at its center. It is $1,8\ m$ high with sides of $2\ m$ long, and the internal hole diameter is $0,5\ m$ wide.
However, in SeismoStruct, there is no square cross-section with a circular hole in its center. The closest design to it is a rectangular hollow cross-section with a central rectangular hole, the cross-section is illustrated in figure 4.1. Four parameters are needed to define this cross-section: the external and internal lengths and widths. The section has an external length and width of $2\ m$. For the internal circular hollow section, a square surface equivalence has been defined based on the diameter of the hole.

$$\text{hole diameter: } d_{hole} = 0,5\ m$$
$$\Rightarrow Area_{hole} = \frac{\pi \cdot d_{hole}^2}{4} = 0,196\ m^2$$
$$\text{Equivalent square side: } a = \sqrt{Area_{hole}} = 0,443\ m$$

So both the internal length and width are taken to be $0,443\ m$.

The stack he stack has hollow circular sections as shown in figure 4.2. As explained in section 2.1.2, the construction techniques of masonry chimneys of the time made that the top section thickness is usually two bricks of 11 cm wide. Along the height, the stack is constituted of several parts of equal length with different cross-section thicknesses multiple of the width of one brick. The lowest cross section is the thickest, then going up the cross section's thickness is reduced brick by brick.
The length of each part is deducted from the height of the structure and the thickness of the cross-section near its base.

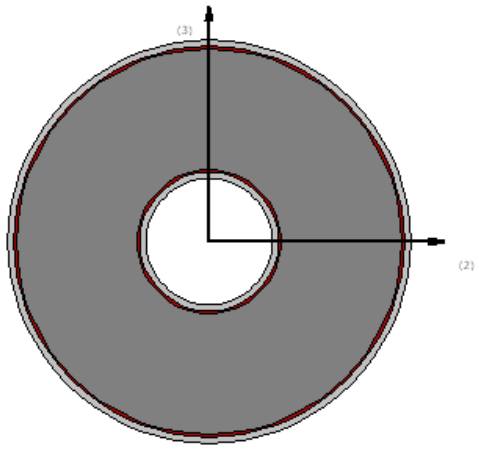

Figure 4.2: Cross section of the stack used in the numerical model.

4.1.2 Material constitutive model

SeismoStruct offers a numerous collection of constitutive material models. The constitutive model used to simulate the masonry's behavior is the *Mander et al. nonlinear concrete model*. The material property values are defined in the next section, section **??**, but some ranges of values can be delimited. The literature shows that the Modulus of elasticity value considered for the calibration should be between $1,5$ and $6,5\ GPa$ and the density between 16 and 19 kN/m^3. However, a value of $E = 1,5\ GPa$ corresponds to masonry in a very bad shape, therefore a higher bound value of $2,5\ GPa$ is taken. For the compressive strength, the value of

$$f_c = \frac{E}{700}$$

can be taken for an aged masonry (Guedes et al. 2019).
The tensile strength is set to a very low value. We will see later that for the

response spectrum analysis, as this analysis is pseudo-elastic and so conservative, a value of $f_t = 0\ kPa$ will be adopted. However, for the time history analysis, a value of zero can sometimes lead to convergence error, therefore a low value of $f_t = 40\ kPa$ will be taken for this analysis.
As the constitutive material is supposed to model reinforced concrete, it asks for reinforcement properties. The problem is overcome by setting the reinforcement ratio to zero.
The stress-strain diagram for a *Mander et al. nonlinear concrete model* with a compressive strength $f_c = 3571\ kPa$, a tensile strength of $f_t = 40\ kPa$ and a Modulus of elasticity of $2,5\ GPa$ is displayed in figure 4.3.

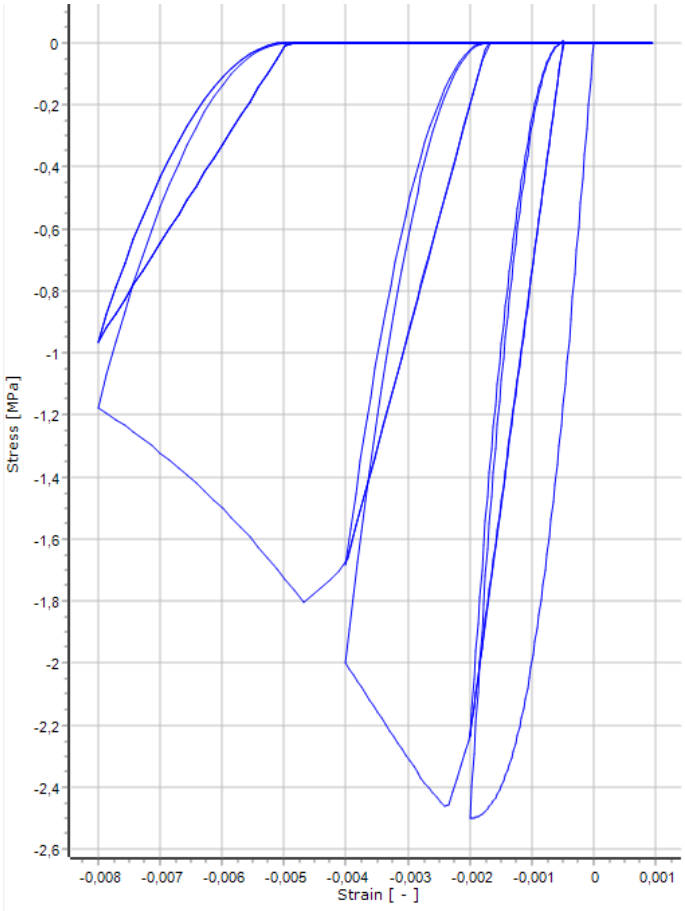

Figure 4.3: Mander et al. constitutive model.

4.1.3 Number of elements

In SeismoStruct, a structure can be seen as nodes linked with elements. This section studies the impact of the number of elements on the final results.

To determine the number of elements to use, five models, based on the same geometry but with five different numbers of elements are compared. The first model has five elements, one for the base and four for the stack. The others keep one element for the base but double the number of elements for the stack. In definitive there are five models with 5, 9, 17, 33 and 65 elements. Figure 4.4 illustrates the five variations of the model. The nodes are in light green and the elements are in dark green.
To be satisfactory, the percentage in error for the frequency value between the two models should be less than 1%. This way the value to the hundredth can be considered as correctly calculated. For each frequency, the percentage in error is calculated as follows

$$\text{Error} = \frac{f_i - f_{i-1}}{f_{i-1}} \tag{4.1}$$

With i the index referring to the different models.
The results are displayed in table 4.1, the first model to have all his errors smaller than 1% is the one with 33 elements. Therefore the four models presented in the following sections are made of 33 elements.

Table 4.1: Frequencies obtained with the same model declined with different number of elements.

	Number of elements					Error			
	5	**9**	**17**	**33**	**65**				
$f_1\,[Hz]$	1,029	1,066	1,075	1,077	1,078	3,5%	0,9%	0,2%	0,1%
$f_2\,[Hz]$	1,029	1,066	1,075	1,077	1,078	3,5%	0,9%	0,2%	0,1%
$f_3\,[Hz]$	3,760	4,090	4,182	4,205	4,211	8,8%	2,2%	0,6%	0,1%
$f_4\,[Hz]$	3,761	4,091	4,182	4,206	4,212	8,8%	2,2%	0,6%	0,1%

4.2 Model 1

Starting from the base, its section geometry is the one presented in the previous section, section 4.1.1. All models consider the same cross section for the base, they differ from the assumptions made for the stack and the foundation. In Model 1,

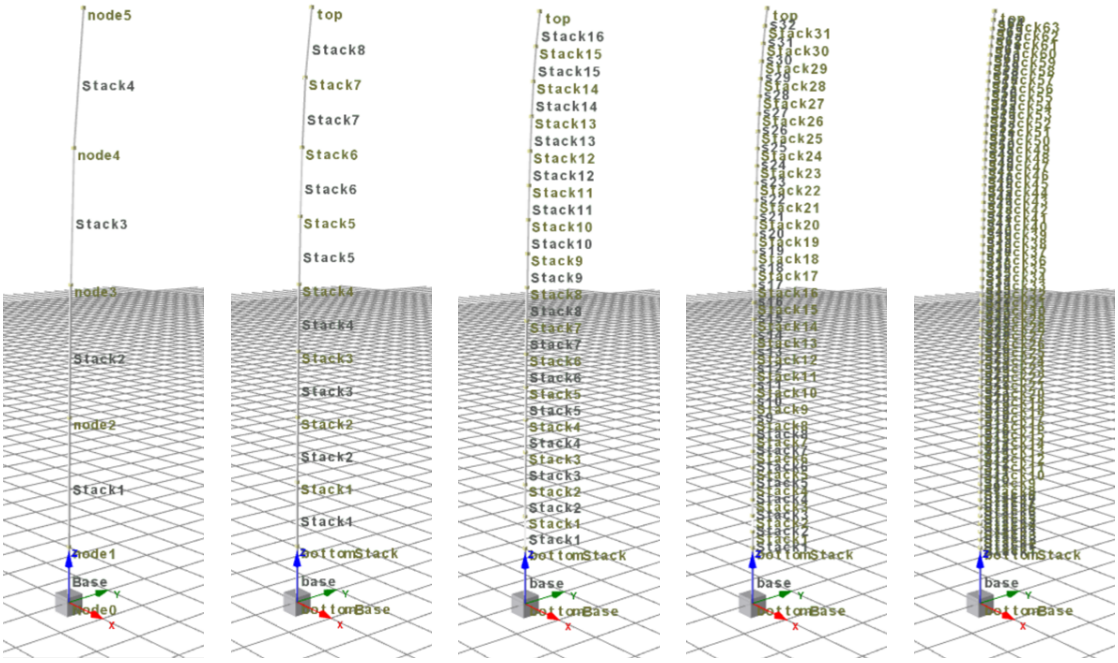

(a) 5 elements. (b) 9 elements (c) 17 elements. (d) 33 elements (e) 65 elements.

Figure 4.4: Discretization of the number of elements.

the structure is supposed embedded in the ground.

Knowing the stack's lowest external diameter and that of the internal hole, a thickness of $0,55\ m$ is taken into account for the cross-section. The difference between the thickness at the bottom and the one at the top of the stack gives the number of sections along the height.

$$\text{Number of sections} = \frac{\text{Lowest thickness} - \text{Top thickness}}{\text{Brick's width}} + 1 \tag{4.2}$$

$$= \frac{0,55 - 0,22}{0,11} + 1 \tag{4.3}$$

$$= 4 \tag{4.4}$$

There are then four different cross sections along the height. All sections are considered to be the same length. Each section has a length of

$$\text{Length of one section} = \frac{\text{Total height} - \text{Base height}}{\text{Number of sections}} \tag{4.5}$$

$$= \frac{18 - 1,8}{4} \tag{4.6}$$

$$= 4,05\ m \tag{4.7}$$

The final estimated geometry used for Model 1, representing the chimney in Lusíada, is drawn in figure 4.5a. From the bottom up, there is first the element modeling the base, then the stack is divided into four equal parts of $4,05\ m$ each. The lowest thickness of the stack's section is $0,55\ m$ and then it goes to $0,44\ m$, $0,33\ m$, and finally $0,22\ m$ for the upper part.
As the chimney is not perfectly straight, the nodal coordinates were retrieved from drawings to simulate the initial deformation. Figure 4.5c shows the initial deflection following the Y-axis.
To ease to model creation, a constant internal diameter for the stack's sections was taken and the variation in thickness is translated with a variation of the external diameter. That is why in figure 4.5b, the chimney has an external stair-like shape.

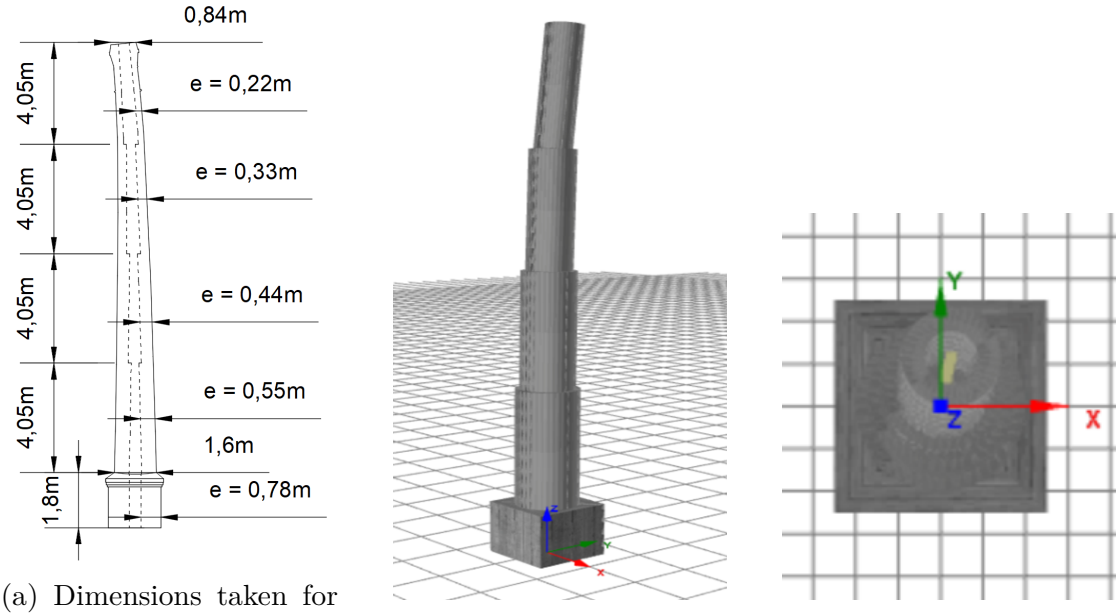

(a) Dimensions taken for the Model 1.

(b) Model 1.

(c) Top view.

Figure 4.5: Model 1 dimensions and numerical view.

4.3 Model 2

This model is based on the assumption that the chimney was built at two different times. Indeed, in section 3.2 in chapter 3, it was noticed that the upper part of the chimney was made of a darker brick color. The assumption is that this upper part was built at a second time, maybe even rebuilt due to a former failure and so is more recent and made of a material with different properties than the lower part. Regarding the geometry, it is assumed that this part was built on its entire length with a thickness of only two bricks. Figure 4.8 shows the geometry assumed for this model.

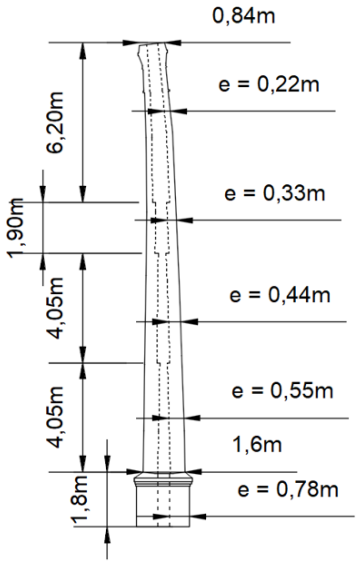

(a) Dimensions taken for the Model 2.

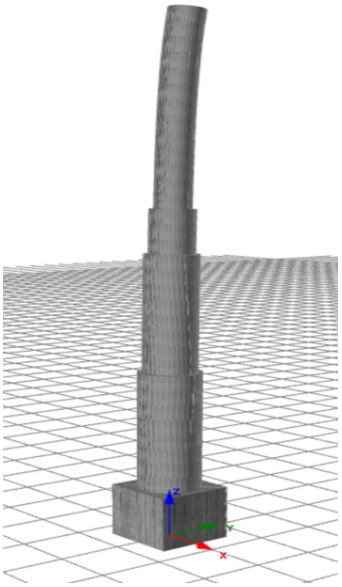

(b) Model 2.

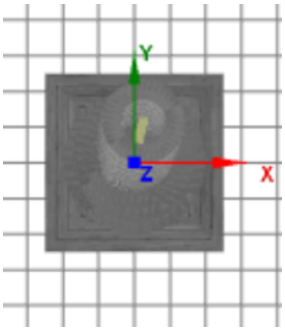

(c) Top view.

Figure 4.6: Model 2 dimensions and numerical view.

4.4 Model 3

For this model, the same geometry as Model 1 is used, the difference lies in the assumptions regarding the soil. In Model 1, the structure is assumed to be a perfect embedded cantilever, where Model 3 models a non-rigid foundation. For that purpose, a rotational spring, with a rotational stiffness K, is defined at the lowest node. The spring takes the assumption that its stiffness is equal in both X and Y directions. Figure 4.7 illustrates this difference with a sketch.
In SeismoStruct, the modeling of this non-rigid foundation is performed with a *Link element type* used to join two nodes. This type of element is defined by a linear symmetric relationship between the moment and the rotation. The parameter to be set is the rotational stiffness chosen.

(a) Cantilever. (b) Cantilever with rotational spring.

Figure 4.7: Static diagrams.

4.5 Model 4

Model 4 is intended to be closer to the real geometry. The previous geometries made the assumptions that the internal diameter is constant along the height and that the reduction in thickness is done from the outside. In this model, the internal diameter is no longer considered fixed along the height, only the thicknesses are. The tapered outside shape is taken into account. The dimensions taken into account for the different parts of the model can be found in figure 4.8a. Figure 4.8b and figure 4.8c shows an external view and a top view of the numerical model.
Figure 4.9 overlays the cross sections of Model 3 and Model 4. The cross-sections for the base are equal, the differences lay in the stack. The orange line describes the Model 3 geometry, where the reduction steps are observed on the outside of the stack. Model 4 (in blue) on the other hand has a continuous external shape and the reduction steps are made from the inside.
This model takes the same assumptions as Model 3 regarding the foundation.

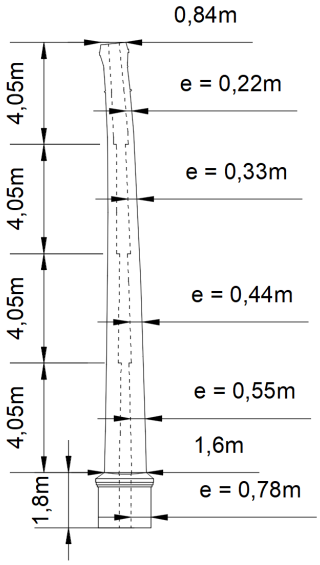

(a) Dimensions taken for the Model 4.

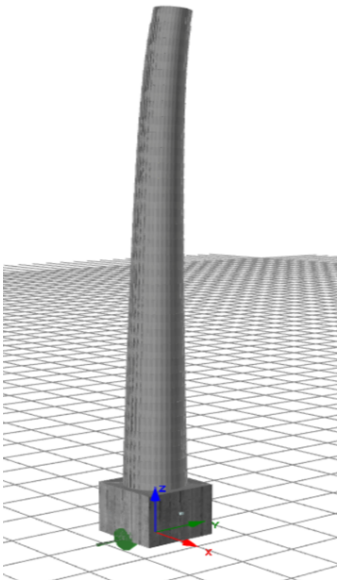

(b) Model 4.

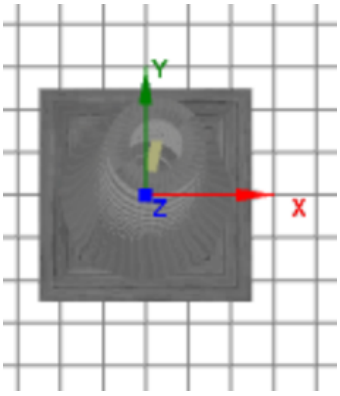

(c) Top view.

Figure 4.8: Model 4 dimensions and numerical view.

4.6 Conclusion

This section explained the different assumptions made to create four different numerical models. Starting with the cross sections and the constitutive materials, then the global geometries were presented.
Four different models are elaborated, each one with its own specificity. The use of these models will try to highlight the impact of geometric assumptions that can be made for a single structure on the results.

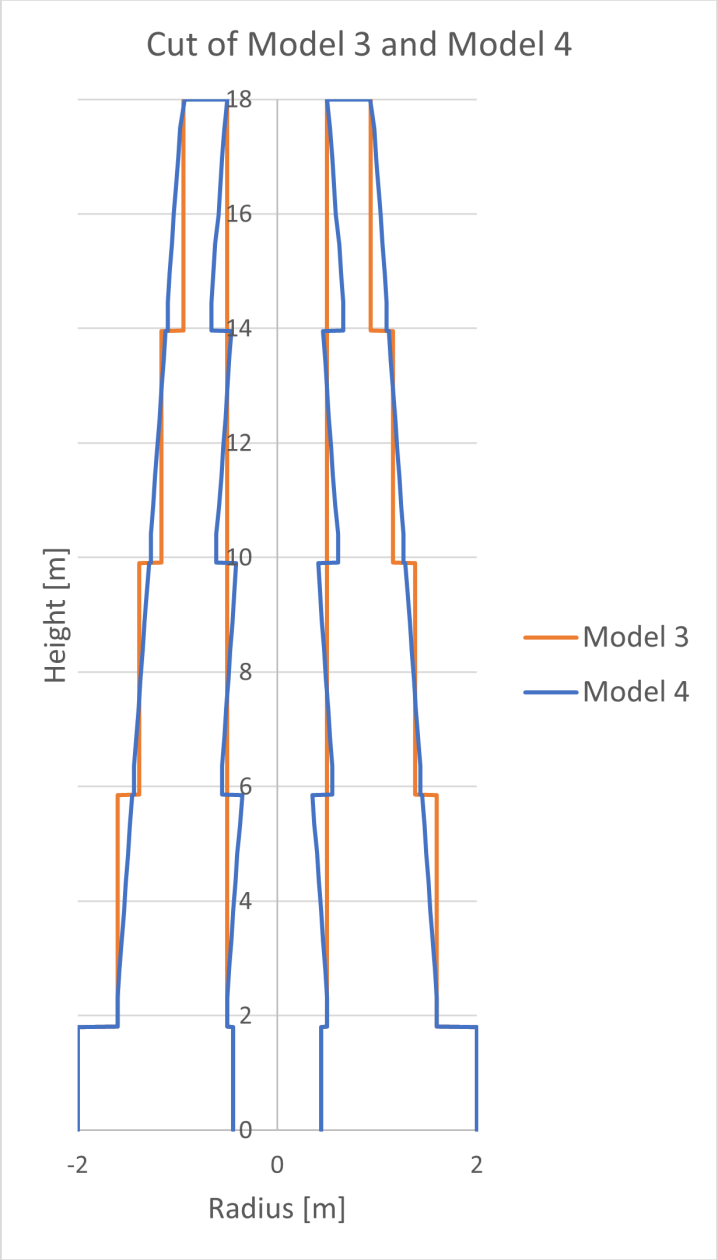

Figure 4.9: Cross section of Model 3 and Model 4.

Chapter 5

Calibration

This chapter presents the process implemented to calibrate the four models defined previously to the data acquired experimentally.
The first section presents the mathematics tools used to compare the numerical results with the experimental ones. Followed by the actual results of the parameters estimated for each model. And to close this section, a discussion of the results is elaborated to select a model to pursue the analysis.

5.1 Fitness functions

The fitness functions, as the name indicates, are mathematical tools used to describe how well a model fits the experimental results.
To this end, two functions are presented, one comparing the frequencies and the second focusing on the correspondence of vibration modes.

The first function is used to compare the natural frequencies found during the experimental investigation and the one computed by the numerical model (Lacanna et al. 2020). Equation 5.1 only accounts the error in frequencies.

$$\mathrm{H}_f(k) = \sum_{i=1}^{k} \left(\frac{f_{i,n} - f_{i,e}}{f_{i,e}} \right)^2 \tag{5.1}$$

With k the number of frequencies used for the fitting of the numerical model. Here $k = 4$ like this the first four natural frequencies are compared, corresponding to two modes of vibration in two different directions. The index n is used to designate the frequencies found *numerically*, and e *experimentally*.

To compare the modes of vibration, the Modal Assurance Criterion is commonly used. It takes as entry two vectors, as it is expressed in equation 5.2:

$$\mathrm{MAC}\left(\phi_{i,n}, \phi_{i,e}\right) = \frac{\left|\phi_{i,n}^T \phi_{i,e}\right|^2}{\left(\phi_{i,n}^T \phi_{i,n}\right)\left(\phi_{i,e}^T \phi_{i,e}\right)} \tag{5.2}$$

The MAC value is a scalar defined between 0 and 1, taking the value of 1 if both vectors are fully consistent. A MAC value higher than $0,8$ can be seen as a "good" fit of the numerical model over the experimental data (Lopes et al. 2009).

However, the MAC value does not take into account the value of the frequency associated to the vector. To compensate for this lack of consideration, the *Modified Total Modal Assurance Criterion* is defined. It is expressed in equation 5.3.

$$\mathrm{H}_m(k) = \mathrm{MTMAC} = \prod_{i=1}^{k} \left[\frac{\mathrm{MAC}\left(\phi_{i,n}, \phi_{i,e}\right)}{1 + \left(\frac{f_{i,n}^2 - f_{i,e}^2}{f_{i,n}^2 + f_{i,e}^2}\right)} \right] \tag{5.3}$$

The MTMAC value is also a scalar defined between 0 and 1, taking the value of 1 if both vectors and frequencies are identical.

5.2 Models

For each model the calibration process is similar. The parameters are changed manually and iterated to reach the model with the smaller value for the fitness function H_f and the largest one for the MTMAC value.
In the following subsections, the results for each retained model are presented. First, the parameters given the best model, then the natural frequencies computed numerically as well as the results of the fitness functions. And finally, graphs of the vibration modes, containing both the experimental and numerical mode shapes, are presented.

The modulus of elasticity E and the density γ are iterated with steps of $0,5$. The soil's stiffness K is assumed to be equal in both directions, X and Y, therefore no distinction is made. K is iterated using steps of $50\,000\ kNm/rad$.

5.2.1 Model 1

Parameters

For this model, the parameters to define are the masonry density γ and the masonry modulus of elasticity E.
Table 5.1 gives the parameters adopted after calibration for Model 1.

Table 5.1: Parameters used for Model 1.

$E\ [GPa]$	$\gamma\ [kN/m^3]$
$1,5$	19

Results

Table 5.2 displays the values of the fitness functions obtained after calibration. Table 5.3 compares the experimental and numerical frequencies computed with Model 1. It also indicates the mode shape associated with each frequency. Table 5.4 is a double entry matrix comparing the MAC value computed between the experimental and numerical mode shapes.

Table 5.2: Fitness functions results of Model 1.

$H_f\ [-]$	$H_m\ [-]$
$0,03$	$0,56$

Table 5.3: Numerical frequencies and their associated mode for Model 1.

	Experimental	Numerical	Associated mode
$f_{1,x}\ [Hz]$	$1,056$	$1,105$	ϕ_1
$f_{1,y}\ [Hz]$	$1,175$	$1,105$	ϕ_2
$f_{2,x}\ [Hz]$	$3,717$	$4,314$	ϕ_3
$f_{2,y}\ [Hz]$	$4,386$	$4,314$	ϕ_4

MAC matrix

Table 5.4: MAC matrix of Model 1.

MAC	$\phi_{1,e}$	$\phi_{2,e}$	$\phi_{3,e}$	$\phi_{4,e}$
$\phi_{1,n}$	$\mathbf{0,983}$	$0,007$	$0,110$	$0,006$
$\phi_{2,n}$	$0,010$	$\mathbf{0,983}$	$0,015$	$0,341$
$\phi_{3,n}$	$0,444$	$0,000$	$\mathbf{0,793}$	$0,006$
$\phi_{4,n}$	$0,000$	$0,438$	$0,005$	$\mathbf{0,950}$

Mode shapes

Here is a visual comparison of the mode shapes. The first four modes of vibration obtained for the structure are presented.

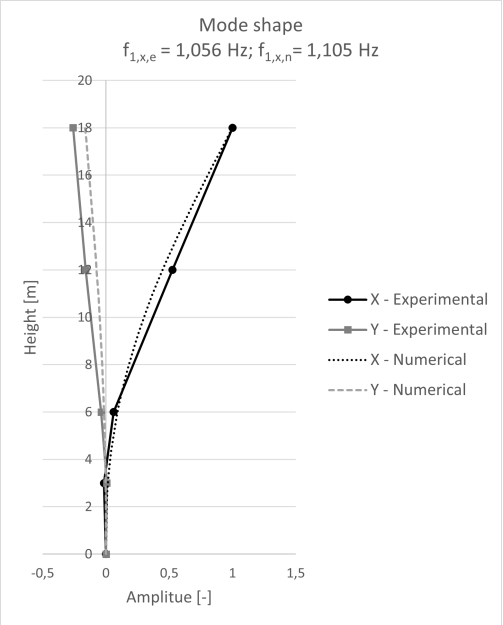

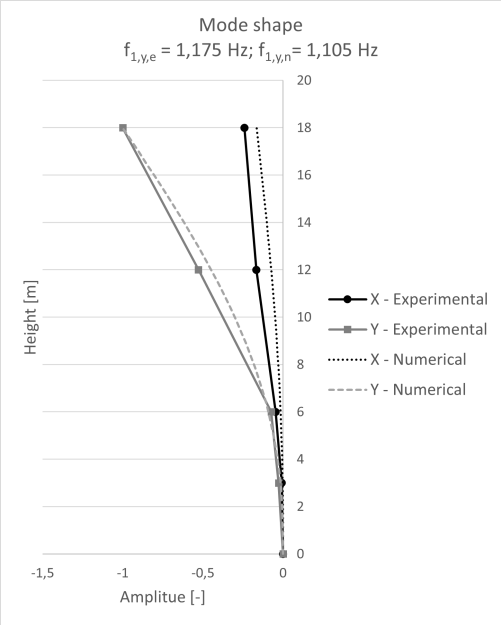

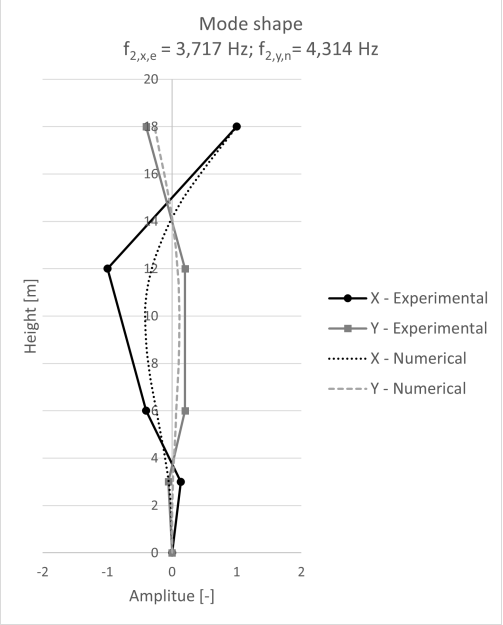

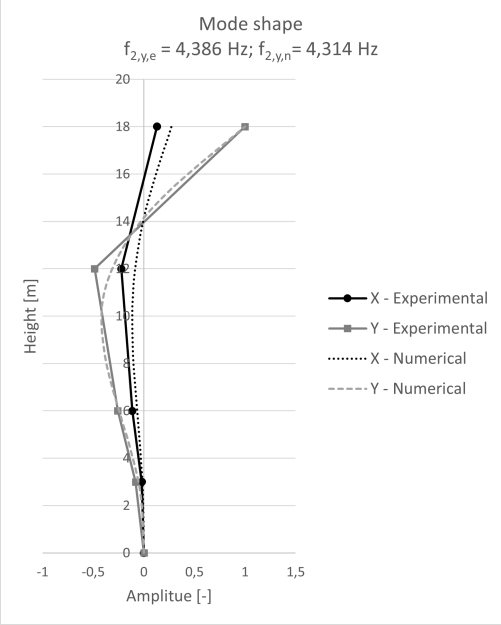

5.2.2 Model 2

Parameters

Like Model 1, the two parameters to define here are the Modules of elasticity and density. The retained values are displayed in table 5.5.

Table 5.5: Parameters used for Model 2.

$E\ [GPa]$	$\gamma\ [kN/m^3]$
$1,5$	19

Results

The results of the fitness functions for Model 2 are given in table 5.6.

Table 5.6: Fitness functions results of Model 2.

$H_f\ [-]$	$H_m\ [-]$
$0,02$	$0,59$

The natural frequencies of Model 2 are compared with the ones obtained from the experimental investigation in table 5.7.

Table 5.7: Numerical frequencies and their associated mode for Model 2.

	Experimental	Numerical	Associated mode
$f_{1,x}\ [Hz]$	$1,056$	$1,137$	ϕ_1
$f_{1,y}\ [Hz]$	$1,175$	$1,137$	ϕ_2
$f_{2,x}\ [Hz]$	$3,717$	$3,879$	ϕ_3
$f_{2,y}\ [Hz]$	$4,386$	$3,879$	ϕ_4

The modal assurance criterion between the experimental and numerical mode shapes of Model 2 can be found in table 5.8. The values in bold are the MAC values computed between 2 vectors associated with the same frequency. In this case, all values are greater than the threshold of $0,8$.

Table 5.8: MAC matrix of Model 2.

MAC	$\phi_{1,e}$	$\phi_{2,e}$	$\phi_{3,e}$	$\phi_{4,e}$
$\phi_{1,n}$	$\mathbf{0,982}$	$0,002$	$0,138$	$0,009$
$\phi_{2,n}$	$0,004$	$\mathbf{0,981}$	$0,012$	$0,373$
$\phi_{3,n}$	$0,346$	$0,010$	$\mathbf{0,857}$	$0,042$
$\phi_{4,n}$	$0,010$	$0,340$	$0,004$	$\mathbf{0,935}$

Mode shapes

Here are presented the first four modes of vibration of Model 2 (dashed lines) in comparison with the one obtained experimentally (plain lines).

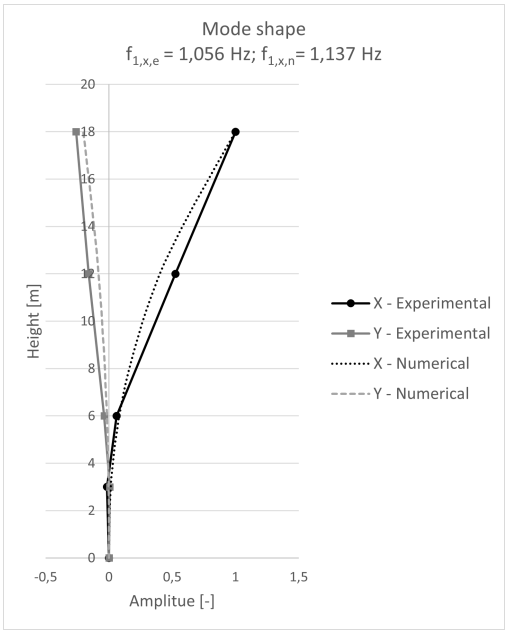

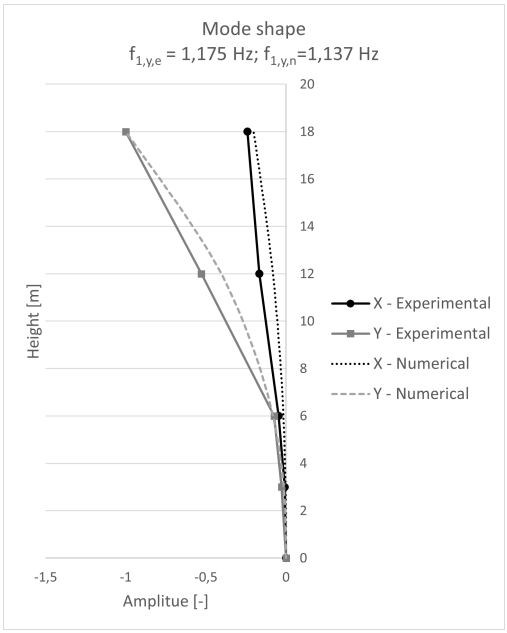

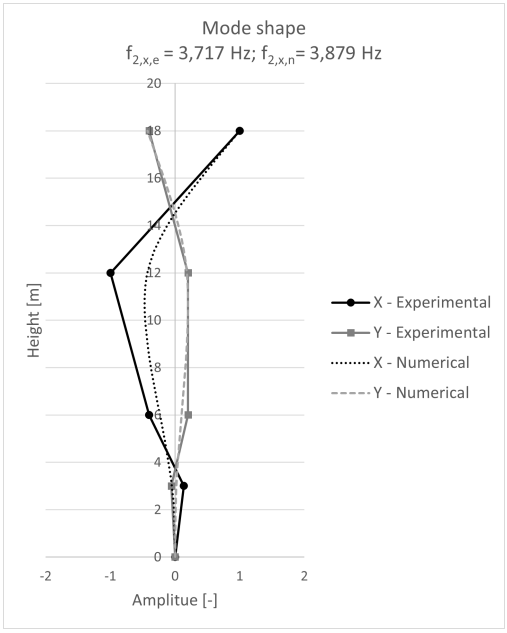

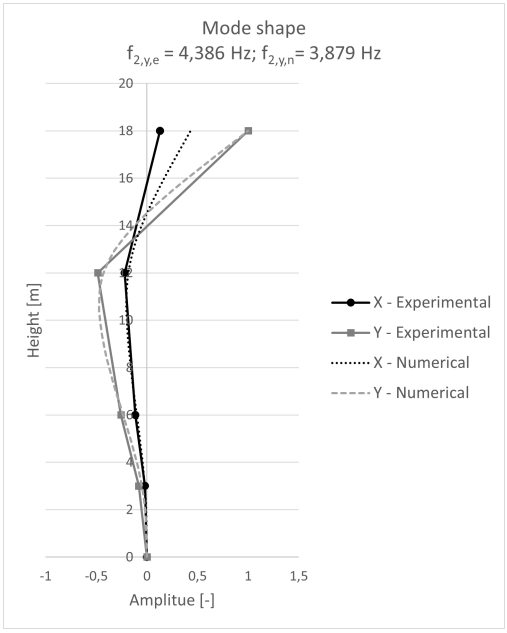

5.2.3 Model 3

Parameters

There are three parameters to define in Model 3, the Modules of elasticity E, the masonry density γ, and the soil's rotational stiffness K. The values retained for

each parameter are found in table 5.9.

Table 5.9: Parameters used for Model 3.

$E\ [GPa]$	$\gamma\ [kN/m^3]$	$K\ [kNm/rad]$
$2,5$	19	$400\,000$

Results

Table 5.10: Fitness functions results of Model 3.

$H_f\ [-]$	$H_m\ [-]$
$0,05$	$0,46$

Table 5.11: Numerical frequencies and their associated mode for Model 3.

	Experimental	Numerical	Associated mode
$f_{1,x}\ [Hz]$	$1,056$	$1,153$	ϕ_1
$f_{1,y}\ [Hz]$	$1,175$	$1,153$	ϕ_2
$f_{2,x}\ [Hz]$	$3,717$	$4,455$	ϕ_3
$f_{2,y}\ [Hz]$	$4,386$	$3,456$	ϕ_4

MAC matrix:

Table 5.12: MAC matrix of Model 3.

MAC	$\phi_{1,e}$	$\phi_{2,e}$	$\phi_{3,e}$	$\phi_{4,e}$
$\phi_{1,n}$	$\mathbf{0,990}$	$0,001$	$0,096$	$0,012$
$\phi_{2,n}$	$0,002$	$\mathbf{0,987}$	$0,009$	$0,266$
$\phi_{3,n}$	$0,507$	$0,003$	$\mathbf{0,699}$	$0,019$
$\phi_{4,n}$	$0,003$	$0,498$	$0,001$	$\mathbf{0,892}$

Mode shapes

In the different mode shapes displayed hereunder, the action of the non-rigid rotation can be observed when comparing the shapes near the base. The numerical modes (dashed lines) are not perfectly perpendicular to the ground plane.

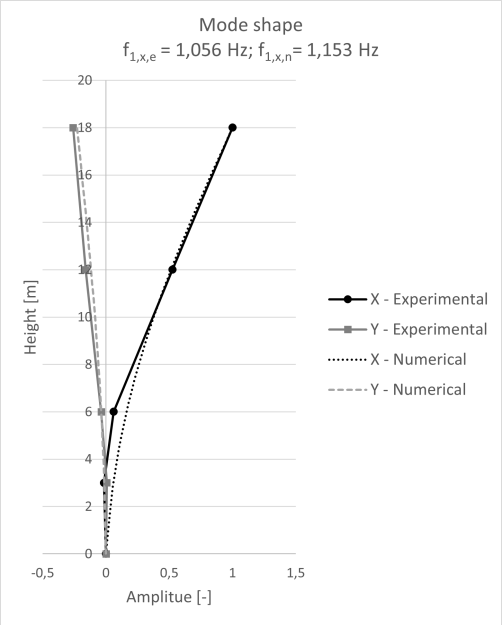

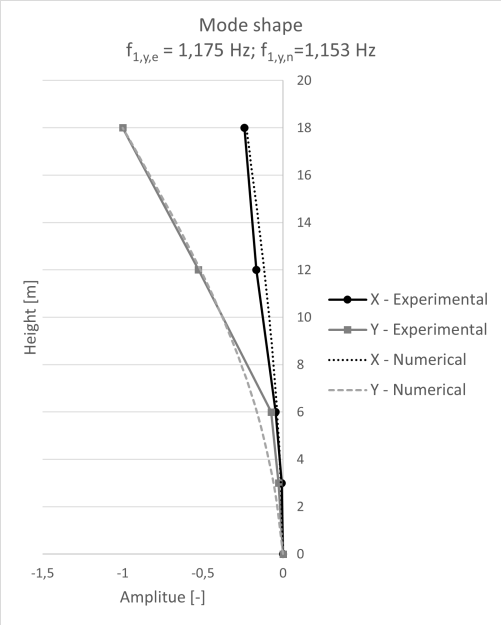

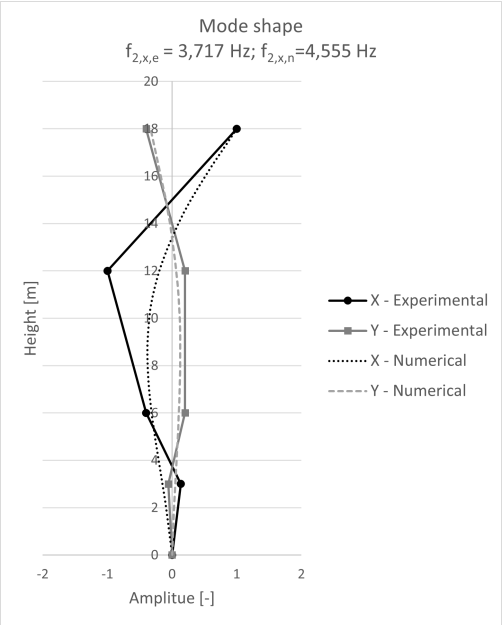

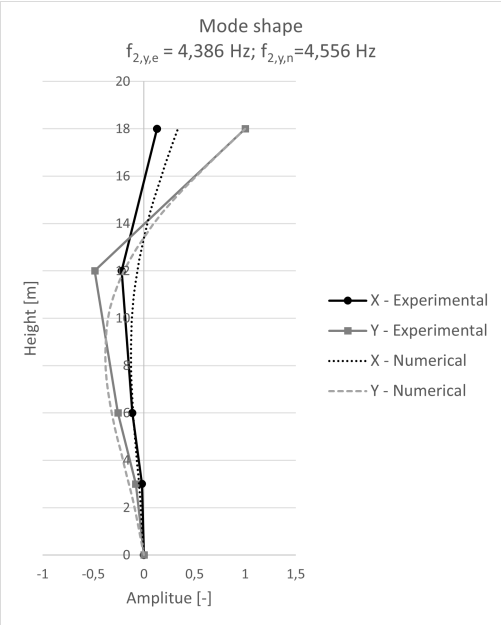

5.2.4 Model 4

Parameters

As in Model 3, three parameters are to be defined. The best model is given with the parameter values displayed in table 5.13.

Table 5.13: Parameters used for Model 4.

$E\ [GPa]$	$\gamma\ [kN/m^3]$	$K\ [kNm/rad]$
$2,5$	19	$400\,000$

Results

Table 5.14: Fitness functions results of Model 4.

$H_f\ [-]$	$H_m\ [-]$
$0,06$	$0,42$

Table 5.15: Numerical frequencies and their associated mode for Model 4.

	Experimental	Numerical	Associated mode
$f_{1,x}\ [Hz]$	$1,056$	$1,101$	ϕ_1
$f_{1,y}\ [Hz]$	$1,175$	$1,101$	ϕ_2
$f_{2,x}\ [Hz]$	$3,717$	$4,559$	ϕ_3
$f_{2,y}\ [Hz]$	$4,386$	$4,559$	ϕ_4

MAC matrix

Table 5.16: MAC matrix of Model 4.

MAC	$\phi_{1,e}$	$\phi_{2,e}$	$\phi_{3,e}$	$\phi_{4,e}$
$\phi_{1,n}$	$\mathbf{0,970}$	$0,019$	$0,086$	$0,003$
$\phi_{2,n}$	$0,022$	$\mathbf{0,972}$	$0,015$	$0,272$
$\phi_{3,n}$	$0,474$	$0,009$	$\mathbf{0,706}$	$0,037$
$\phi_{4,n}$	$0,010$	$0,466$	$0,000$	$\mathbf{0,873}$

Mode shapes

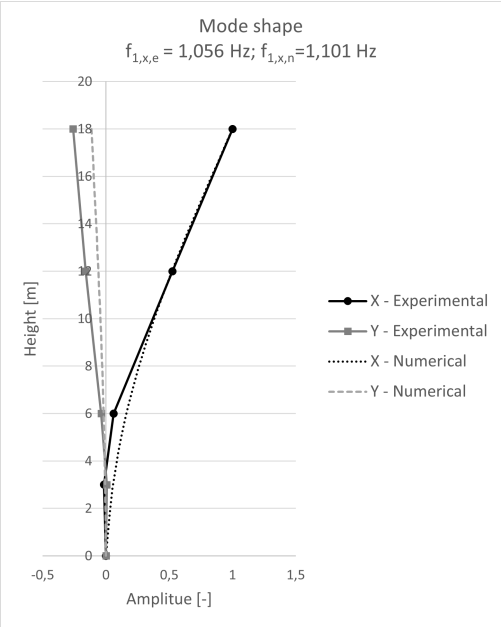
Mode shape
$f_{1,x,e}$ = 1,056 Hz; $f_{1,x,n}$=1,101 Hz
Height [m]
Amplitue [-]
X - Experimental
Y - Experimental
X - Numerical
Y - Numerical

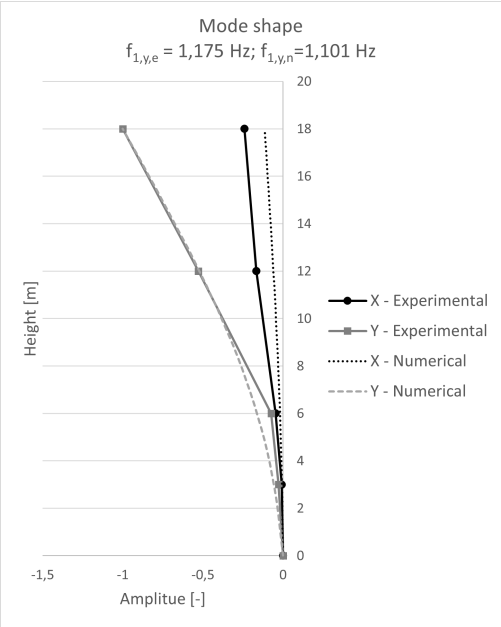
Mode shape
$f_{1,y,e}$ = 1,175 Hz; $f_{1,y,n}$=1,101 Hz
Height [m]
Amplitue [-]
X - Experimental
Y - Experimental
X - Numerical
Y - Numerical

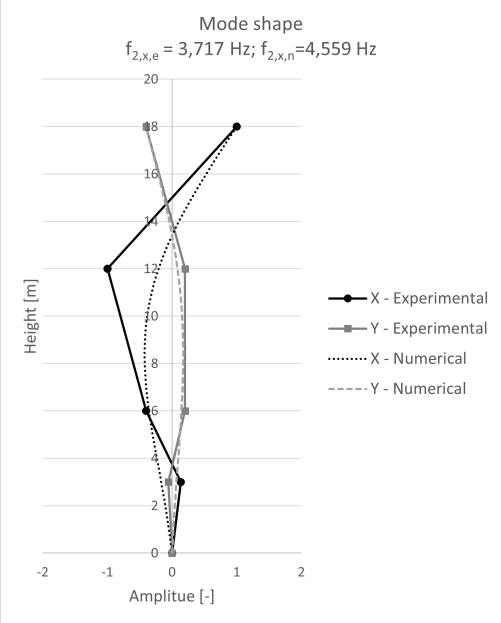
Mode shape
$f_{2,x,e}$ = 3,717 Hz; $f_{2,x,n}$=4,559 Hz
Height [m]
Amplitue [-]
X - Experimental
Y - Experimental
X - Numerical
Y - Numerical

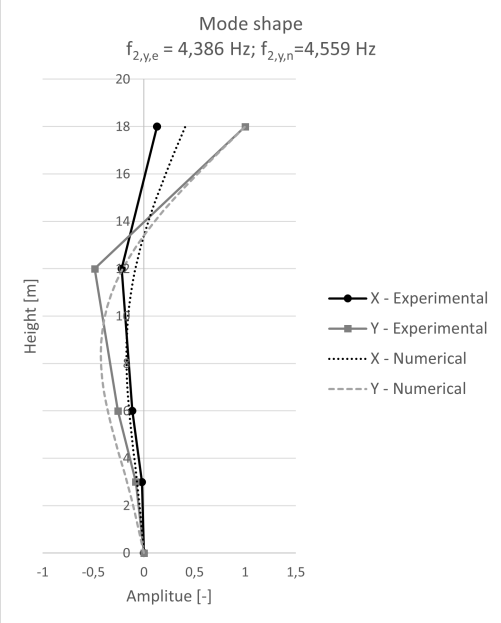
Mode shape
$f_{2,y,e}$ = 4,386 Hz; $f_{2,y,n}$=4,559 Hz
Height [m]
Amplitue [-]
X - Experimental
Y - Experimental
X - Numerical
Y - Numerical

5.3 Discussion of the results

Table 5.17 summarizes the parameters taken for each model as well as their fitness functions values. As Model 1 and 2 consider a perfectly embedded structure, it is equivalent to say that the rotational stiffness of the foundations are infinite.

Table 5.17: Comparative table of the calibration results.

	Model 1	Model 2	Model 3	Model 4
$E\ [GPa]$	$1,5$	$1,5$	$2,5$	$2,5$
$\gamma\ [kN/m^3]$	19	19	19	19
$K\ [kNm/rad]$	∞	∞	400 000	400 000
$H_f\ [-]$	$0,03$	$0,02$	$0,05$	$0,06$
$H_m\ [-]$	$0,56$	$0,59$	$0,46$	$0,42$

Model 1 and Model 2 show that a reduced modulus of elasticity increased the fit of the numerical data when comparing the results of their fitness functions with the ones of Model 3 and 4. However, as defined previously in chapter 4, the value of E should be at least greater than $2,5\ GPa$ to correspond to masonry in good shape, as it is the case with this structure. A value of $1,5\ GPa$ is typical for masonry with large visible cracks and even sometimes missing bricks.

Comparing Model 1 with Model 2 demonstrates that with a smaller cross-section near the top the model is closer to what was identified in situ. This shows that the structure gains flexibility on its upper part. Yet, a geometry like the one assumed in Model 2 is very unlikely when compared to building practices of that time. Drawings available of comparable chimneys in that area also discredit this hypothesis (Guedes et al. 2019).
Because of their lack of probability in their assumptions, Model 1 and 2 are rejected.

Chapter 2 explained that the natural frequency of a system is proportional to its rigidity (stiffness) and inversely proportional to its mass (density). Table 5.17 shows that all models maximize their flexibility reaching the lower elasticity and upper density limit.
Model 3 and 4 both assume a non-rigid foundation, giving some more flexibility to the model without changing its structural parameters. The value reached is a bending stiffness of 400 000 kNm/rad can corresponds to a *very stiff clay* or a *dense sand and gravel* (Melchers 1992). Both types of soil are found in the Porto area so this hypothesis can be accepted.
The calculations for the soil's properties are detailed in Appendix B.

Model 3 and Model 4 are really close to one another regarding their parametric values and fitness function results. It seems that the change in geometry between the two models does not affect greatly their dynamic properties. Table 5.18 displays the frequencies found with Model 3 and Model 4 compared to the ones found experimentally. For the first two frequencies, $f_{1,x}$ and $f_{1,y}$, associated with the first mode of vibration, Model 4 has smaller frequency values than Model 3. While for the ones associated with the second mode shape, it is the contrary. Model 3 has its modes closer to each other than Model 4.

Table 5.18: Comparison of computed frequencies in Model 3 and Model 4.

	Experimental	Model 3	Model 4
$f_{1,x}\ [Hz]$	$1,056$	$1,153$	$1,101$
$f_{1,y}\ [Hz]$	$1,175$	$1,153$	$1,101$
$f_{2,x}\ [Hz]$	$3,717$	$4,455$	$4,559$
$f_{2,y}\ [Hz]$	$4,386$	$4,456$	$4,559$

Both models are assessed in the next chapter to understand what the geometry assumptions change in the structural behavior when subjected to static and dynamic loads.

Chapter 6

Seismic assessment

This chapter is divided into four sections. The first one studies the behavior of Model 3 and Model 4 under gravity loading and agrees on the model to be dynamically assessed.
The first assessment of the structure is performed with the local conditions of Porto, then of Sagres. For both seismic assessments, a response spectrum and a dynamic time-history analysis are performed.
Finally, the chapter presents a comparison of the results obtained with a model in 2D shell finite element and the ones computed with a fiber element-based model.

6.1 Behavior under self-weight

Fiber elements

In SeismoStruct, two nodes are linked with one element, this element is subdivided into a number of integration sections, each of which is divided into several fibers. It is possible to choose to analyze any fiber and obtain its stress and strain.
In the models presented, each element is subdivided into five integration sections, and each section is itself subdivided in 152 fibers. The number of integration sections and fibers are taken according to the software recommendations.
For each element of the chimney's models, four fibers are analyzed in the integration section located in the middle of each element. All fibers are on the outer part of the section, in the four principal directions regarding the global axis: +X, -X, +Y, -Y, as indicated in red in figure 6.1a.

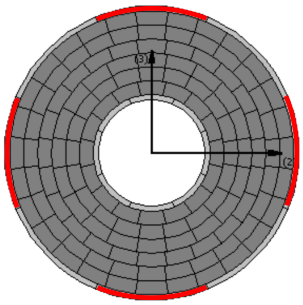

(a) Section of an element divided into several fibers.

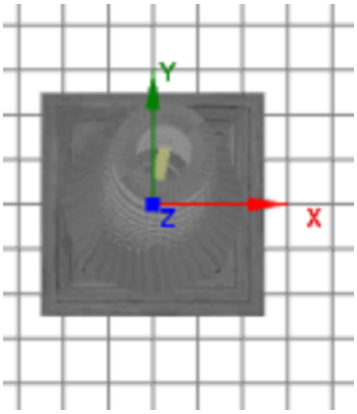

(b) Orientation of Model 4.

Figure 6.1: Top view cross section and Model 4.

Model 3 and Model 4 under self-weight

Figure 6.2 displays the results of the stress distribution along the height of both chimneys resulting from the self-weight loading. Each line corresponds to an element fiber. Negative stress corresponds to fiber in compression. As the analysis is elastic, the stress-strain relationship is described by

$$\sigma = \varepsilon \cdot E$$

The strain distribution follows the same path as the stresses and their values can be computed noted that $E = 2,5\ GPa$.

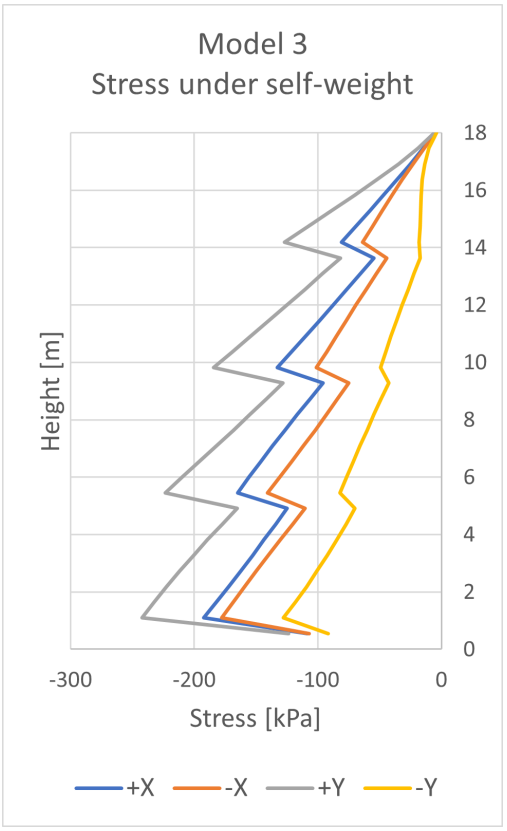

(a) Stress distribution for Model 3 under self-weight.

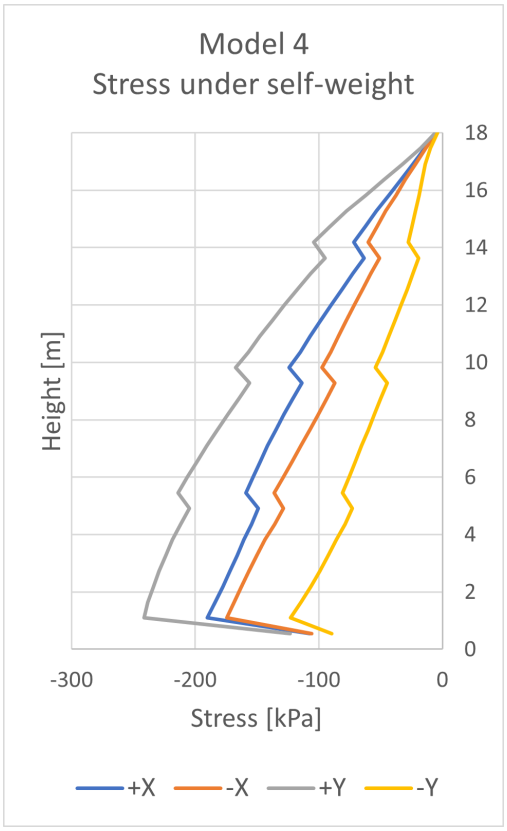

(b) Stress distribution for Model 4 under self-weight.

Figure 6.2: Stress distribution due to self-weight in all fibers.

For a symmetric structure, the stresses in the four directions would be expected to be equal. In this case, the chimney has an initial deformation bending towards the $+Y$ and $+X$ directions, as seen in figure 6.1b, therefore the fibers in those directions are expected to undergo higher compression stresses than the ones in the opposite direction. Figure 6.2 shows that it is the case, as the gray and blue lines have smaller values compared to the other two. Since the initial deformation is mainly towards the $+Y$ direction, those fibers undergo higher compression stresses. The jumps in figure 6.2 are located at four different heights, corresponding to the heights where the changes in sections are happening. The first one between 0 and 2 m is the biggest one because the change in the cross-section area between the base and the stack is significant. The three other jumps are occurring when the stack cross-section loses one brick in thickness.
The jumps on figure 6.2b are smaller compared to the one occurring in Model 3, indicating a smoother stress distribution. The expected distribution should be as

regular as possible since the chimney in Lusíada has a continuous tapered external stack. Model 4 is therefore preferred to Model 3 to pursue the investigation.

6.2 Assessment in Porto

6.2.1 Response spectrum analysis

The principles of response spectrum analysis are explained in Section 2.2.2. This section presents the spectra for the geographical zone of Porto and then the results from its application to the structure.

The design spectrum

To determine the spectrum to use, the Portuguese national Annex to Eurocode 8 gives information on the different parameter values regarding the geographical situation in the country. The detailed computation of the spectrum is available in Appendix C.
The design spectra for Porto are given in figure 6.15. Both curves for type 1 and type 2 seismic actions are displayed.

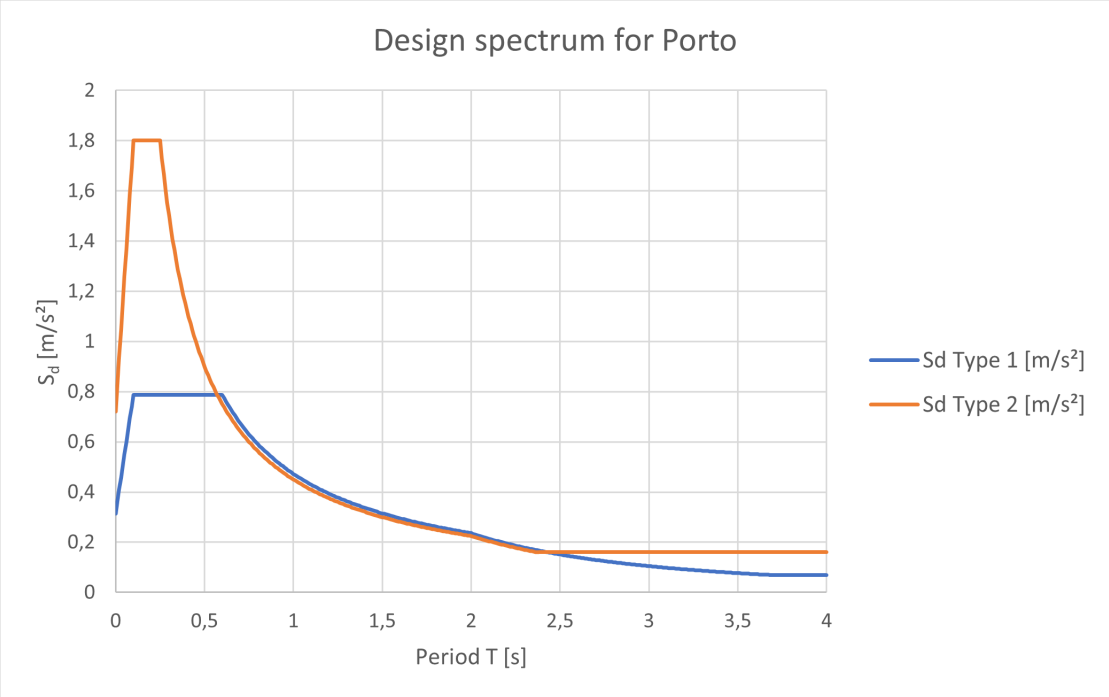

Figure 6.3: Design spectrum for Porto

The EC8 recommends assessing the structure with both types. However as the curve for the type 2 (in orange in figure 6.15) is the maximum value for almost all the periods, only this curve will be considered for the following analysis.

Following the recommendations of Eurocode 8, two combinations of seismic loads were studied:

$$E = 100\% \cdot E_X + 30\% \cdot E_Y$$
$$E = 30\% \cdot E_X + 100\% \cdot E_Y$$

Where E is the total excitation acting on the structure. E_X is the excitation following the X-axis and E_Y the Y-axis.
As the structure is not perfectly symmetric, the direction of the seismic loads influences the structural response. Therefore eight combinations were used:

$$E = \pm 100\% \cdot E_X \pm 30\% \cdot E_Y$$
$$E = \pm 100\% \cdot E_X \pm 30\% \cdot E_Y$$

Results from the analysis

This section presents the envelope of the highest stresses on the structure and the resulting displacements.
Figure 6.4 shows that the maximum stress in compression experienced by the structure is located at the base of the stack, so around $1,8\ m$ high. The masonry compression strength was defined in chapter 4 as $f_c = \frac{E}{700}$. After calibration, the model had a modulus of elasticity set to $2,5\ GPa$ which gives a compressive strength of

$$f_c = \frac{2\,500\,000\ [kPa]}{700} = 3571\ kPa$$

The maximum compressive stress value computed is much smaller than the masonry compression strength:

$$\sigma_c = 520\ kPa < 3571\ kPa$$

There is no risk of crushing bricks.

The maximum tensile stress allowed for masonry for the response spectrum analysis is $0\ kPa$, because the analysis supposes an elastic material. Figure 6.4 shows that the maximum tensile stress is located around $10m$ high in the fiber in the $-Y$ direction and is larger than $0\ kPa$.

$$\sigma_t = 193\ kPa >> 0\ kPa$$

This observation leads to the conclusion that, following the assumptions, the structure does not sustain the earthquake. Note that the higher stresses are along the $Y - axis$, which is the same direction as the largest initial deformation of the chimney.

Regarding the strain distribution, as the analysis is elastic, the strains follow the rule:

$$\varepsilon = \frac{\sigma}{E}$$

For the maximum tensile stress, the corresponding elongation is

$$\varsigma_{max} = \frac{193\ kPa}{2\,500\,000\ kPa} = 7,72 \cdot 10^{-5}\ m/m$$

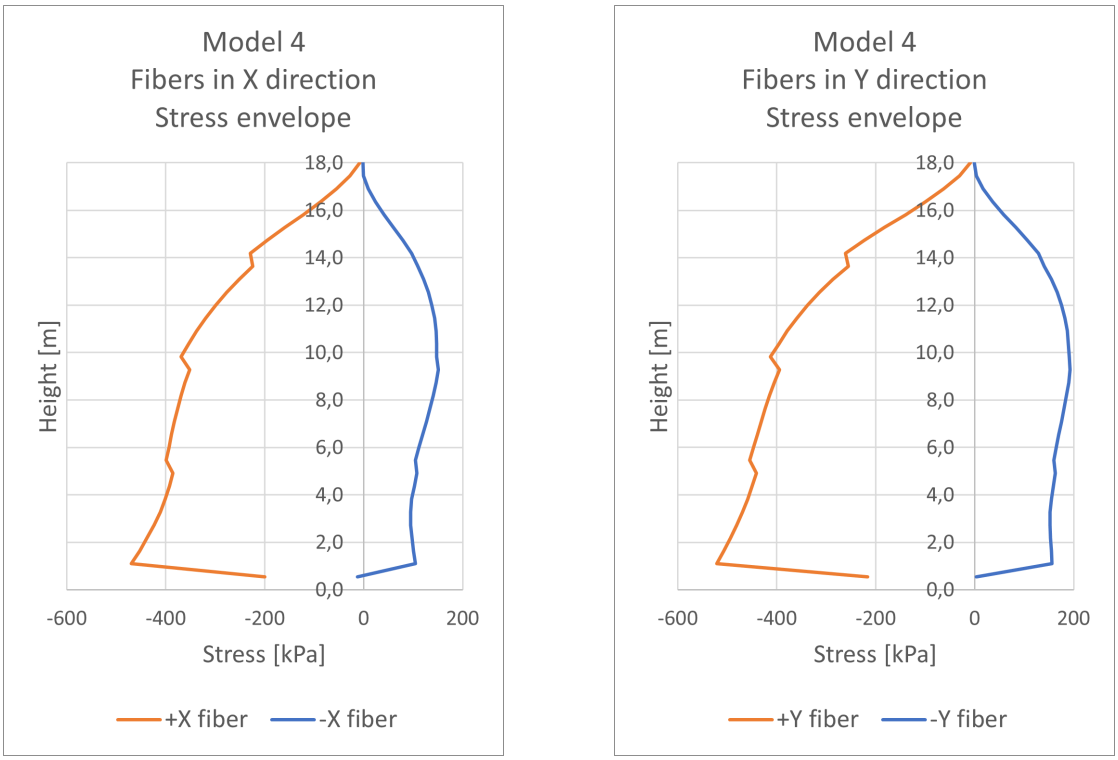

(a) Stress distribution in the X direction.

(b) Stress distribution in the Y direction.

Figure 6.4: Envelope of stress distribution from the RSA of Model 4 in Porto.

Figure 6.5 presents the relative displacements computed with the response spectrum method. The structural displacements take a shape close to the first and second mode shapes derived previously. Figure 6.6 recall those mode shapes.

It is noticed that the maximum curvature of the relative displacements occurs at a height of about 10 m, which is the same height at which the maximum tensile stress occurs (blue lines in figure 6.4).
From the combination $\pm 100\% \cdot E_X \pm 30\% \cdot E_Y$, the maximal relative displacement occurring at the top node has an amplitude of $d_{top} = \sqrt{0,031^2 + 0,020^2} = 0,037\ m$. The amplitude from the combination $\pm 30\% \cdot E_X \pm 100\% \cdot E_Y$ is $d_{top} = \sqrt{0,013^2 + 0,037^2} = 0,040\ m$.
According to the response spectrum analysis, the structure has a maximal relative displacement at the top of 4 cm.

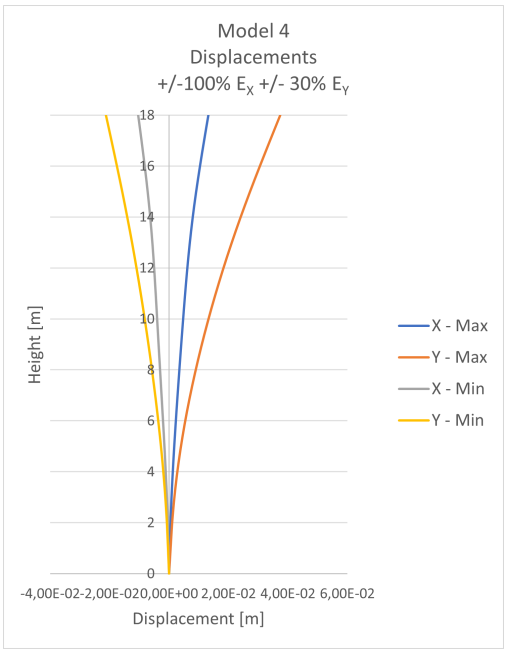

(a) Relative displacement from the combination $\pm 100\% \cdot E_X \pm 30\% \cdot E_Y$.

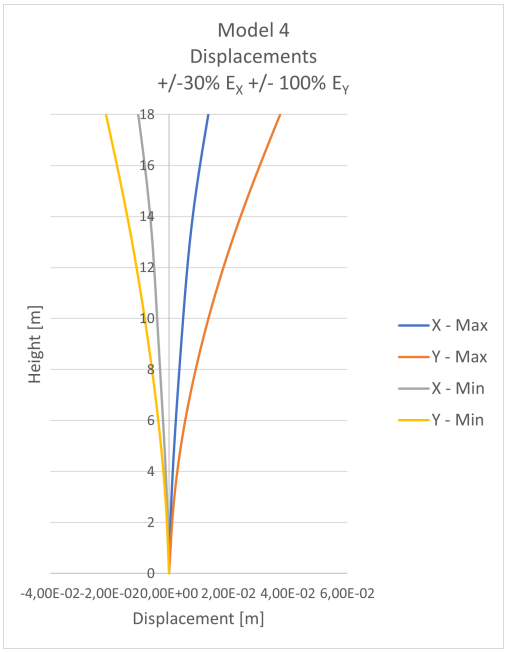

(b) Relative displacement from the combination $\pm 30\% \cdot E_X \pm 100\% \cdot E_Y$.

Figure 6.5: Relative displacement from the RSA of Model 4 in Porto.

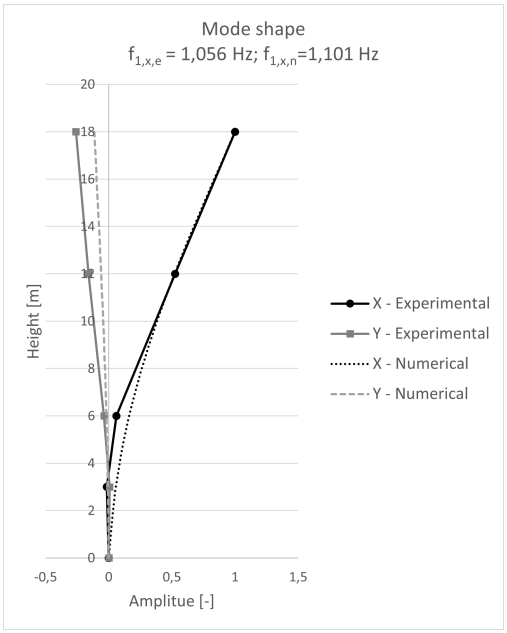

(a) First mode shape of Model 4.

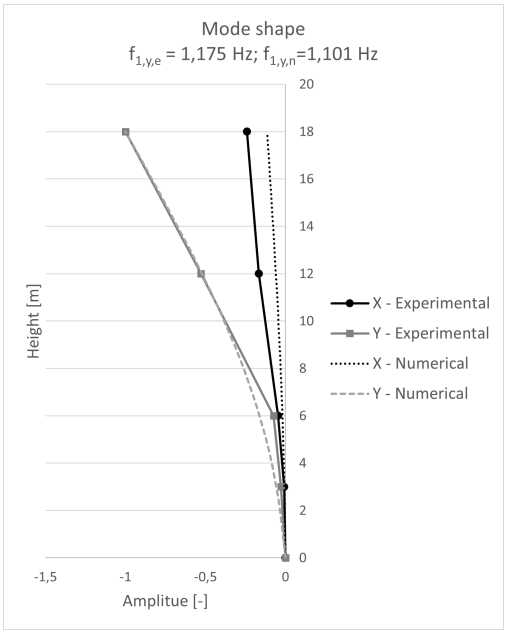

(b) Second mode shape of Model 4.

Figure 6.6: First and second mode shapes of Model 4.

6.2.2 Dynamic time-history analysis

Ground accelerations

To perform dynamic time-history analysis, a set of ground accelerations is needed. A total of eight artificial ground motions are used in the following analysis. As they are artificial, they are all compatible with the elastic spectra computed with the Eurocode 8 procedure. A scale factor is applied to them in order to reach the peak ground acceleration demand of Porto. All the ground motions correspond to a ground motion of type 2.
Figure 6.7 compares the elastic spectra derived from each of those ground motions with the elastic spectra of type 2 defined using Eurocode 8 for the area of Porto.

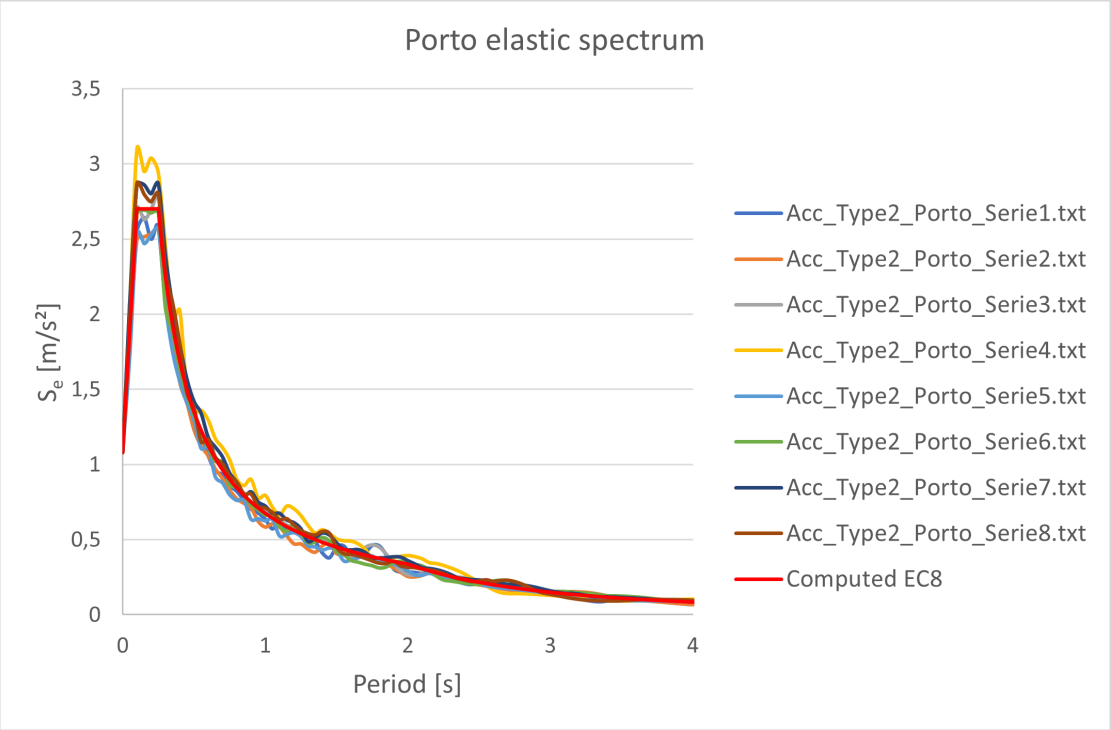

Figure 6.7: Elastic spectra of Porto.

Figure 6.8 displays one of the accelerographs. The ground motion lasts 15 seconds and then a series of zeros are added at the end in order to let the structure oscillates during the analysis. This trick also permits to discern of any residual displacements due to material nonlinearities.
All the ground motions used for the analysis of Model 4 in Porto can be found in Appendix D.

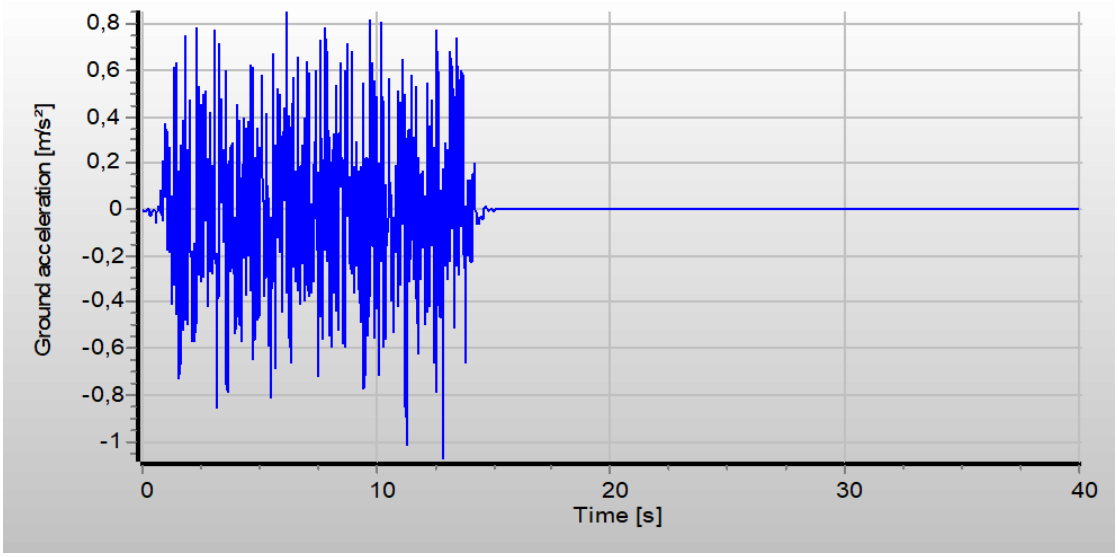

Figure 6.8: Ground acceleration for the analysis in Porto.

In the following analysis, all eight ground motions were run with the model, following the loading combinations $30\%E_X + 100\%E_Y$. Only the results of the series giving the largest top node displacements are detailed.

Analysis parameters

For the dynamic time-history analysis, the compression strength for the masonry is set to 40 $[kPa]$. A low value but different from zero is used as it can help for numerical convergence.

To model energy dissipation and motion decay, a Rayleigh damping is assigned to the structure, using two different frequencies associated to two different mode shapes. The frequencies $f_{1,x} = 1,101\ Hz$ and $f_{2,x} = 4,559$ are used with both a low damping ratio of $1,5\%$.

Results

The Serie 7 from the ground accelerations set gives the largest displacement of the top node. Figure 6.19 displays the displacements of the ground node (centered at the base of the chimney) and top node. The values displayed are displacements relative to the initial node coordinates. In figure 6.19, the initial top node displacements close to $0,005$ at $t = 0\ s$ are due to the application of gravity over the system. At that time, the ground has not yet started to move. The maximum displacement

computed in the Y-direction is $d_y = 0,084\ m$ happening at $t = 13,815\ s$ in the Y-direction. At this moment the displacement in X is equal to $d_x = 0,022\ m$.
Ten peaks can be counted between 20 and 30 s giving an oscillation period close to 1 Hz, resulting in a frequency of 1 Hz. This frequency is very close to the first frequencies of the model $f_{1,x} = f_{1,y} = 1,101\ Hz$.
Both graphs show that the oscillations converge towards the displacement value at $t = 0\ s$, meaning that there is no permanent deformation after the seismic action.

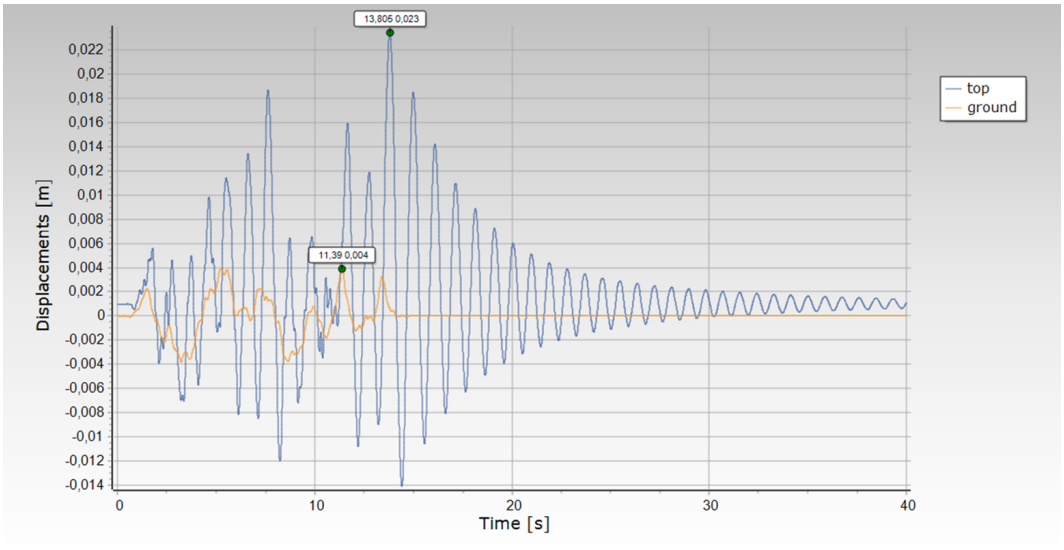

(a) Displacements in X-direction.

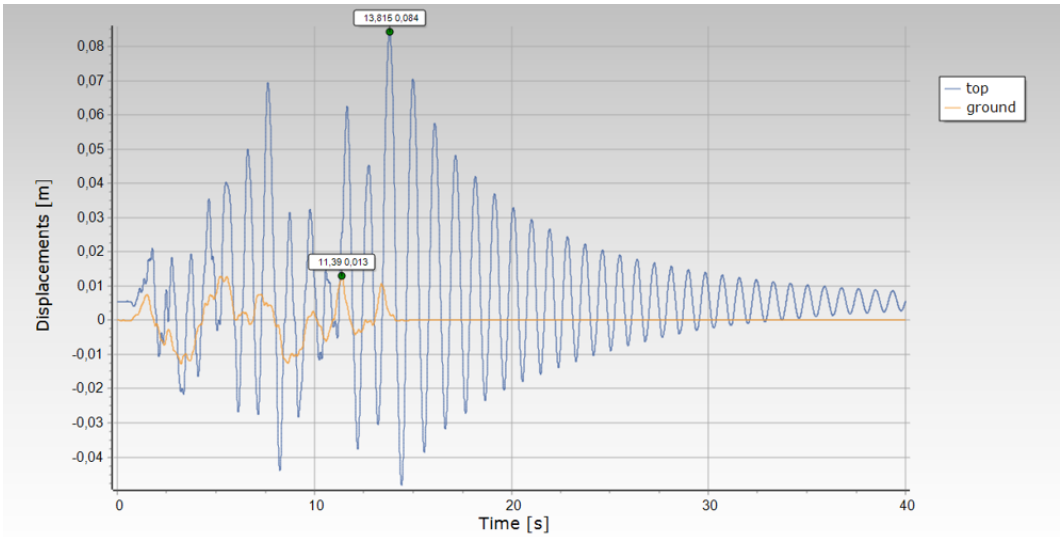

(b) Displacements in Y-direction.

Figure 6.9: Ground (in orange) and top node (in blue) displacements relative to initial node coordinates. Assessment in Porto.

Figure 6.10 displays the displacement of each node relative to their initial position at the time $t = 13,815\ s$, where the top node displacement is maximal in the $+Y$-direction.
The total displacement amplitude of the top node is computed as $d_{top} = \sqrt{0,023^2 + 0,084^2} = 0,087\ m$.

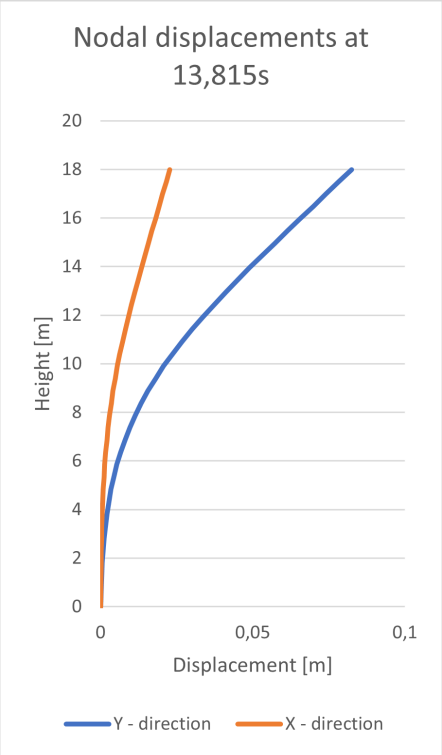

Figure 6.10: Nodal displacements at $t = 13,815\ s$. Assessment in Porto.

Figure 6.11 displays the hysteretic curve of the base shear in $[kN]$ over the Y-direction top node displacements in $[m]$. Some loops are centered around the displacement of $d_{top} = 0\ m$, this behavior is typical of elastic structural response. When the pattern becomes less symmetric, the structure fibers enter plasticity. The maximum top node displacement of $d_{top} > 0,08\ m$ occurs when the base shear has a low value close to 0. On the other hand, the maximum base shear computed reaches a value of $55\ kN$ when the top node is close to its initial position ($d_{top} \approx 0\ m$).

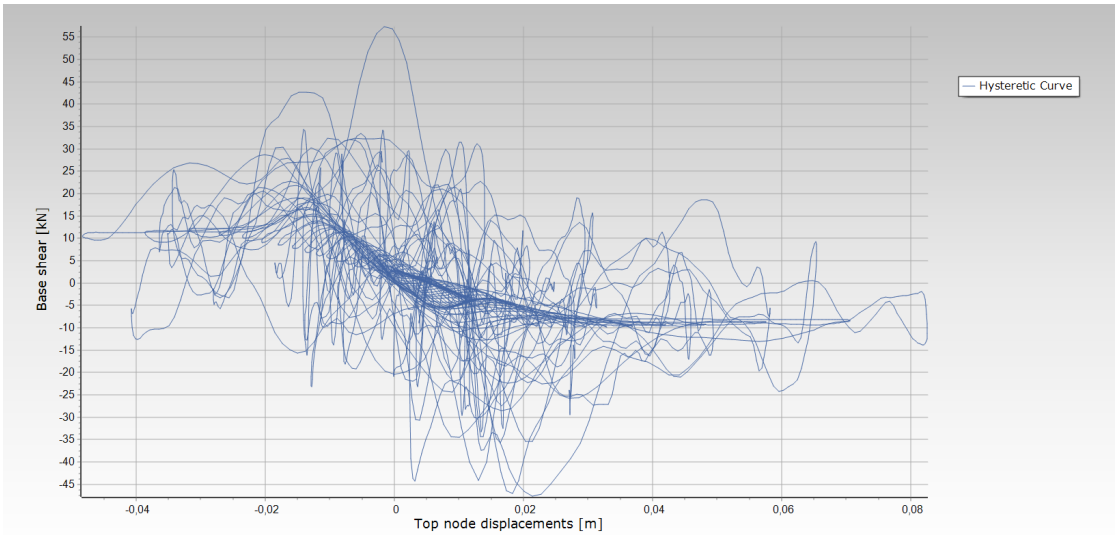

Figure 6.11: Hysteretic curve of the base shear in $[kN]$ over the top node displacement in the Y-axis $[m]$.

As the largest displacement occurs in the Y-axis, the maximum stresses and strains are expected to be along the fibers in the $+Y$ and $-Y$ directions respectively. Figure 6.12 displays the stress in all fibers in the $+Y$-direction over time. It allows to discern that the maximum compression stress occurs at $t = 13,75\ s$, almost the same time as the maximum displacement of the top node, with a value of $\sigma_c = -890\ kPa$. While the maximum tensile stress reaches the tensile strength of $40\ kPa$ multiple times before $t = 15\ s$. After $t = 15\ s$, the time period between two peaks approximates $T = 0,91\ s$, the equivalent frequency is $f = 1,1\ Hz$. This frequency is almost similar to the frequencies of the first modes of vibration $f_{1,x} = f_{1,y} = 1,101\ Hz$.
The strains over time for the fibers in the $-Y$-direction is displayed in figure 6.13. The maximum strain reaches a value of $\varepsilon_{max} = 0,00098\ m/m$ at the time $t = 11,7\ s$. Meaning that a brick of $20\ cm$ high is elongated of

$$\Delta_{brick} = \varepsilon_{max} \cdot 0,2\ m = 0,00019\ m = 0,19\ mm$$

The maximum elongation of one brick is $0,19\ mm$.

Figure 6.14a displays the stress distribution of the $+Y$ fibers at $t = 13,75\ s$, where the maximum compression stress occurs. The maximum compression stress occurs at a height of about $7\ m$ and its value $\sigma_c = 890\ kPa$ is smaller than the compression strength of $3571\ kPa$.
Figure 6.14b displays the strain distribution of the $-Y$ fibers at $t = 11,7\ s$.
The maximum strain occurs at $11\ m$ high and has a positive value of $9,8 \cdot 10^{-4}\ m/m$.

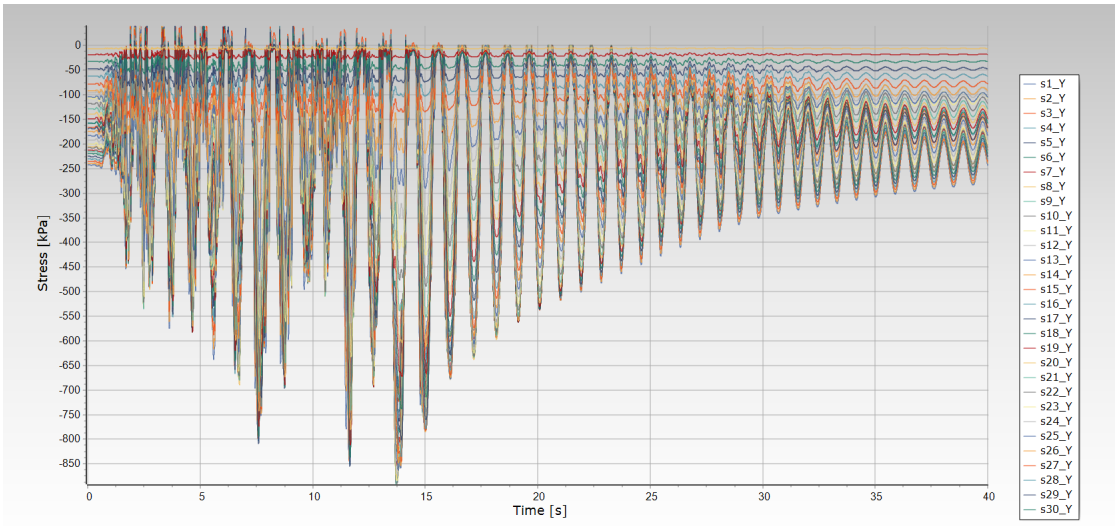

Figure 6.12: Stresses $[kPa]$ over time $[s]$ for the fibers in the $+Y$-direction. The maximum value is $\sigma_t = 40\ kPa$ and the minimum value is $_c = -890\ kPa$. Assessment in Porto.

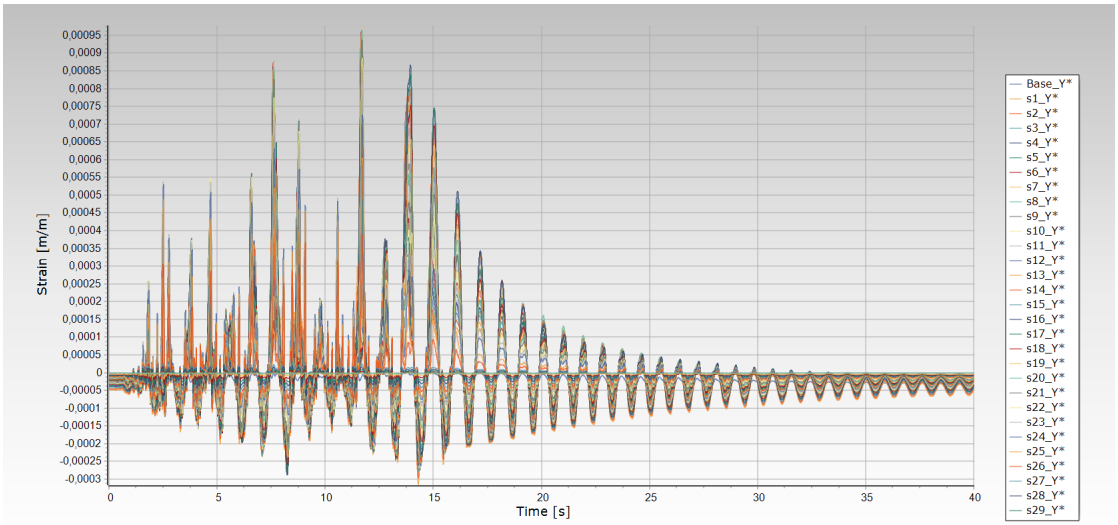

Figure 6.13: Strains $[m/m]$ over time $[s]$ for the fibers in the $-Y$-direction. The maximum value is $\varepsilon_t = 0,00098\ m/m$ and the minimum value is $\varepsilon_c = -0,00032\ m/m$. Assessment in Porto.

The fiber is in tension and the structure still resists the ground motion, which means that the fiber entered the plasticity threshold.

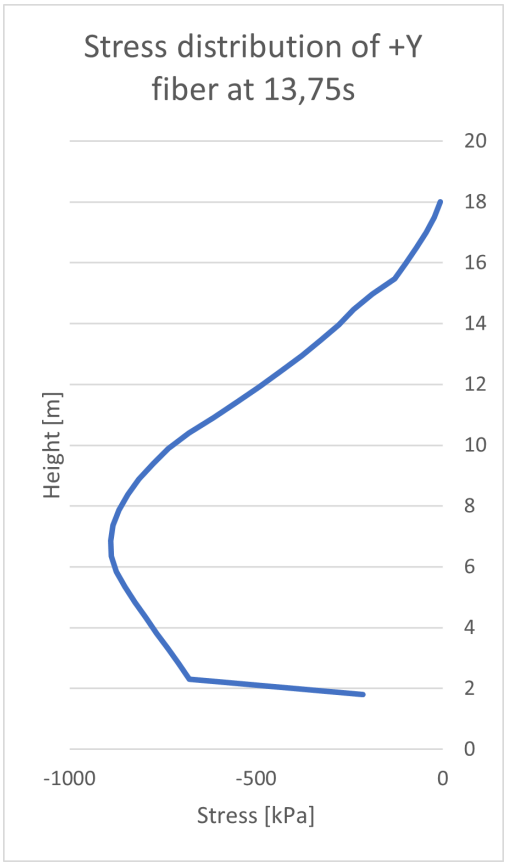

(a) Stress distribution in $+Y$-direction fibers.

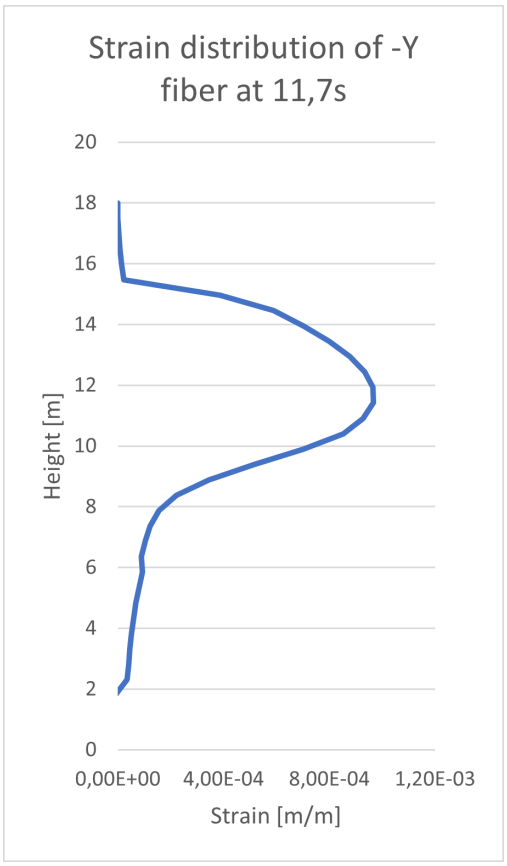

(b) Strain distribution in $-Y$-direction fibers.

Figure 6.14: Stress and strain distribution along the height for the assessment in Porto.

6.2.3 Conclusion

Table 6.1 displays the different values of interest computed by the response spectrum analysis (RSA) and the dynamic time-history analysis (DTHA).
The maximum displacement amplitude of the top node calculated by the DTHA is more than twice the value calculated by the RSA. The maximum compression stress and tensile strain values are also superior in the time-history analysis rather than the RSA.
Both maximum compression stresses computed are below the masonry compression

Table 6.1: Summary of the values computed by the response spectrum analysis (RSA) and the dynamic time-history analysis (DTHA) for the chimney in Lusíada with the seismic conditions of Porto.

	RSA	DTHA
Maximum top node displacement	$4,0\ cm$	$8,7\ cm$
Maximum compression stress	$520\ kPa$	$890\ kPa$
Location of the maximum stress	$1,8\ m$	$7\ m$
Maximum tensile strain	$7,7 \cdot 10^{-5}\ m/m$	$9,8 \cdot 10^{-4}\ m/m$
Location of the maximum strain	$10\ m$	$11\ m$

strength of 3571 kPa. There is then no risk of crushing. However, both values do not happen at the same location. For the RSA, the stress occurs at the bottom of the stack, while for the DTHA the maximum compression happens a little bit below the middle of the stack's height.

The response spectrum method assumes that the masonry behaves elastically and that no tension is permitted. Therefore since the computed tensile strain is superior to zero, the conclusion is the chimney will not sustain the earthquake because some parts of it experience tension. Reinforcements may be recommended to improve the strength properties of the chimney.
The DTHA on the other hand, assuming less conservation hypothesis shows that the structure can sustain the entire ground motion. Its computed responses are superior to the ones obtained with the response spectrum analysis. Yet the assumption of inelastic material allows the structure to sustain the earthquake without additional reinforcements.

6.3 Assessment in Sagres

The previous analysis showed that the structure can sustain an earthquake in its location: Porto. The following section is developed to answer the question: would this chimney sustain the strongest earthquake possible in Portugal?
It turns out that the region suffering the most devastating earthquake in Portugal is located at its southern cape. This region is near the city called Sagres.

6.3.1 Response spectrum analysis

The design spectrum

For Sagres, the design spectrum is computed following the same process as in Section 6.2.1, the only difference comes in the value of the PGA. For a seism of type 1, $a_{gR} = 2,5\ [m/s^2]$ and for type 2, $a_{gR} = 1,7\ [m/s^2]$.
The design spectrum for Sagres is given in figure 6.15. Both curves for type 1 and type 2 seismic actions are displayed. As the curve for the type 1 is the envelope for all the periods, only this one will be considered for the following analysis.

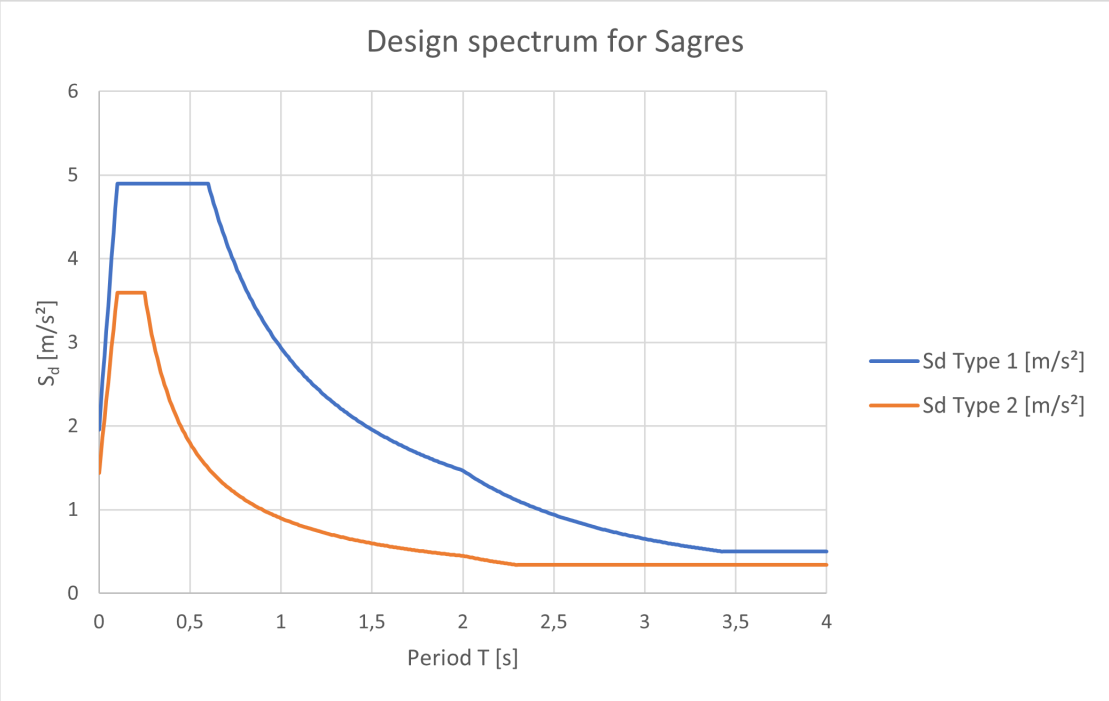

Figure 6.15: Design spectrum for Porto

Results from the analysis

Figure 6.16 displays the envelope of the stresses computed for the fibers in all four directions.
The maximum compression stress is attained in the $+Y$ fiber from the combination $\pm 30\% E_X \pm 100\% E_Y$. Its value is $\sigma_c = -2828\ kPa$.
From the same loading combination, the maximum tensile stress occurs in the $-Y$ fiber with a value of $\sigma_t = 2462\ kPa$. This value is much higher than the assumed compression strength of zero. In terms of elongation, the maximum strain is equal

to

$$\varepsilon_{max} = \frac{\sigma_t}{E} = \frac{2462\ kPa}{2\,500\,000\ kPa} = 9,85 \cdot 10^{-5}\ m/m$$

For a brick of 20 cm height this is equivalent to a deformation of $0,19\ mm$.

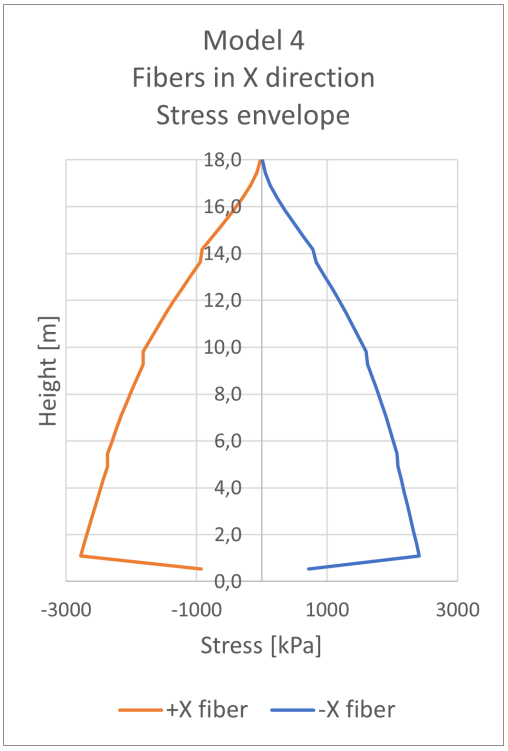

(a) Stress distribution in the X direction.

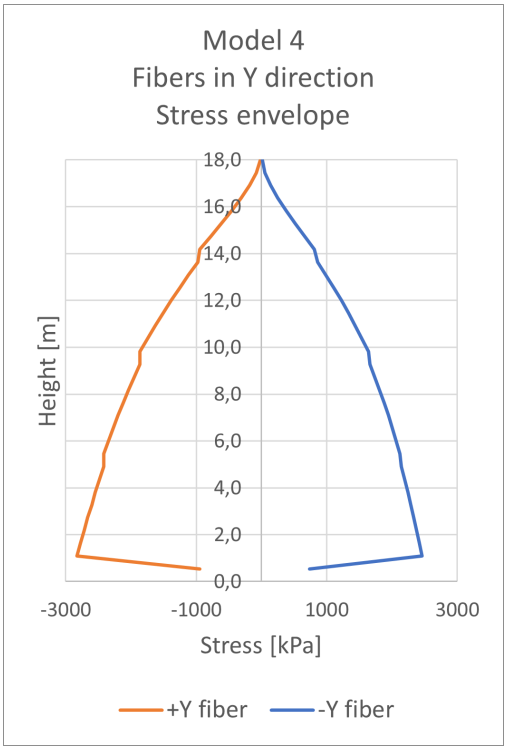

(b) Stress distribution in the Y direction.

Figure 6.16: Envelope of stress distribution from the RSA of Model 4 in Sagres.

Figure 6.17 displays the maximum displacement computed with the response spectrum method on Model 4 with the spectrum of Sagres.
The maximum amplitude for the top node is a displacement of $d_{top} = \sqrt{0,11^2 + 0,29^2} = 0,31\ m$.

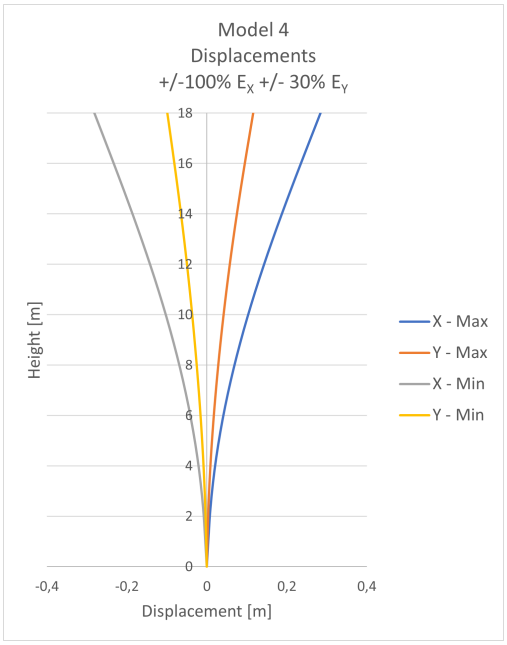

(a) Relative displacement from the combination $\pm 100\% \cdot E_X \pm 30\% \cdot E_Y$.

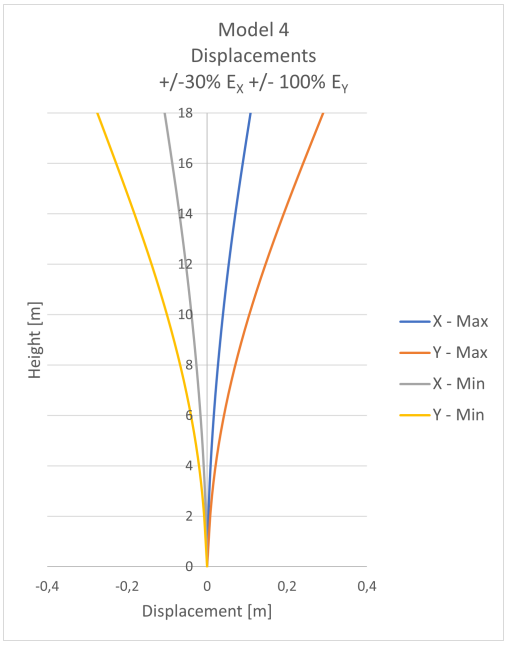

(b) Relative displacement from the combination $\pm 30\% \cdot E_X \pm 100\% \cdot E_Y$.

Figure 6.17: Relative displacement from the RSA of Model 4 in Sagres.

6.3.2 Dynamic time-history analysis

Ground accelerations

A set of eight ground accelerations is used. For it is a type 2 seism that is used, each ground motion lasts for 40 seconds. Then a series of zeros of 25 seconds is added at the end, making the total recording 65 seconds long.
All the time-domain ground accelerations used for this analysis are displayed in Appendix E.
In figure 6.18 the elastic spectra of each ground motion are compared with the one given by the Eurocode procedure.

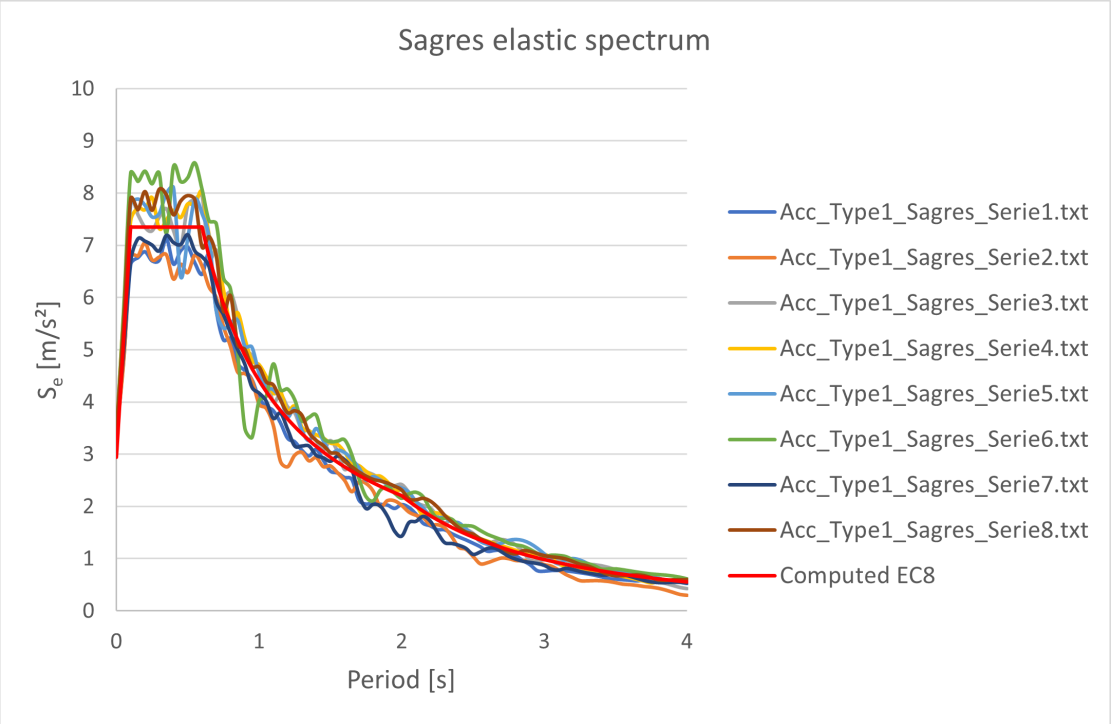

Figure 6.18: Elastic spectra of Sagres.

Results from the analysis

With the initial Rayleigh damping of $1,5\%$ assigned to the structure, the computations only converge for Series 7 and 8. The material model still has a tensile strength of 40 kPa.
A damping of 2% is assigned to the structure to resolve the problem. Now three series converge, number 4, 6, and 7. Trying to make all the Series converge, a reduction factor is applied to each of them individually. Series 1 and 2 need a reduction factor of $0,8$, while Series 3, 5, and 8 require a reduction factor of $0,7$.

The results presented come from the model with a damping ratio of $1,5\%$ defined for the frequencies $f_{1,x}$ and $f_{2,x}$. The excitation is the ground accelerations Series 8 applied with the combination: $30\%E_X + 100\%E_Y$. This choice is made to be able to compare the results with the previous analysis, section 6.2.2. And Series 8 is chosen over Series 7 because it is the one producing the largest top node displacements.

Figure 6.19 presents the displacements of the ground and top nodes over time. The displacements of the nodes are relative to their initial coordinates. Figure 6.19a

displays the displacement in the X-axis and figure 6.19b in the Y-axis. The top node has a maximal displacement of $0,44\ m$ in the $+Y$-direction and a displacement of $0,09\ m$ in the $+X$-direction. They both occur at the same time $t = 36,67\ s$, so the total displacement amplitude is $d_{top} = \sqrt{0,44^2 + 0,09^2} = 0,45\ m$.
As detailed previously the ground motion stops after 40 seconds, after that the structure oscillates towards its equilibrium position. The oscillation frequency is close to 1 Hz. It is possible to see in both graphs in figure 6.19 that the displacement of the top node starts near the zero displacement value but tend to a negative value at the end of the analysis. This observation proves a residual displacement due to the entry in plasticity of the constitutive material.
Following the ground curve, in orange, the same behavior is observed.

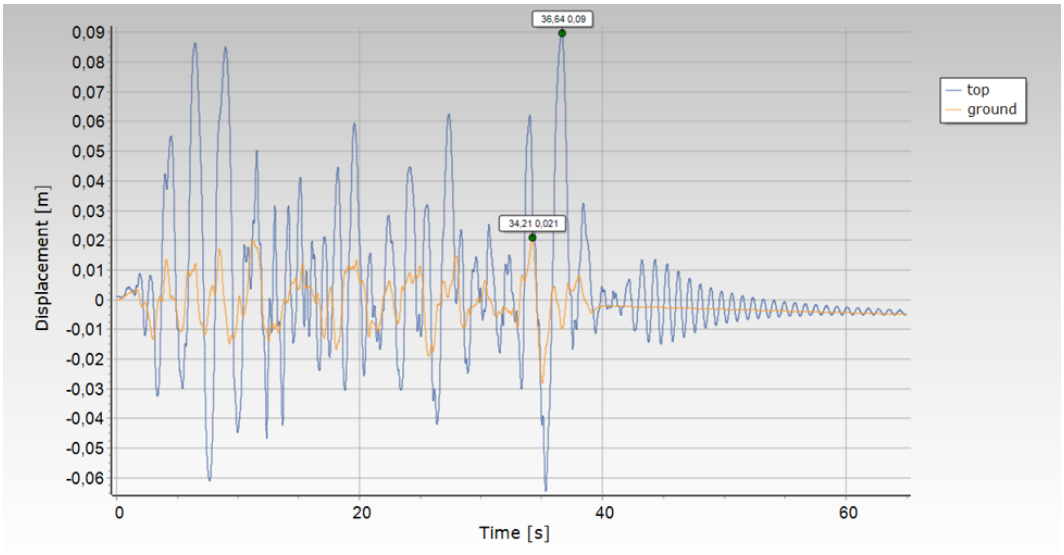

(a) Displacements in X-direction.

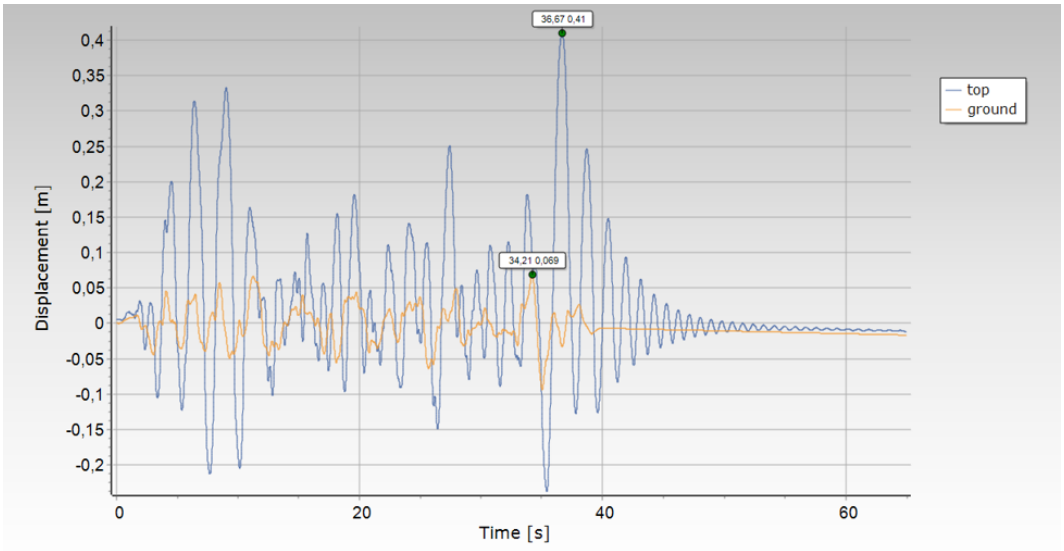

(b) Displacements in Y-direction.

Figure 6.19: Ground (in orange) and top node (in blue) displacements relative to initial node coordinates. Assessment in Sagres.

Figure 6.20 shows the nodal displacements distribution at the time $t = 36,67\ s$, where the top node displacement is maximal. The deformed structure takes a shape close to its first vibration mode.

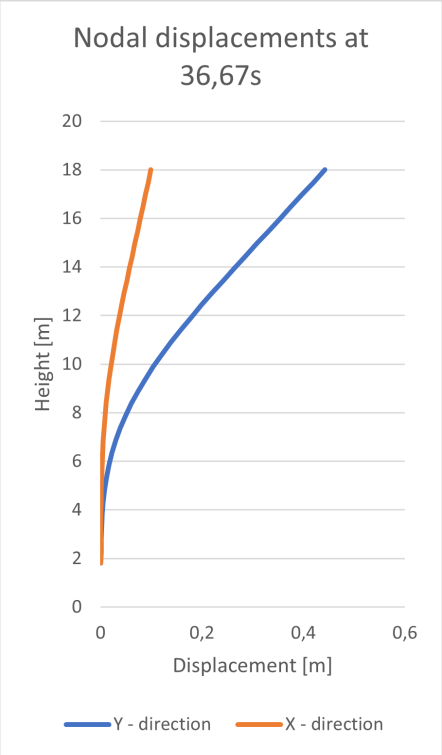

Figure 6.20: Nodal relative displacements at $t = 36,67\ s$. Assessment in Sagres.

Figure 6.21 puts on view the hysteretic curve of the base shear versus the displacement of the top node in the Y-axis. The maximum amplitude of the shear at the base reaches a value close to 100 kN when the displacement of the upper node is close to its initial position. In contrast, the top node displacement is maximum when the base shear is almost null.
The graph has a tendency to extend horizontally, indicating that the base shear value is mostly in the range $[-60; 60]$ kN.

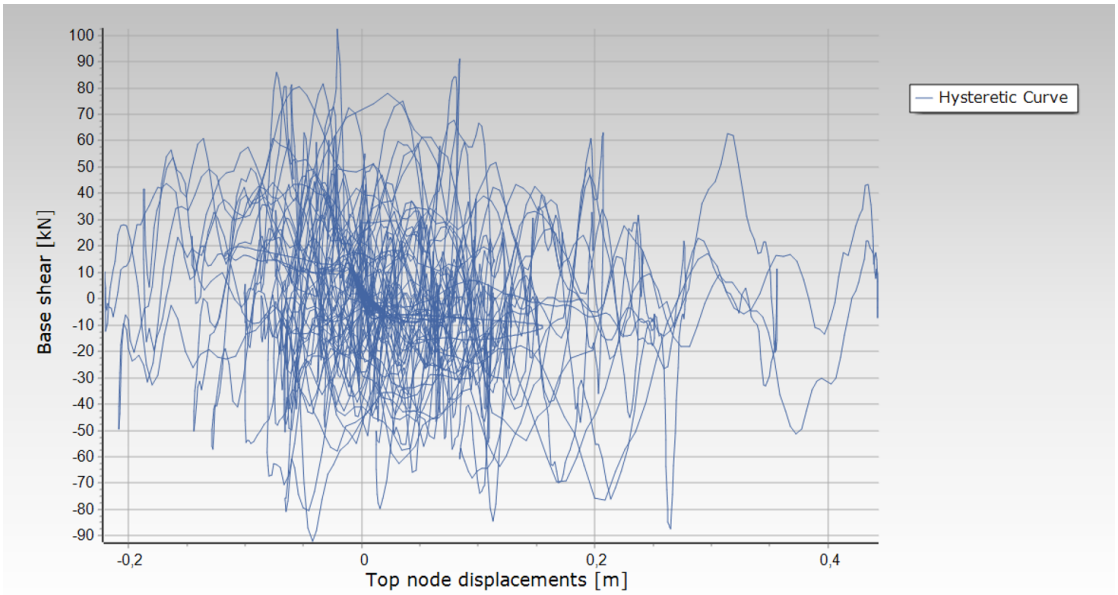

Figure 6.21: Hysteretic curve of the base shear in $[kN]$ over the top node displacement in the Y-axis $[m]$. Assessment in Sagres.

The maximum displacement value is in the $+Y$-direction. Based on figure 6.20, the maximum compression stress is expected to be in the $+Y$ fibers, while the maximum strain should be located in the $-Y$ fibers.
The graph in figure 6.22 plots the stress values of all the fibers in the $+Y$-direction. The tensile strength $f_t = 40\ kPa$ is reached multiple times in the fibers during the analysis. The maximum compression stress is reached at $t = 8,7\ s$, its value is $\sigma_c = -2921\ kPa$. It is smaller the the compression strength of $f_c = 3571\ kPa$.
The graph in figure 6.23 displays the different strains undergone by the fibers in the $-Y$-direction the maximum value reached is $0,0075\ m/m$. For a brick of $20\ cm$, this correspond to an elongation of $1,5\ mm$.

Figure 6.24 presents both stresses and strains distributions at the time of their respective maximum.
The stress distribution in figure 6.24a indicates that the majority of compression stresses are located in the first half of the chimney. The maximum value is reached at the base of the stack, at a height of $1,8\ m$. Notice that in the second half the stresses are very low but still negative, indicating that all the fibers in the $+Y$-direction are in compression.
The left graph, figure 6.24b, points out that the maximum tensile strain is occurring at a height of $10,5\ m$. The comparison with figure 6.20 is possible since both graphs are really close in time to each other. It is noticed that the location of

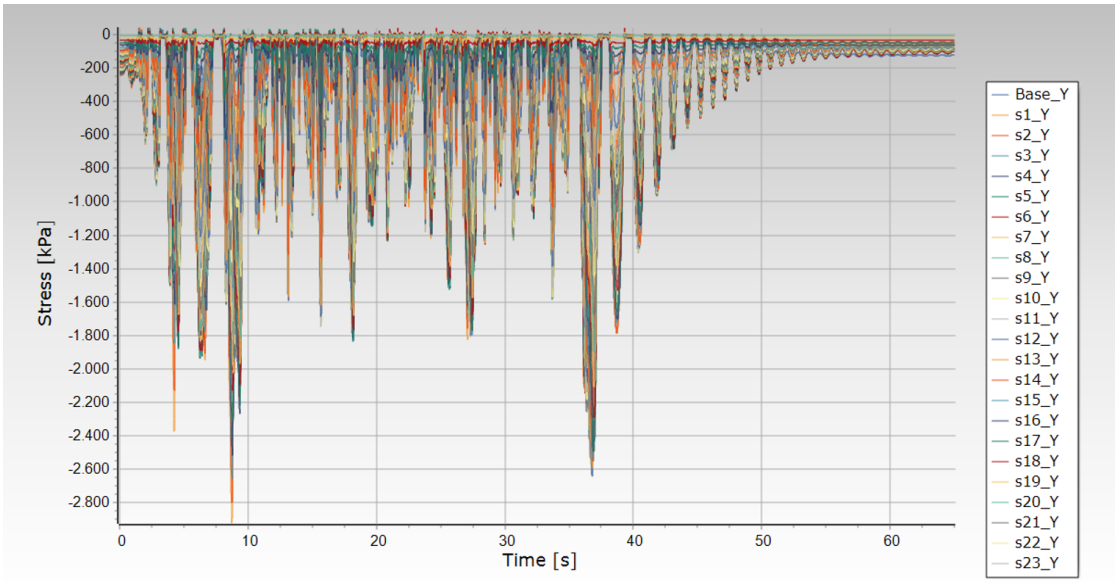

Figure 6.22: Stresses $[kPa]$ over time $[s]$ for the fibers in the $+Y$-direction. The maximum value is $\sigma_t = 40\ kPa$ and the minimum value is $_c = -2921\ kPa$. Assessment in Sagres.

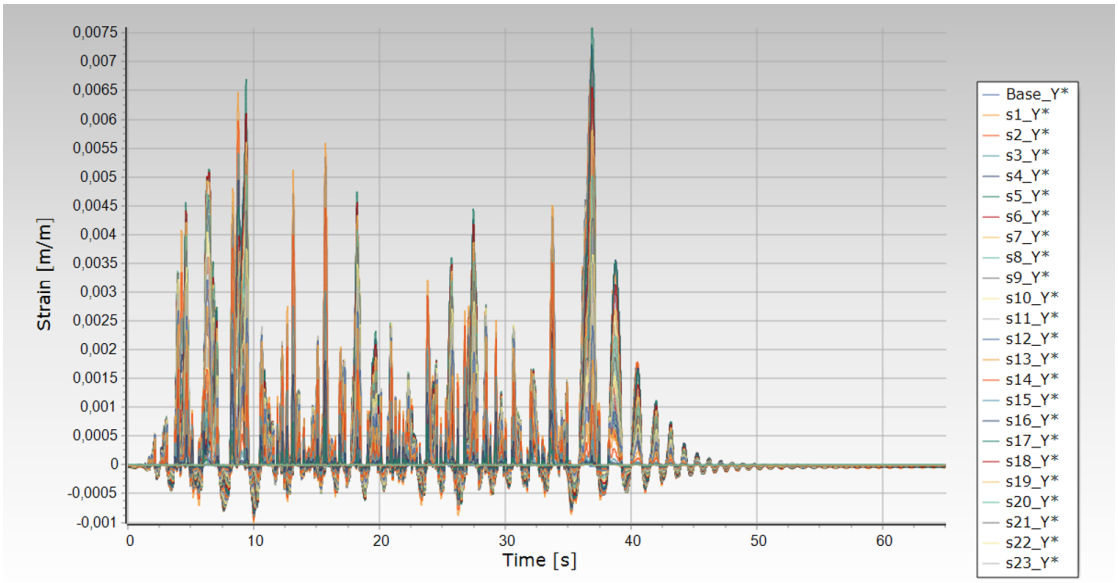

Figure 6.23: Strains $[m/m]$ over time $[s]$ for the fibers in the $-Y$-direction. The maximum value is $\varepsilon_t = 0,0075\ m/m$ and the minimum value is $\varepsilon_c = -0,001\ m/m$. Assessment in Sagres.

the maximum strain corresponds to the location of the maximum curvature of the deformed structure.

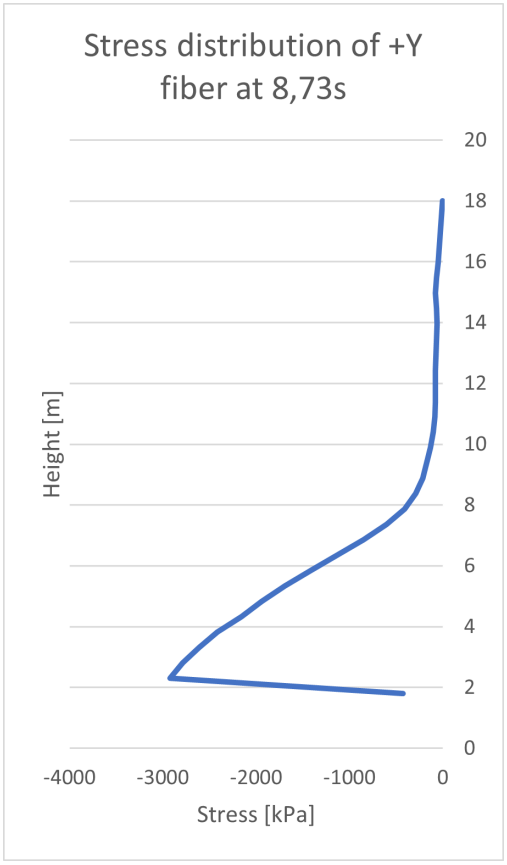

(a) Stress $[kPa]$ distribution in $+Y$-direction fibers.

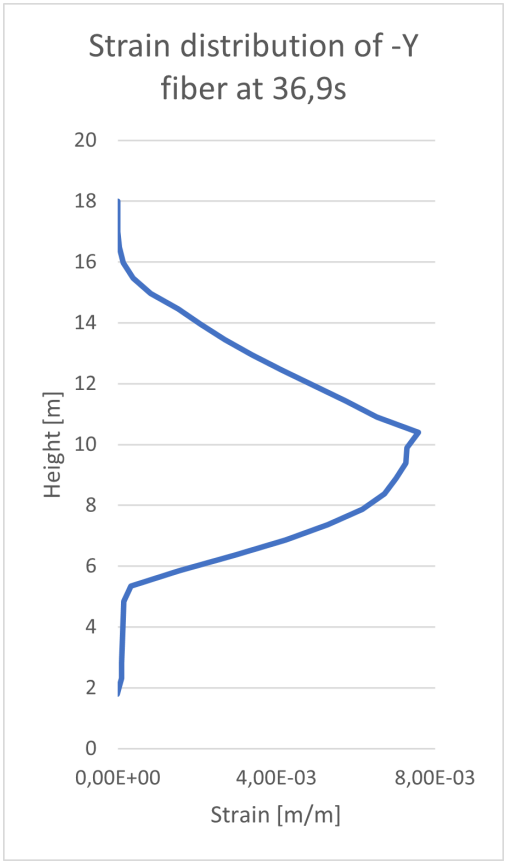

(b) Strain $[m/m]$ distribution in $-Y$-direction fibers.

Figure 6.24: Stress and strain distribution along the height for the assessment in Sagres.

6.3.3 Conclusion

Table 6.2 displays the different values of interest computed by the response spectrum analysis (RSA) and the dynamic time-history analysis (DTHA) for the assessment of the chimney in Sagres.
The maximal top node displacement computed is greater in the time-history analysis. The value of 45 cm is very close to the initial offset of the upper section from its base. This gives an idea of how much the structure would mode.

Table 6.2: Summary of the values computed by the response spectrum analysis (RSA) and the dynamic time-history analysis (DTHA) for the chimney in Lusíada with the seismic conditions of Sagres.

	RSA	DTHA
Maximum top node displacement	31 cm	45 cm
Maximum compression stress	2828 kPa	2921 kPa
Location of the maximum stress	$1,8\ m$	$1,8\ m$
Maximum tensile strain	$9,8 \cdot 10^{-4}\ m/m$	$7,5 \cdot 10^{-3}\ m/m$
Location of the maximum strain	$1,8\ m$	$10,5\ m$

Compared to the previous analysis in Porto, section 6.2.3, the maximum compression stress is still greater in the time-history analysis. But now the values are about 100 kPa apart, compared to $890 - 520 = 370\ kPa$ previously.
For the DTHA, still comparing with section 6.2.3, the maximum compression stress location moved from the middle of the stack to its base, while the maximum strain location remained approximately constant.
In the response spectrum analysis, the maximum strain shifted at the base of the stack, whereas the maximum stress location stayed in place.

The RSA computed tensile stresses in the structure, as it takes the assumptions that the masonry tensile strength is null. The conclusion is that the chimney will need structural reinforcements in order to resist this seismic action. There is no surprise here since the excitation is greater than the one in Porto and already there the structure needed reinforcements.

The conclusion regarding the time-history analysis is less straightforward. Regarding the results displayed, the structure seems to sustain the ground accelerations. However, from the set of eight ground motions, only two converged. The computation crash can be due to a computational error or this means that the model cannot sustain the earthquake in Sagres. In order to draw a more formal conclusion, the model should be further investigated regarding the cause of this non-convergence.

6.4 Comparison with shell elements

The section presents a comparison of analysis for the chimney in Lusíada. The chimney was assessed by the study office NCREP based in Porto. They used a shell element-based software to model it.
Their in-situ investigation was realized with two mono-axial accelerometers placed at the top of the structure. They retrieved the chimney's frequencies using opera-

tional modal analysis.
After building a model based on geometrical assumptions, they performed a calibration process in order to define the structure material properties.
With this calibrated model, denoted NCREP model in the following, they finally performed a response spectrum analysis to evaluate if the structure was at risk.

In the following section, first, the model created by NCREP is presented. Then the model in fiber elements using similar geometrical assumptions is built. After that, both results from response spectrum analysis are compared and finally, the model in fiber elements is subjected to dynamic time-history analysis.

6.4.1 The model in shell elements

The geometry of the model created by NCREP is displayed in figure 6.25a. The model created assumes one squared base with a side of $2,01\ m$ and a height of $1,85\ m$. Then the stack is divided into three different parts of $5,37\ m$ long, making the whole structure $17,95\ m$ tall.
Each part of the stack has a hollow circular cross-section with a constant thickness. From the bottom up, the thicknesses are: $0,49\ m$, $0,37\ m$ and $0,24\ m$. The diameter at the top section is $0,84\ m$ wide.

Figure 6.25b shows that three materials are distinguished in that model. The base and the lower stack are made of material A in green, the medium stack part is in material B in blue and finally material C is in red.
The material properties are summarized in table 6.3.

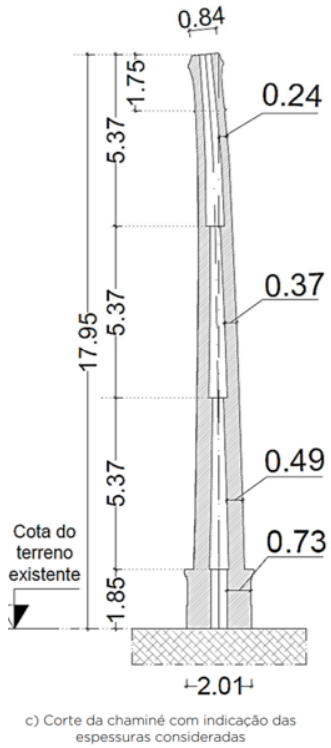

(a) Dimensions used by NCREP.

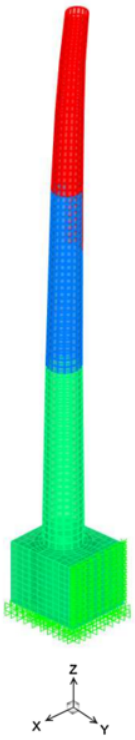

(b) Material used by section.

Figure 6.25: NCREP model of the chimney in Lusíada.

Table 6.3: NCREP model: material properties.

Material	$E\ [GPa]$	$\gamma\ [kN/m^3]$	$f_c\ [kPa]$	Height $[m]$
A	$2,4$	17	2 400	0 to $7,22$
B	$1,6$	17	1 600	$7,22$ to $12,58$
C	$0,8$	17	800	$12,58$ to $17,95$

Regarding the boundary conditions, the chimney is considered embedded in the ground and the side of the base in the $+Y$-direction is considered fixed.

As seen in chapter 4, the previous model developed for the seismic assessment, Model 4, does not assume the same geometry nor the same material properties. For that matter, a new model is created assuming the same geometry as the NCREP model. This model is detailed in the next section.

6.4.2 The model in fiber elements

Figure 6.26 shows a global view of the fiber element model, this model is called Model 5 in the following. Figure 6.27a is the top view of this model. Figure 6.27b shows the top view of the NCREP model. For the sake of clarity, the two models are aligned according to the same coordinate system.

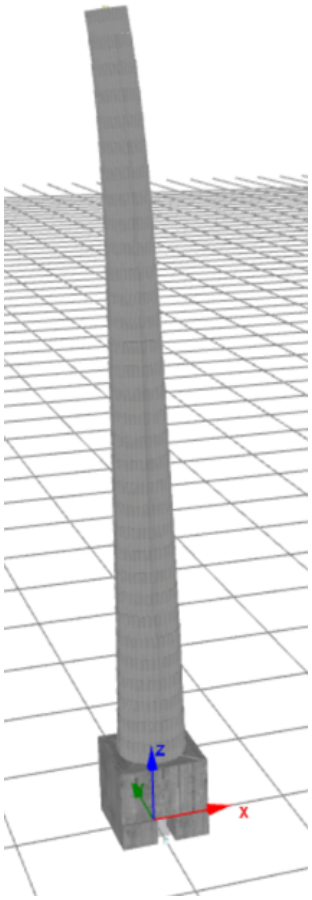

Figure 6.26: View of Model 5.

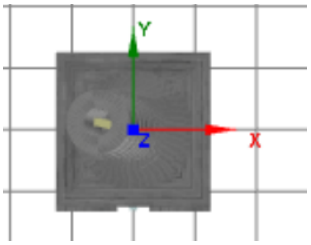

(a) Model 5.

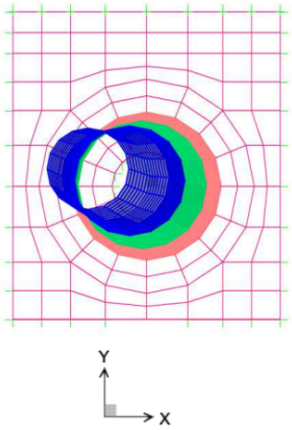

(b) NCREP model.

Figure 6.27: Top views.

Model 5 is computed with the same material properties as the NCREP model. Table 6.5 compares the natural frequencies of the NCREP model and Model 5. The error in frequencies is minimal 17%. This error is too high to say that the model will produce the same results.
Therefore since the geometry is fixed and well explained and that the NCREP model was calibrated based on natural frequencies acquired in-situ, the choice of changing the material parameters is made in order to make the frequencies match. The model with the new material properties is called Model 6. Table **??**

summarizes the new properties adopted for each material.
Table 6.5 displays the frequencies of Model 5 and Model 6, with the error in frequency compared to the NCREP model.

Table 6.4: Model 6: material properties.

Material	$E\ [GPa]$	$\gamma\ [kN/m^3]$	$f_c\ [kPa]$	Height $[m]$
A	$2,0$	19	2 000	0 to $7,22$
B	$1,0$	19	1 000	$7,22$ to $12,58$
C	$0,8$	19	800	$12,58$ to $17,95$

Table 6.5: Frequencies for the NCREP model, Model 5 and Model 6.

	NCREP	Model 5	Error [%]	Model 6	Error [%]
$f_{1,x}\ [Hz]$	$1,05$	$1,26$	$19,6$	$1,04$	$1,1$
$f_{1,y}\ [Hz]$	$1,10$	$1,29$	$17,2$	$1,06$	$3,4$
$f_{2,x}\ [Hz]$	$3,72$	$4,41$	$18,4$	$3,75$	$0,9$
$f_{2,y}\ [Hz]$	$3,86$	$4,57$	$18,5$	$3,91$	$1,4$
$f_{3,x}\ [Hz]$	$8,93$	$10,46$	$17,2$	$9,03$	$1,1$
$f_{3,y}\ [Hz]$	$9,06$	$10,99$	$21,2$	$9,45$	$4,3$

Figure 6.28 shows the fourth mode of vibration of Model 4, the NCREP model, and Model 6. The rest of the mode shapes can be found in appendix F. The mode shape of Model 6 fits better the experimental data regarding the Y-direction than Model 4 but is straight in the X-direction. The straight shape is due to the fixed base side.

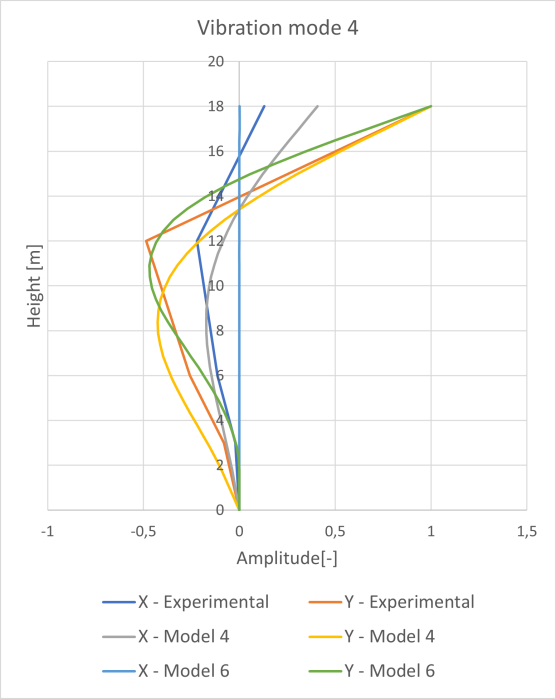

Figure 6.28: Fourth vibration mode shape for Model 4 and Model 6.

6.4.3 Response spectrum analysis

The spectrum used for the analysis is the same as the one presented in section 6.2.1.
Figure 6.29b shows the envelope of stresses obtained for the stack of Model 6, from the eight seismic combinations:

$$E = \pm 100\% \cdot E_X \pm 30\% \cdot E_Y$$
$$E = \pm 100\% \cdot E_X \pm 30\% \cdot E_Y$$

Figure 6.29a shows the results of the NCREP model. The SRSS combination rule is used to compute these results.

The maximal compression stress in both models is located near the stack base in the $-X$-direction. Its value is close to $\sigma_c = -500\ kPa$.
The maximum tensile stresses computed have a value of about $\sigma_t = 100\ kPa$ and are located around $2/3^{rd}$ of the stack height in the $-Y$-direction.
In both models, there are jumps around $1/3^{rd}$ and $2/3^{rd}$ of the stack. Those jumps occur where cross sections change in thickness.

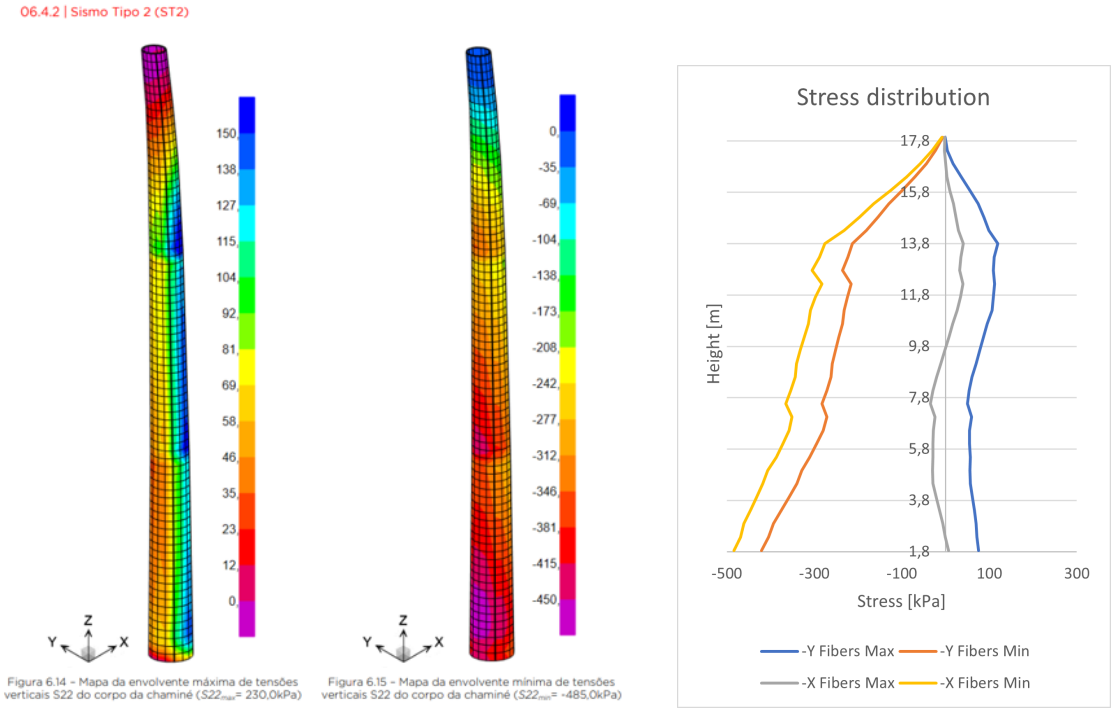

(a) Stress computed with finite elements (b) Stress computed with Model 6

Figure 6.29: Stress envelopes computed with RSA.

6.4.4 Dynamic time-history analysis

Running the set of the eight ground motions displayed in appendix D, the one given the largest top node displacement is Serie 1 with the combination $100\%E_X + 30\%E_Y$.

The subject of interest is to compare the location and amplitude of the stresses computed in the structure with the ones computed in the response spectrum analysis.
To do so, the stress distributions, at the time step where the corresponding stress is maximum, are compared with the results from the finite element model.

Figure 6.30 plots the stresses of the fibers in the $-X$-direction over time. The maximum compression stress occurs at $13,7s$ with a value of 651 kPa.
Figure 6.31 plots the stresses of the fibers in the $-Y$-direction. The maximum compression stress is reached at $13,25$ s with a value of 291 kPa.
In both plots, the fibers reached their tensile strength of 40 kPa.

Figure 6.32 shows side by side the stress envelope obtained for the chimney stack by the response spectrum analysis with the finite element model and the stresses obtained with the dynamic time-history analysis. As the maximum tensile

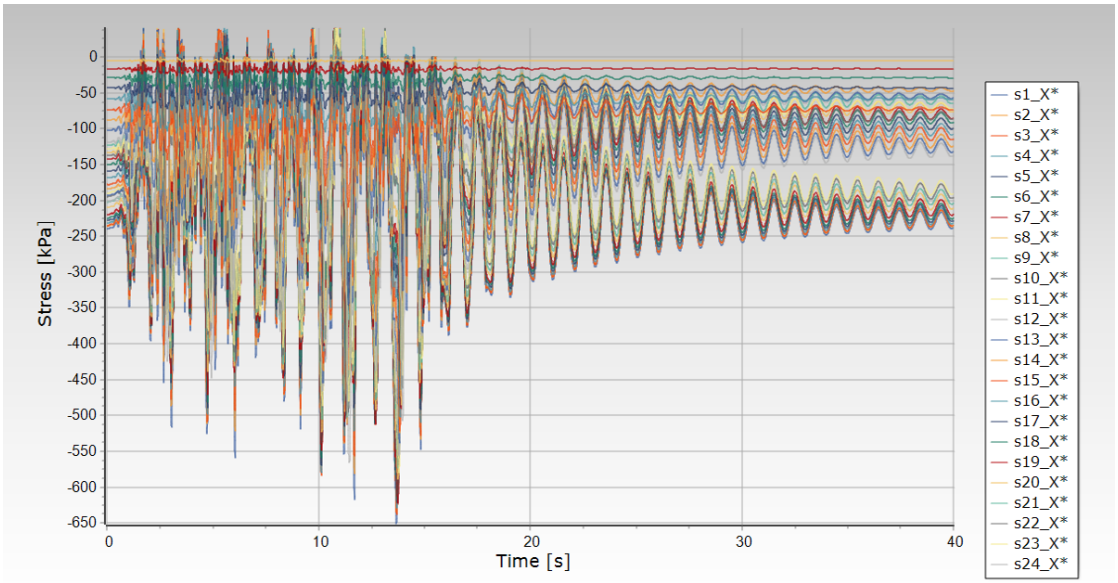

Figure 6.30: Stresses $[kPa]$ over time $[s]$ for the fibers in the $+Y$-direction. The maximum value is $\sigma_t = 40\ kPa$ and the minimum value is $_c = -651\ kPa$.

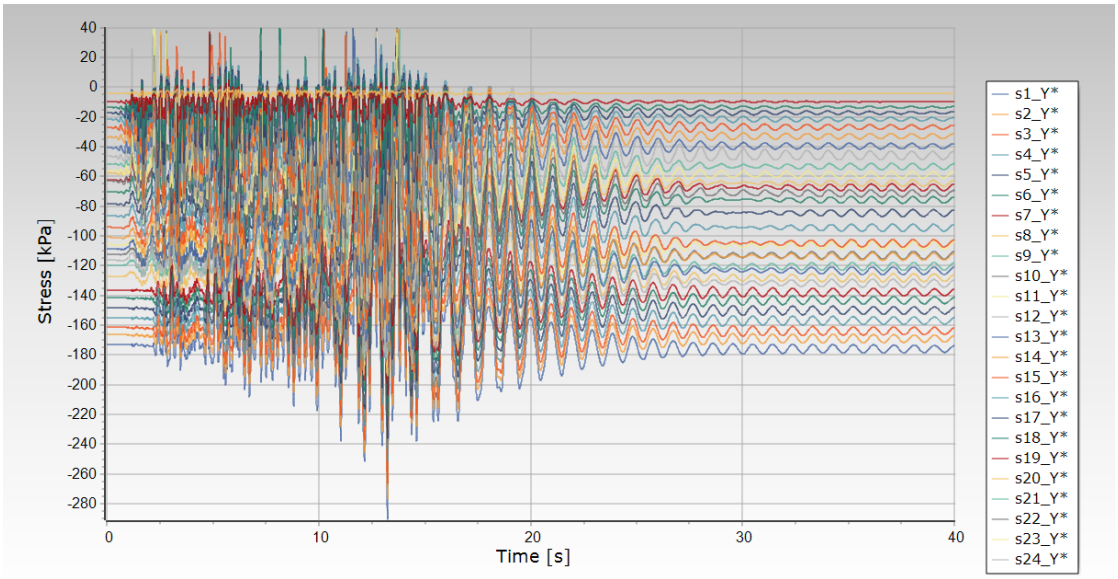

Figure 6.31: Stress $[kPa]$ over time $[s]$ for the fibers in the $-Y$-direction. The maximum value is $\sigma_t = 40\ kPa$ and the minimum value is $\sigma_c = -291\ m/m$.

stresses obtained with the DTHA cannot be superior to the tensile strength assigned $f_t = 40\ kPa$, only the compression stresses are compared.
In figure 6.32a, the minimum stresses (purple zone) are smaller than $-450\ kPa$ and located in the $-X$-direction. Then from the bottom up following the $-X$-direction the stresses go almost regularly to zero. With two jumps due to the change in thickness in the cross sections. In figure 6.32b, the stresses in the $-X$-direction are represented by the blue curve. The minimum value located at the base of the stack is smaller than $-600\ kPa$. Then the distribution goes to zero at the top. This compression stress occurs at the lower part of the stack where the material compression strength is $2\,000\ kPa$. Even though, the lowest compression strength of $800\ kPa$ of Material C is never reached at any point.
In the $-Y$-direction, the colored map indicates a maximal compression stress around $415\ kPa$, while in the fiber element model the maximum value is around $300\ kPa$.

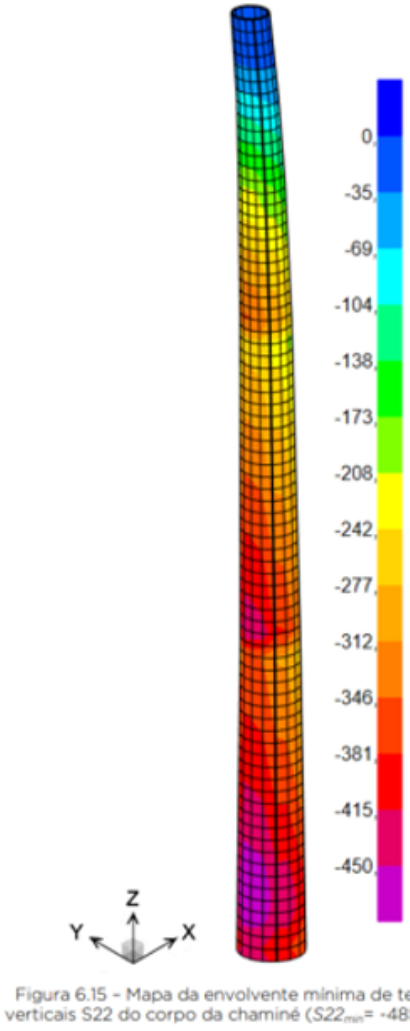

(a) Compression stresses computed with finite elements.

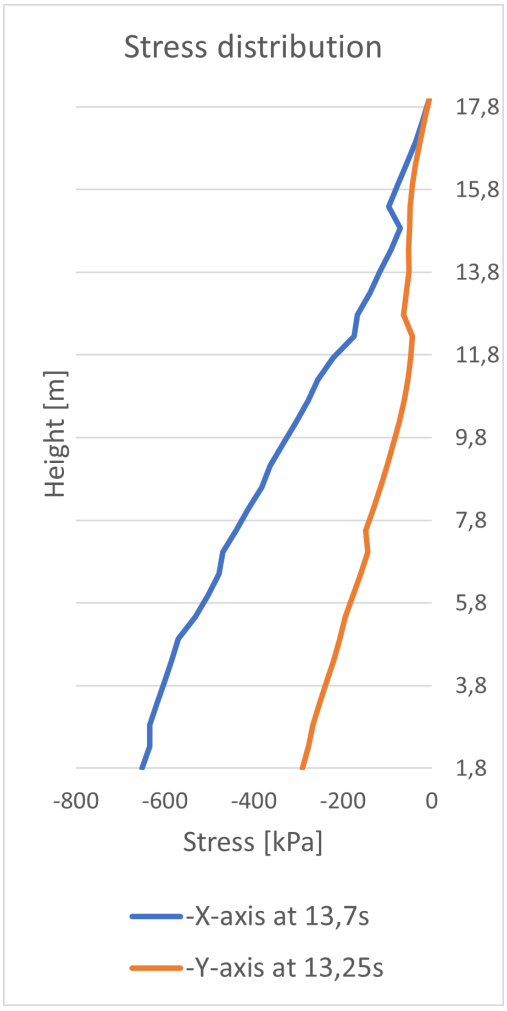

(b) Stress computed with Model 6 and the dynamic time-history analysis.

Figure 6.32: Stresses distributions.

6.4.5 Conclusion

This section showed a comparison between modeling the same structure with finite element-based software and fiber element-based software.
First of all, it was noticed that even with the same geometry and material properties, the two models would not give the same natural frequencies. The model in finite elements is more refined than the one in fiber and so more flexible because its

elements are way smaller. This could be an explanation for the lower frequencies. Regarding the results from the response spectrum analysis, both models gave similar results. This would show that the fiber element vibration modes are a good estimation of the ones from the NCREP model.

The dynamic time-history analysis of Model 6 showed that the model could sustain a seismic event in Porto. The compression stresses computed are way below the compression strength of the masonry:

$$600 << 2000\ kPa$$

And considering the plasticity of the material, the model lives through the earthquake.
This last conclusion is what separates the two analyses. Where the finite model, assuming an elastic behavior, would recommend some structural reinforcements, the fiber element model shows that the structure is fine just as it is. So in this case, while nonlinear analysis takes more time to do, it significantly reduces the cost of the intervention.

Chapter 7

Conclusion

This work sought to determine if a chimney could withstand an earthquake corresponding to its geographic region. In order to do so, we first used EMA to identify the dynamic properties of the chimney in order to reduce the amount of material to be used in the experiments.
Then, based on a geometric survey, a numerical fiber element model of the stack was defined. To determine the material properties of this model, their values were iterated in order to match the frequencies and vibration modes of the model with those identified experimentally.
After that, two seismic analyses were performed, the first one following the response spectrum proposed by the Eurocode 8, and the second one is a numerically solved temporal analysis for a given seismic acceleration.
Finally, the work ends with a comparison of the results obtained by the analysis of the seismic response of a model realized with shell-type finite elements and a model realized with fiber elements.

Regarding the acquisition of experimental data, two stacks located in the vicinity of Porto have been addressed. The two modal analysis methods that are the operational modal analysis and the experimental modal analysis were used. The purpose of using the operational modal analysis was to obtain results similar to the OMA without the need for a lifting platform. This has the advantage of reducing the cost and duration of the investigation. This goal was not achieved because the EMA experiments produced only poor results.
The investigation campaign revealed a better estimation of the structural dynamic properties by the operational modal analysis. The first four vibration modes could be determined for one stack, which allowed the development of a numerical model.

Four different numerical models were established, assuming different geometries and support conditions. The calibration of these models was based on the definition

of the properties of the constitutive materials. To compare the frequencies and modes obtained numerically to those obtained experimentally, the Modified Total Modal Assurance Criterion (MTMAC) was used.
The model selected for the seismic analysis uses a detailed geometry of the structure and models an elastic soil.

The model was first analyzed under Porto conditions. First with the response spectrum analysis under assumptions of elastic behavior. Then with a dynamic time analysis with the assumption of a nonlinear material. The RSA concluded that the chimney would need structural reinforcement, while the nonlinear analysis concluded that the chimney could survive a seismic event in the Porto region.
The question was then asked whether the chimney could survive the most severe possible earthquake in Portugal. However, the model did not converge for all evaluated ground accelerations. The issue of whether this is due to a modeling error or simply a model failure could be investigated further.

In the end, part of the seismic analysis turned on the comparison of the results obtained between a numerical model made with 2D finite elements and another one made with fiber elements. The comparison showed that the use of the fiber elements allowing the nonlinear calculation of the structure brings an advance as for the general conclusions in quality of structural resistance to the seisms.
The relevance of the study of the nonlinear behavior of the structure was thus well founded and showed a progression in the apprehension of the structural problem that is the seismic analysis of the industrial chimneys in masonry.
Through this work, the time-history analysis has been only slightly addressed. More detailed analyses could be conducted in this area in order to determine more precisely the nonlinear behavior of masonry chimneys.

From a personal point of view, I am grateful to have been able to carry out this large-scale project because of the knowledge that I was able to acquire and the skills that I was able to develop. I am glad that I was able to learn the basics of a mechanical testing laboratory. I am thankful that I was able to live two months of my life in the beautiful city of Porto. This experience made me meet great people but most of all it made me discover new facets of the engineering profession that I didn't even imagine.

Bibliography

Alipour, A, Farzin Zareian, and Phd Student (June 2008). "Study Rayleigh damping in structures; unceratinties and treatments". In:

Anil K. Chopra (2012). *Dynamics of structures*. Ed. by Pearson Education. 4th ed. ISBN: 9780133072693.

Batel, Mehdi and Brüel Kjaer (2002). "Operational Modal Analysis – Another Way of Doing Modal Testing". In:

Costa, A, M Sousa, and A Carvalho (June 2008). "Seismic zonation for Portuguese National Annex of Eurocode 8". In:

Guedes, João M. et al. (2019). "Brick masonry industrial chimneys: Assessment, evaluation and intervention". In: *Philosophical Transactions of the Royal Society A: Mathematical, Physical and Engineering Sciences* 377.2155. ISSN: 1364503X. DOI: 10.1098/rsta.2019.0012.

João Almeida (2021). *Earthquake engineering*.

Lacanna, G. et al. (Apr. 2020). "Dynamic Identification as a Tool to Constrain Numerical Models for Structural Analysis of Historical Buildings". In: *Frontiers in Built Environment* 6, p. 40. ISSN: 22973362. DOI: 10.3389/FBUIL.2020.00040/BIBTEX.

Linnet Gjelstrup, Soren (Mar. 2021). *What is Modal Analysis: The Ultimate Guide | Dewesoft*. URL: https://dewesoft.com/daq/what-is-modal-analysis.

Lopes, Valter et al. (2009). "Ambient vibration testing and seismic analysis of a masonry chimney". In: *Journal of Building Appraisal*. Vol. 5. 2. DOI: 10.1057/jba.2009.24.

López-Patiño, Gracia et al. (Apr. 2017). "Causes of damage to industrial brick masonry chimneys". In: *Engineering Failure Analysis* 74, pp. 188–201. ISSN: 13506307. DOI: 10.1016/j.engfailanal.2017.01.014.

Masciotta, Maria Giovanna et al. (Jan. 2017). "Damage identification and seismic vulnerability assessment of a historic masonry chimney". In: *Annals of Geophysics* 60.4. ISSN: 15935213. DOI: 10.4401/ag-7126.

Melchers, R. E. (1992). "Rotational stiffness of shallow footings". In: *Computers and Geotechnics* 13.1. ISSN: 0266352X. DOI: 10.1016/0266-352X(92)90009-I.

Minghini, Fabio, Gabriele Milani, and Antonio Tralli (2014). *Seismic risk assessment of a 50 m high masonry chimney using advanced analysis techniques*. Tech. rep.

Pallarés, Francisco J., Antonio Agüero, and Manuel Martín (Apr. 2006). "Seismic behaviour of industrial masonry chimneys". In: *International Journal of Solids and Structures* 43.7-8, pp. 2076–2090. ISSN: 00207683. DOI: 10.1016/j.ijsolstr.2005.06.014.

Pallarés, Francisco J., Salvador Ivorra, et al. (Dec. 2011). "State of the art of industrial masonry chimneys: A review from construction to strengthening". In: *Construction and Building Materials* 25.12, pp. 4351–4361. ISSN: 0950-0618. DOI: 10.1016/J.CONBUILDMAT.2011.02.004.

PCB piezotronics, https://www.pcb.com (Aug. 2022).

Qingkai Kong, Timmy Siauw, and Alexandre M. Bayen (2021). *Python Programming and Numerical Methods*. Elsevier. ISBN: 9780128195499. DOI: 10.1016/C2018-0-04165-1.

Ramos et al. (2013). *SHM of a Masonry Chimney after a Lightning Accident*. Tech. rep.

Sancibrian, R. et al. (Jan. 2017). "Dynamic identification and condition assessment of an old masonry chimney by using modal testing". In: *Procedia Engineering* 199, pp. 3410–3415. ISSN: 1877-7058. DOI: 10.1016/J.PROENG.2017.09.485.

Santoro, Valentino, Elisa Bassoli, and Loris Vincenzi (2021). "Dynamic Identification and Model Updating of a Masonry Chimney". In: *Lecture Notes in Civil Engineering* 156, pp. 535–556. ISSN: 23662565. DOI: 10.1007/978-3-030-74258-4{_}35.

Schwarz, Brian J and Mark H Richardson (1999). "EXPERIMENTAL MODAL ANALYSIS". In:

Seismosoft (2022). *"SeismoStruct 2022 – A computer program for static and dynamic nonlinear analysis of framed structures," available from https://seismosoft.com/.*

Chapter 8

Appendices

A Chimney in Aguas Santas: Mode shapes from OMA.

A.1 $f_{1,x} = 0,79\ Hz$

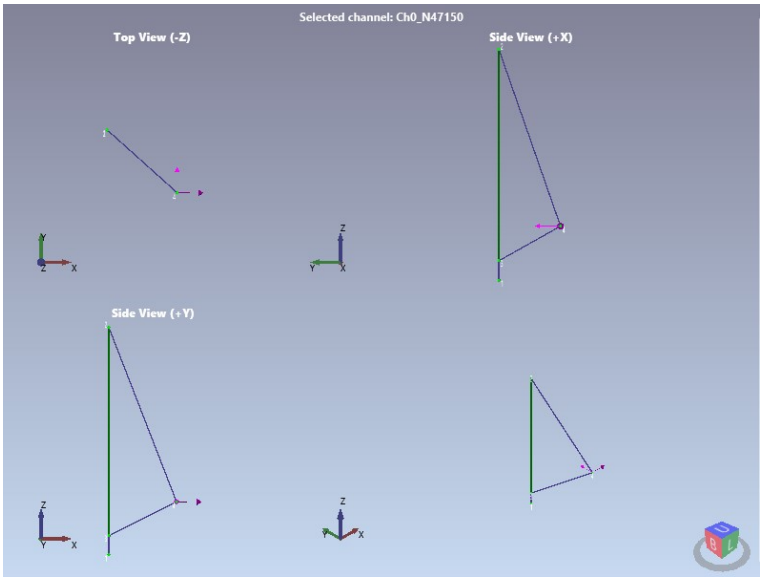

A.2 $f_{1,y} = 0,85\ Hz$

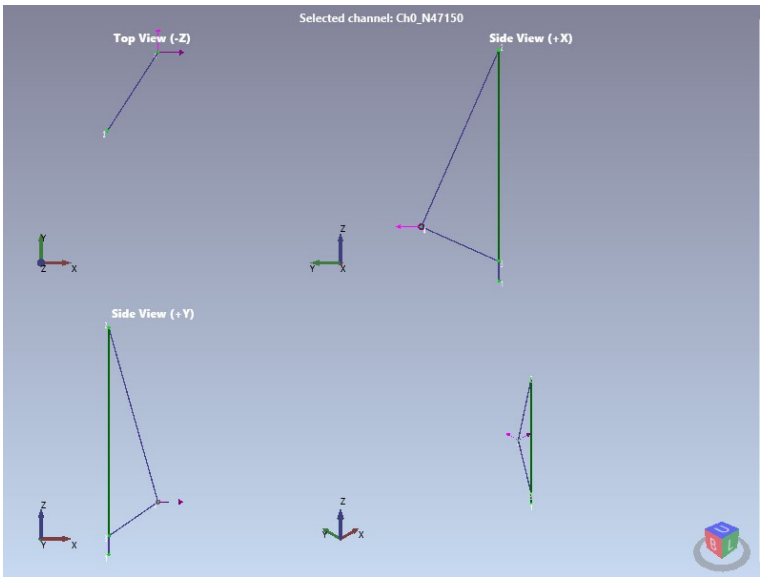

A.3 $f_{2,x} = 2,66\ Hz$

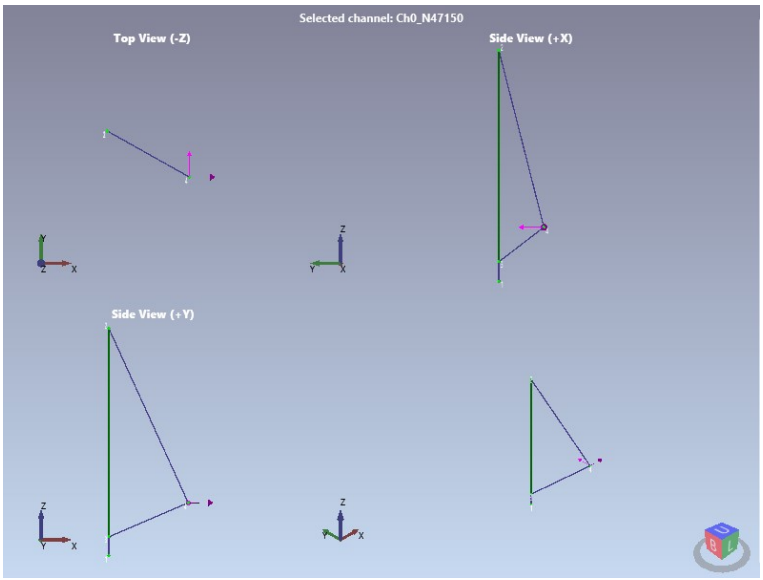

A.4 $f_{2,y} = 2,95\ Hz$

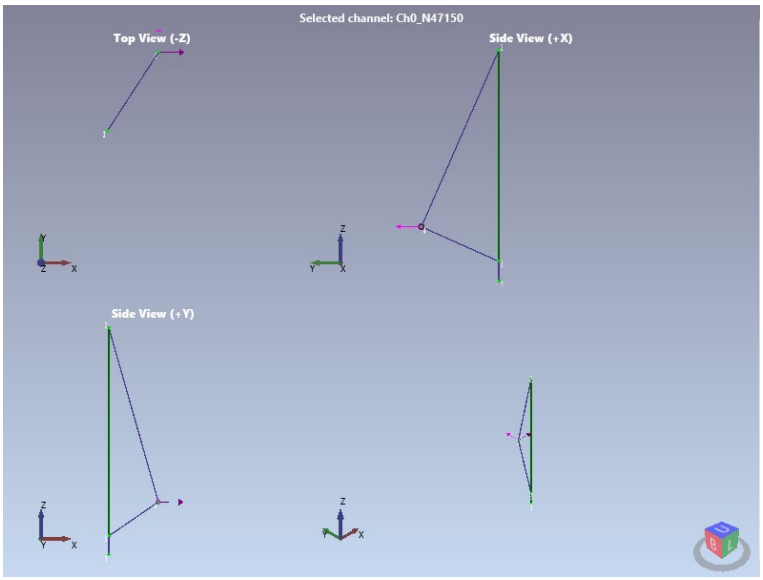

A.5 $f_{3,x} = 5,69\ Hz$

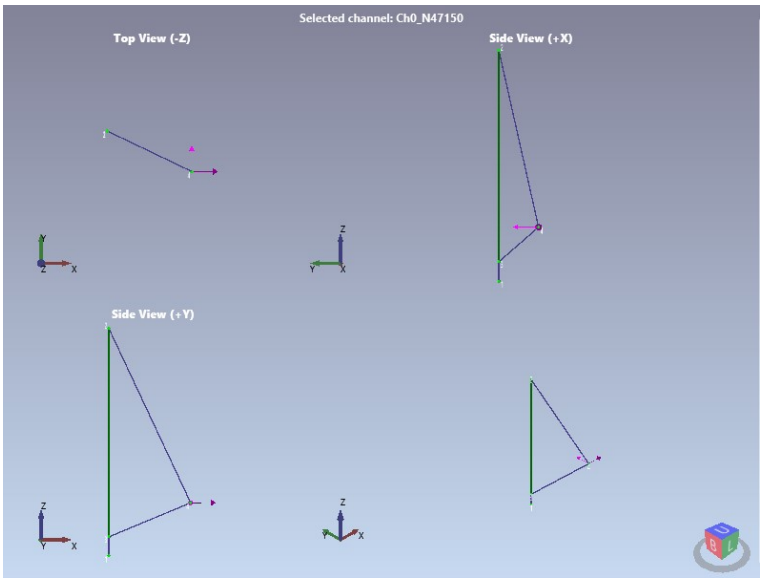

A.6 $f_{3,y} = 6,40\ Hz$

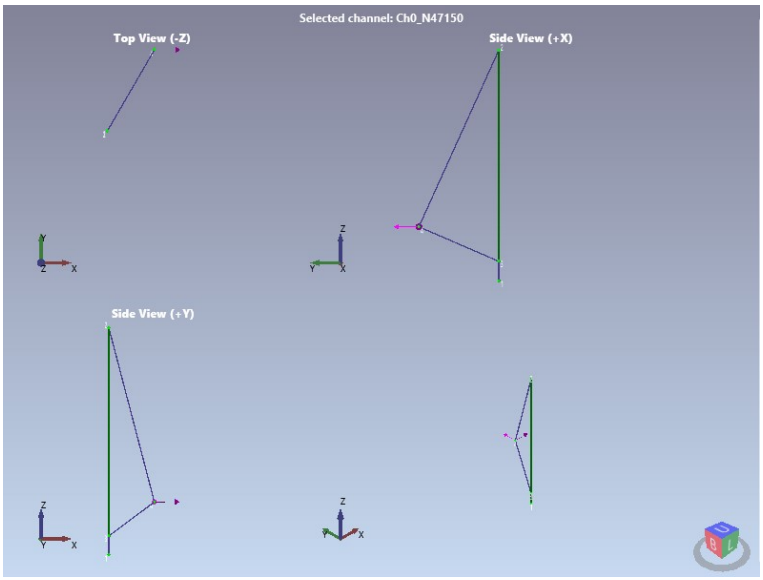
Selected channel: Ch0_N47150
Top View (-Z)
Side View (+X)
Side View (+Y)

B Derivation of soil's properties

Knowing the rotational stiffness of the soil and the foundation geometry, the soil's modulus of elasticity can be derived and matched with a certain type of soil. Melchers 1992 gives us the following relations:

$$K_b = \frac{b^2 \cdot l \cdot E_b}{(1-\nu^2) \cdot I_\Theta} \; [Nm/rad] \tag{8.1}$$

$$I_\Theta = \frac{16}{\pi \cdot \left(1 + 0,22\frac{b}{l}\right)} \; [rad] \tag{8.2}$$

Where K_b, b, l, E_b and ν are respectively the soil's stiffness, the base width, the base length, the soil's modulus of elasticity and the Poisson ratio. Melchers 1992 assumes a value of $\nu = 0,3$ for a soil.
The assumptions taken in chapter 5, of a rotational stiffness

$$K_{soil} = 4 \cdot 10^5 \; [kNm/rad]$$

and the square base of side of 2 m derives E_b.

$$I_\Theta = \frac{16}{\pi \cdot \left(1 + 0,22\frac{2}{2}\right)} \tag{8.3}$$

$$= 4,18 \; [rad] \tag{8.4}$$

$$K_b = \frac{2^2 \cdot 2 \cdot E_b}{(1-0,3^2) \cdot 4,18} \tag{8.5}$$

$$= 2,1 \cdot E_b \tag{8.6}$$

$$\Leftrightarrow E_b = \frac{4 \cdot 10^5}{2,1} = 190,5 \; [MPa] \tag{8.7}$$

According to typical soil elastic properties, displayed in the table in figure 8.1, a value of $E_b = 190,5 \; [MPa]$ can correspond to a dense sand and gravel or a very stiff clay.

SOIL DESCRIPTION	ELASTIC MODULUS E (MPa)	POISSON'S RATIO ν	SOURCE
Soft Clay	0.5 – 5	0.15 – 0.25, 0.45	K, D, d
Medium Clay	1.0 – 10	0.2 – 0.5	K, D
Stiff Clay		~ 0.4	B, d
Hard Clay	6 – 15		D
Very Stiff Clay	25 – 200		d
Silty Sand	7 – 70	0.2 – 0.4	d, D
Loose Sand	10 – 50	0.2 – 0.4	d, D
Medium Sand		0.25 – 0.4	D
Dense Sand	35 – 120	0.3 – 0.45	d, D
Dense Sand and Gravel	90 – 200		d
Sandstone	< 50000		d
Chalk	5000 – 20000		d
Limestone	25000 – 100000	0.34	d, K
Basalt	15000 – 100000	0.34	d, K

Figure 8.1: Typical soil elastic properties

C Computation of the design spectrum following EC8

The first parameters to determine is the type of soil under the structure. Given the assumptions made in chapter 5, the soil can either be a "very dense sand, gravel", or a "very stiff clay". In the Eurocode 8, such type of soils are are described by a Ground type B, as shown in figure 8.2.
The type of soil defines also the values of S_{max}, T_B, T_C and T_D. The values are given in Table 8.1. The value of S depends on the the value of $S_{\max}$ and $a_g = \gamma_I \cdot a_{gR}$:

$$\begin{array}{ll} \text{para } a_{\mathrm{g}} \leq 1 \text{ m/s}^2 & S = S_{\max} \\ \text{para } 1 \text{ m/s}^2 < a_{\mathrm{g}} < 4 \text{ m/s}^2 & S = S_{\max} - \frac{S_{\max}-1}{3}\,(a_{\mathrm{g}} - 1) \\ \text{para } a_{\mathrm{g}} \geq 4 \text{ m/s}^2 & S = 1,0 \end{array}$$

Eurocode 8

Table 3.1: Ground types

Ground type	Description of stratigraphic profile	Parameters		
		$v_{s,30}$ (m/s)	N_{SPT} (blows/30cm)	c_u (kPa)
A	Rock or other rock-like geological formation, including at most 5 m of weaker material at the surface.	> 800	–	–
B	Deposits of very dense sand, gravel, or very stiff clay, at least several tens of metres in thickness, characterised by a gradual increase of mechanical properties with depth.	360 – 800	> 50	> 250
C	Deep deposits of dense or medium-dense sand, gravel or stiff clay with thickness from several tens to many hundreds of metres.	180 – 360	15 - 50	70 - 250
D	Deposits of loose-to-medium cohesionless soil (with or without some soft cohesive layers), or of predominantly soft-to-firm cohesive soil.	< 180	< 15	< 70
E	A soil profile consisting of a surface alluvium layer with v_s values of type C or D and thickness varying between about 5 m and 20 m, underlain by stiffer material with v_s > 800 m/s.			
S_1	Deposits consisting, or containing a layer at least 10 m thick, of soft clays/silts with a high plasticity index (PI > 40) and high water content	< 100 (indicative)	–	10 - 20
S_2	Deposits of liquefiable soils, of sensitive clays, or any other soil profile not included in types A – E or S_1			

Figure 8.2: Table describing the different soil type assumed in the Eurocode 8

Soil type	$S_{\max}$	$T_B(s)$	$T_C(s)$	$T_D(s)$
A	1,0	0,1	0,6	2,0
B	1,35	0,1	0,6	2,0
C	1,6	0,1	0,6	2,0
D	2,0	0,1	0,8	2,0
E	1,8	0,1	0,6	2,0

(a) Seismic action of type 1

Soil type	$S_{\max}$	$T_B(s)$	$T_C(s)$	$T_D(s)$
A	1,0	0,1	0,25	2,0
B	1,35	0,1	0,25	2,0
C	1,6	0,1	0,25	2,0
D	2,0	0,1	0,3	2,0
E	1,8	0,1	0,25	2,0

(b) Seismic action of type 2

Table 8.1: Seismic parameters depending on the type of seismic action and soil.

In Portugal, the peak ground acceleration, PGA or a_{gR}, varies from a region

to another but is also different regarding the type of earthquake. The Portuguese national annex provides those PGA through the maps in figure 8.3 and table 8.2. Porto is located in the seismic zone n°1.6 for the seismic action of type 1, which gives a PGA of $a_{gR} = 0,35\ [m/s^2]$. For the type 2, $a_{gR} = 0,8\ [m/s^2]$.
The importance factor γ_I in this case is equal to 1, as the structure, a chimney is neither a building of minor importance for public safety as it is here located in a residential area, as explained in Section 3.2. Its collapse would not touch a consequent number of human beings and therefore its integrity is not in the order of public safety.

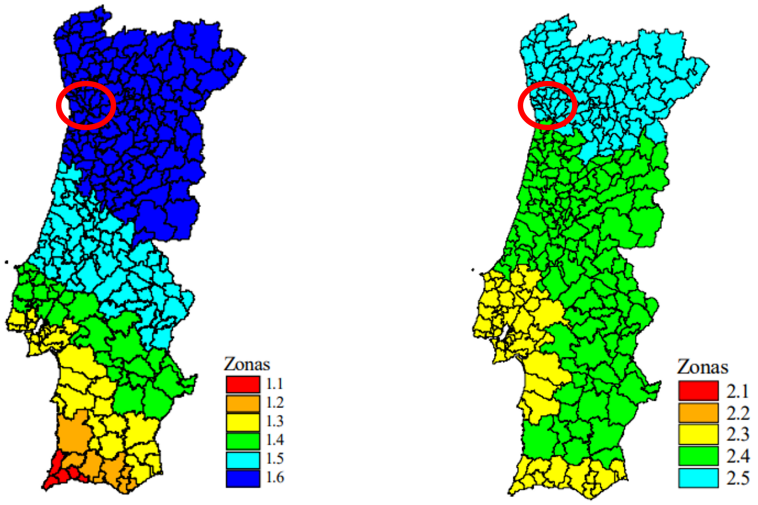

Figure 8.3: Maps providing the value of PGA to use in Portugal, Costa, Sousa, and Carvalho 2008.

Seismic action type 1		Seismic action type 2	
Seismic zone	a_{gR} (m/s^2)	Zona Sísmica	a_{gR} (m/s^2)
1.1	2,5	2.1	2,5
1.2	2,0	2.2	2,0
1.3	1,5	2.3	1,7
1.4	1,0	2.4	1,1
1.5	0,6	2.5	0,8
1.6	0,35	-	-

Table 8.2: Table providing the value of PGA to use in Portugal, Costa, Sousa, and Carvalho 2008.

Importance class	Buildings	Type 1	Type 2	
			Continent	Azores
I	Buildings of minor importance for public safety, e.g. agricultural buildings, etc.	0,65	0,75	0,85
II	Ordinary buildings, not belonging in the other categories.	1	1	1
III	Buildings whose seismic resistance is of importance in view of the consequences associated with a collapse, e.g. schools, assembly halls, cultural institutions etc.	1,45	1,25	1,15
IV	Buildings whose integrity during earthquakes is of vital importance for civil protection, e.g. hospitals, fire stations, power plants, etc.	1,95	1,5	1,35

Table 8.3: Table providing the value of importance factor γ_I.

In order to determine the Design spectrum for elastic analysis, the last parameter to set is the behavior factor q. The Eurocode 8 defines the behavior factor to take into account the effect of ductility and redundancy synonym of its dissipation capacity, and the global inherent overstrength present in the structure. Like this the elastic analysis can be carried on knowing that the building will not behave perfectly elastically in reality. A building with a high ductility capacity will have a high behavior factor.

The minimum value of q is $1,5$. Taking $q = 1$ would be equivalent of saying that the structure behaves elastically at all times.
As the chimney is considered as a simple cantilever, its redundancy is null. However, it is still assumed that a little bit of energy can be dissipated through cracking of the mortar and the sliding of the bricks. That is the reason why the minimum value of the behavior factor is chosen for this type of structure.

D Set of ground accelerations for the analysis in Porto

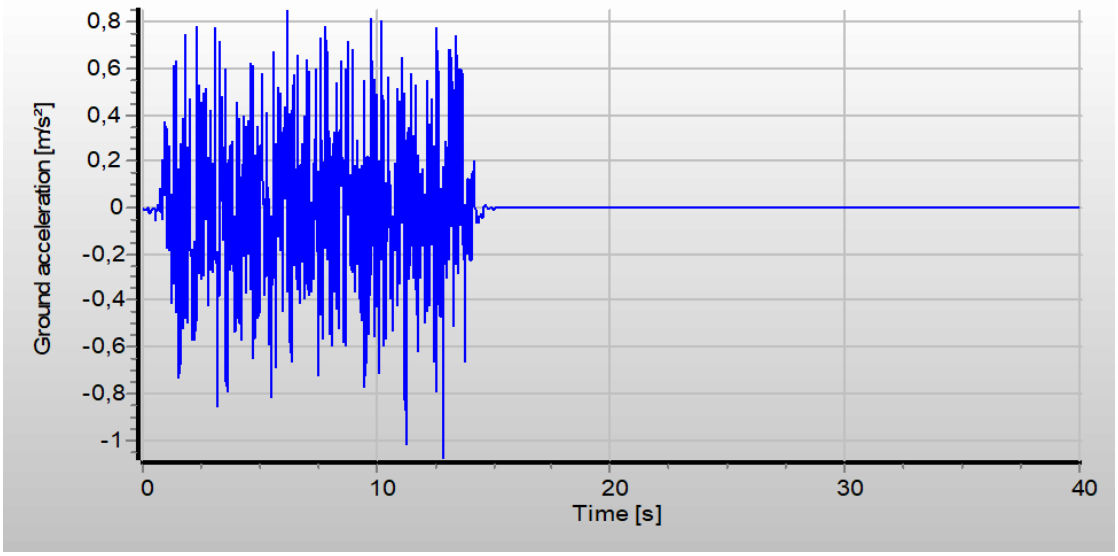

Figure 8.4: Serie 1.

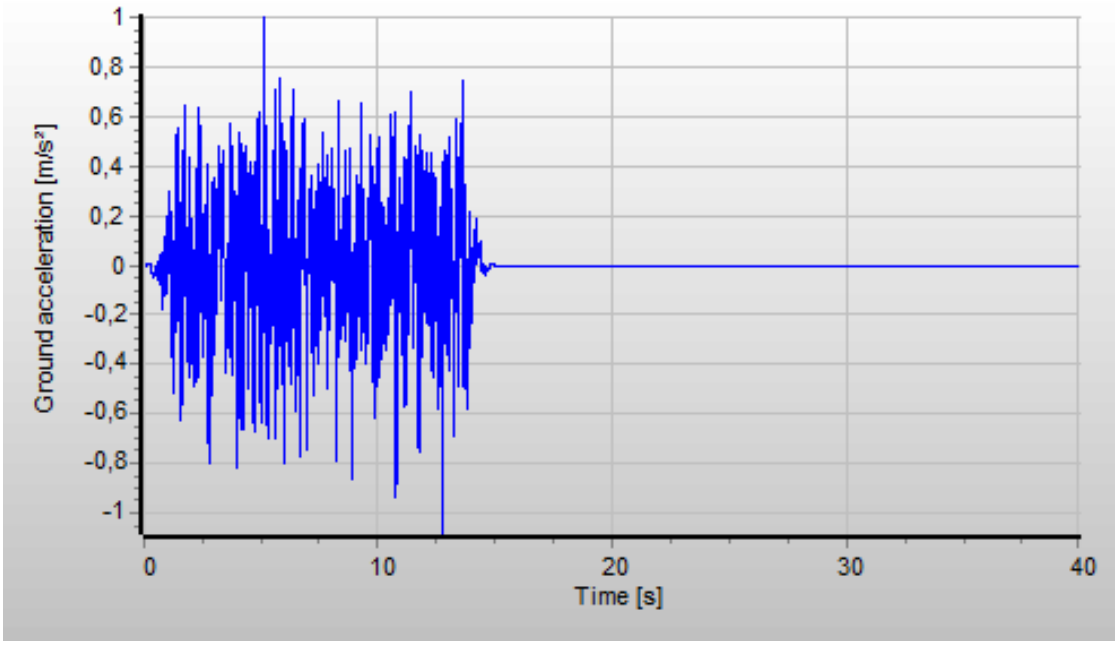

Figure 8.5: Serie 2.

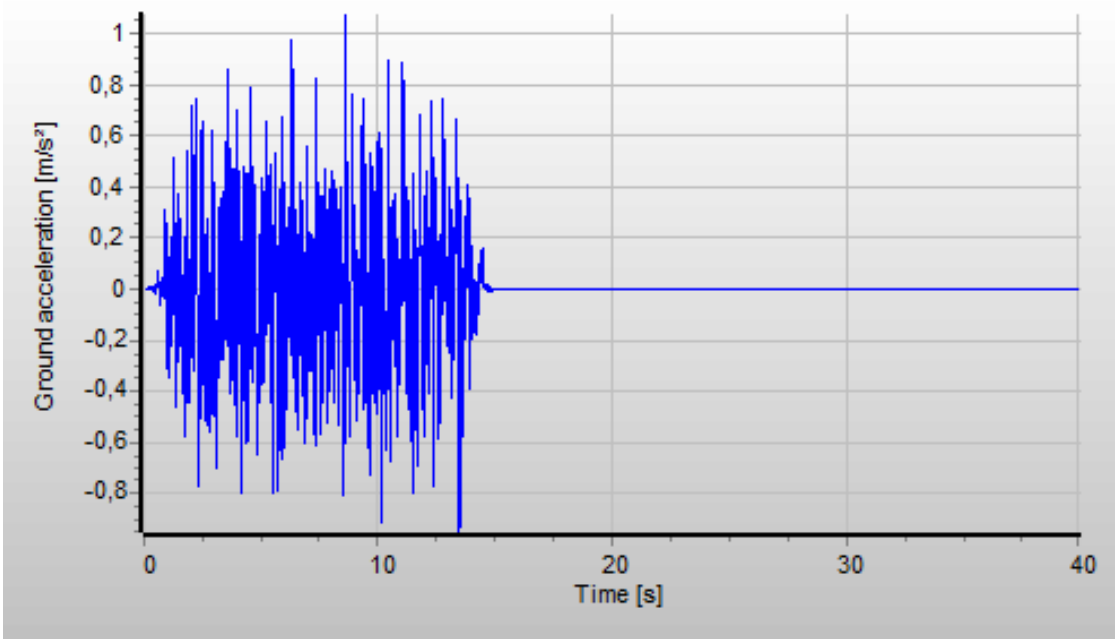

Figure 8.6: Serie 3.

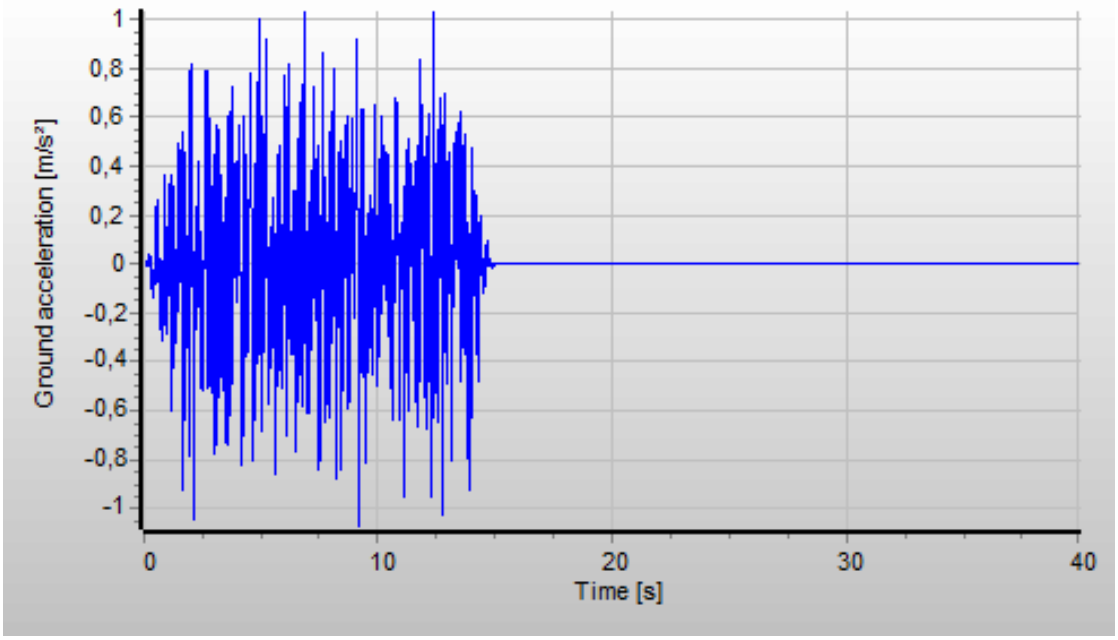

Figure 8.7: Serie 4.

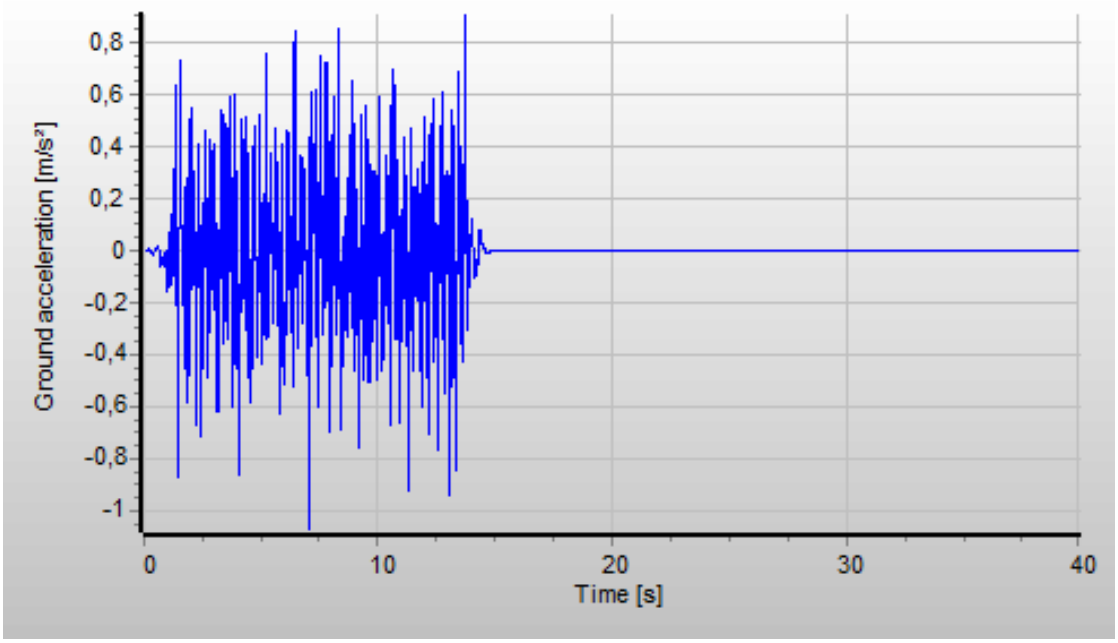

Figure 8.8: Serie 5.

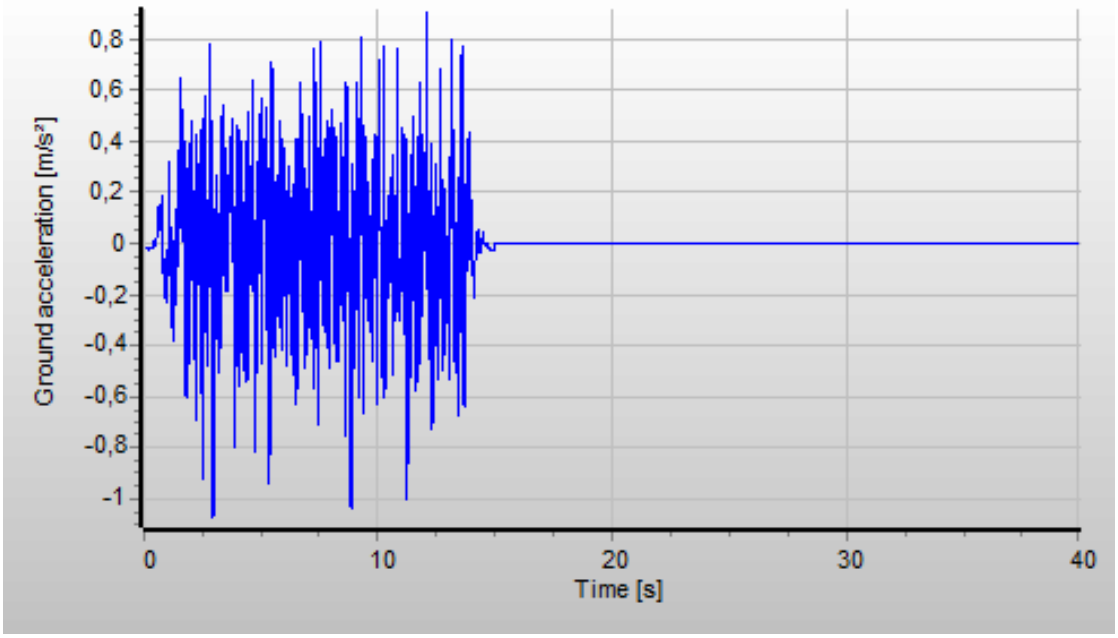

Figure 8.9: Serie 6.

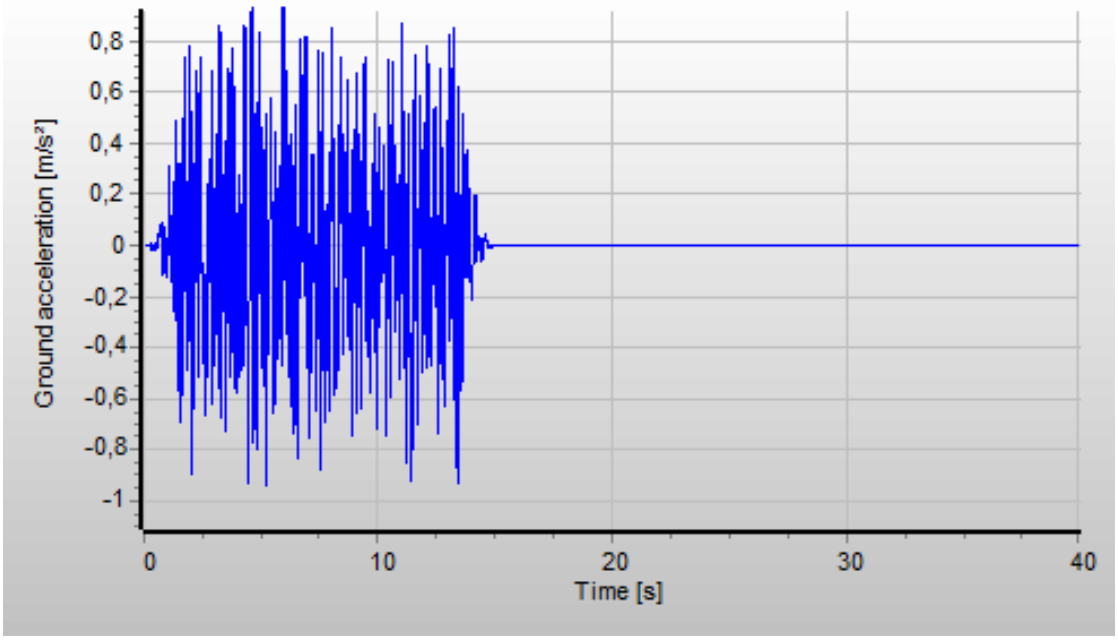

Figure 8.10: Serie 7.

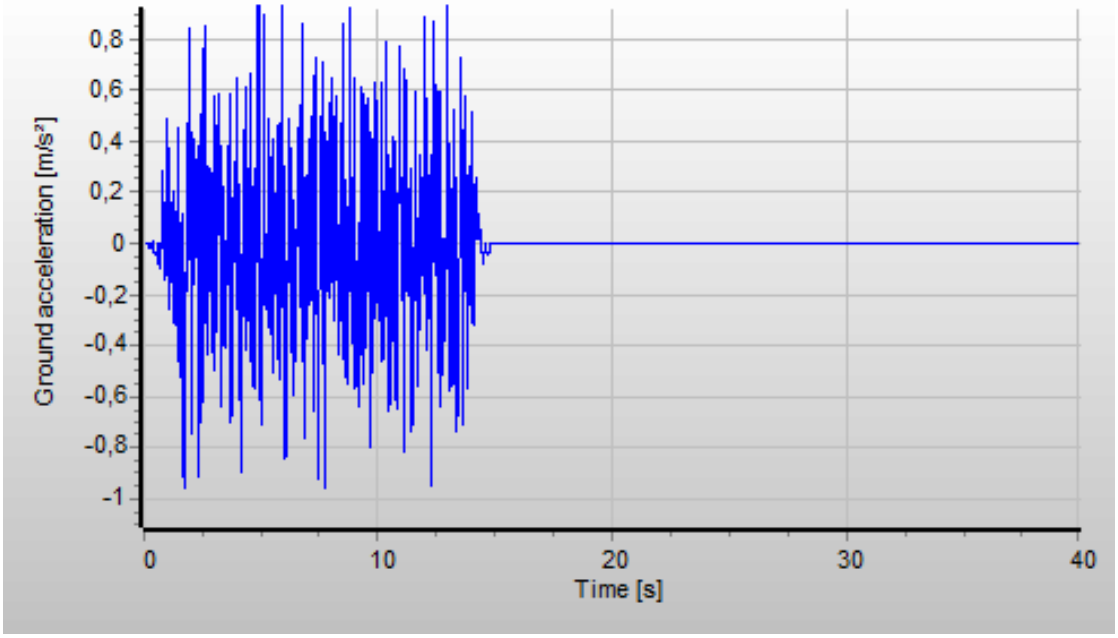

Figure 8.11: Serie 8.

E Set of ground accelerations for the analysis in Sagres

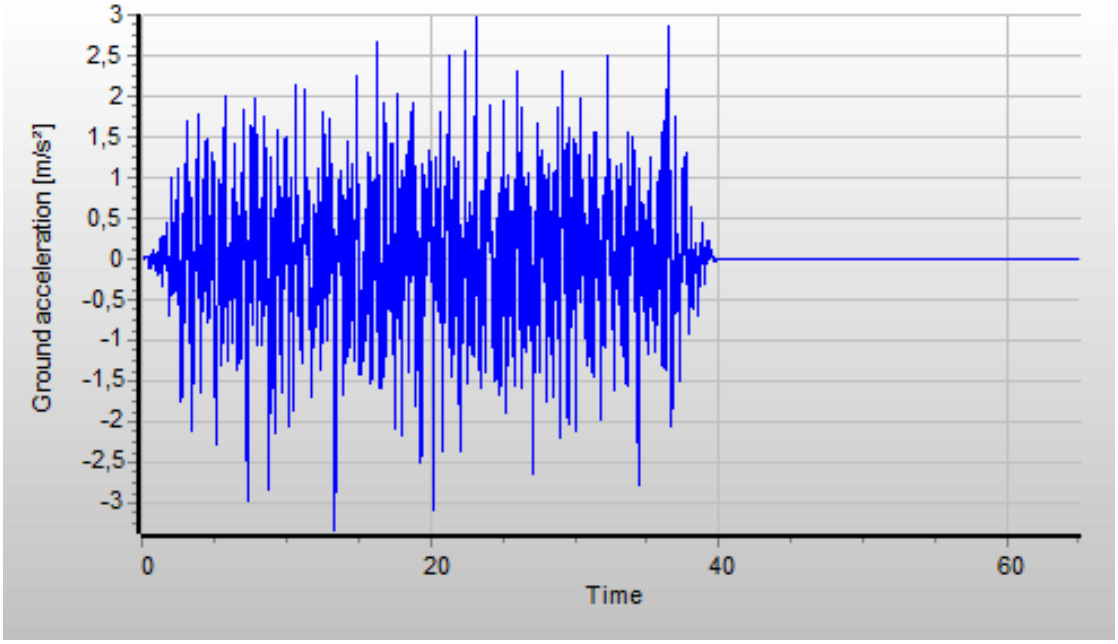

Figure 8.12: Serie 1.

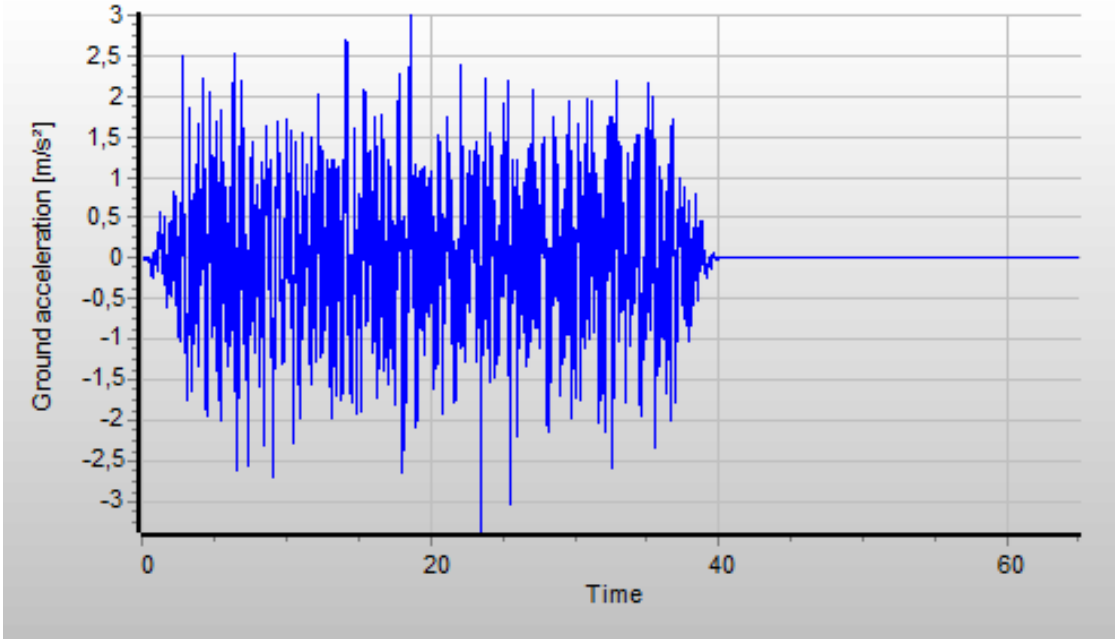

Figure 8.13: Serie 2.

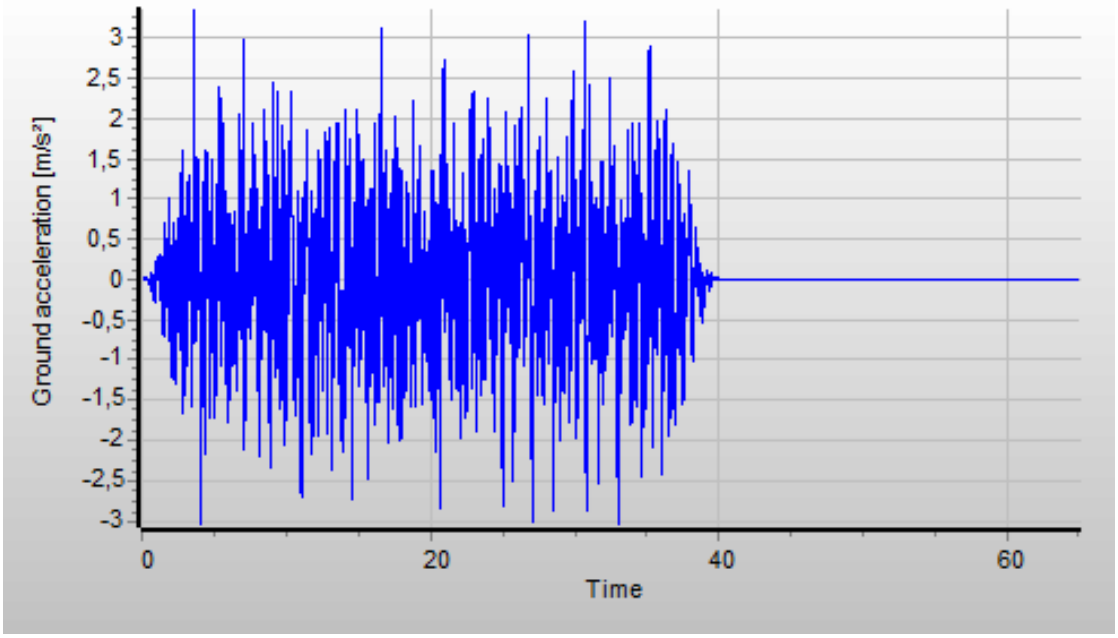

Figure 8.14: Serie 3.

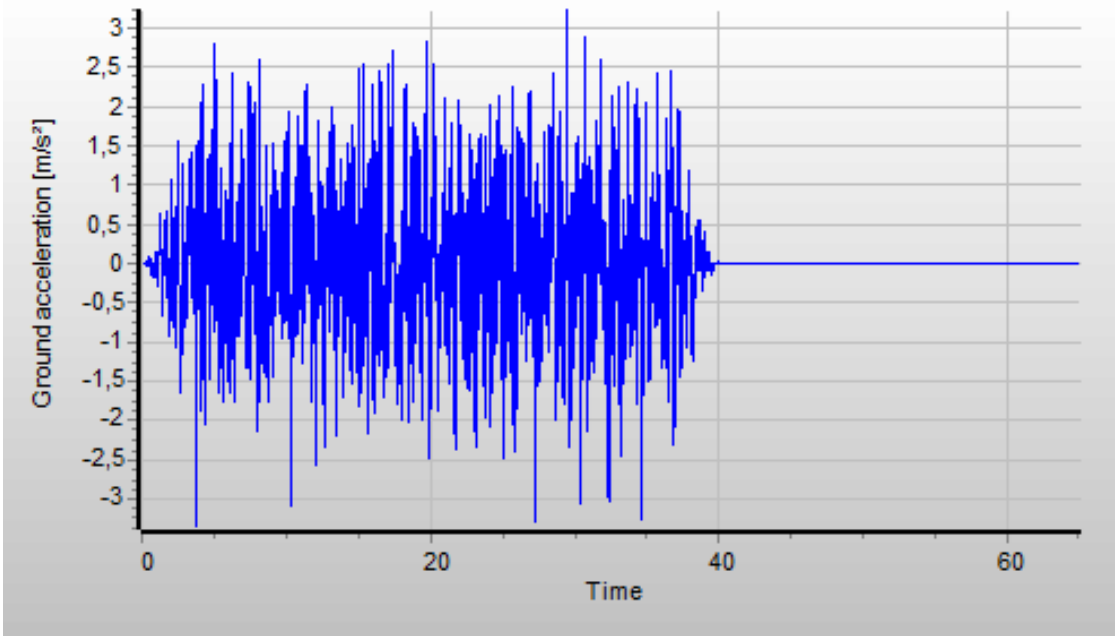

Figure 8.15: Serie 4.

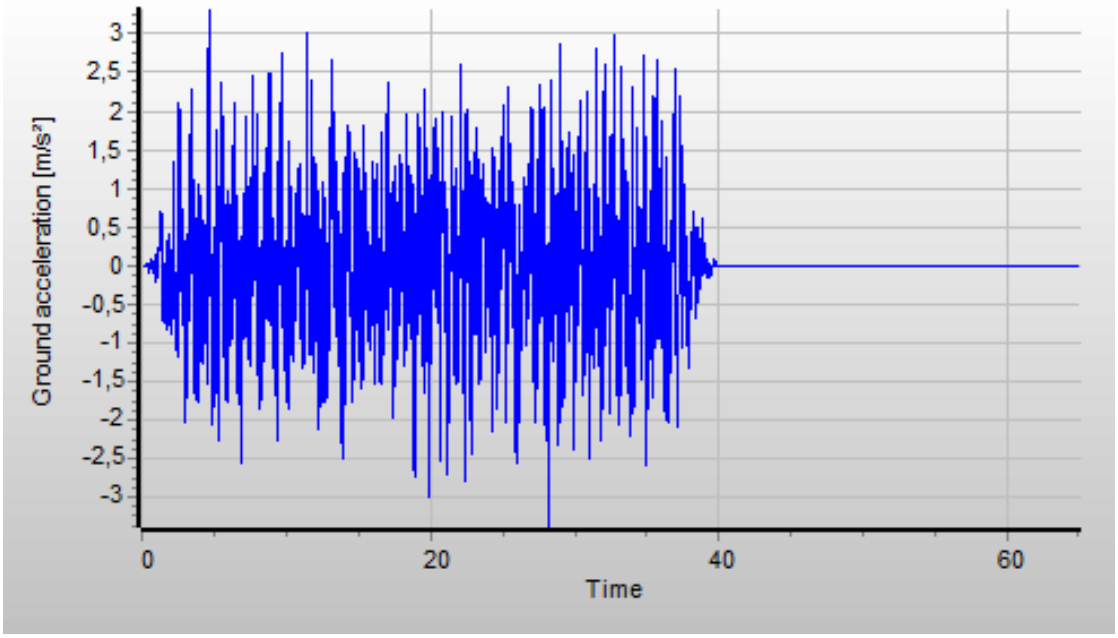

Figure 8.16: Serie 5.

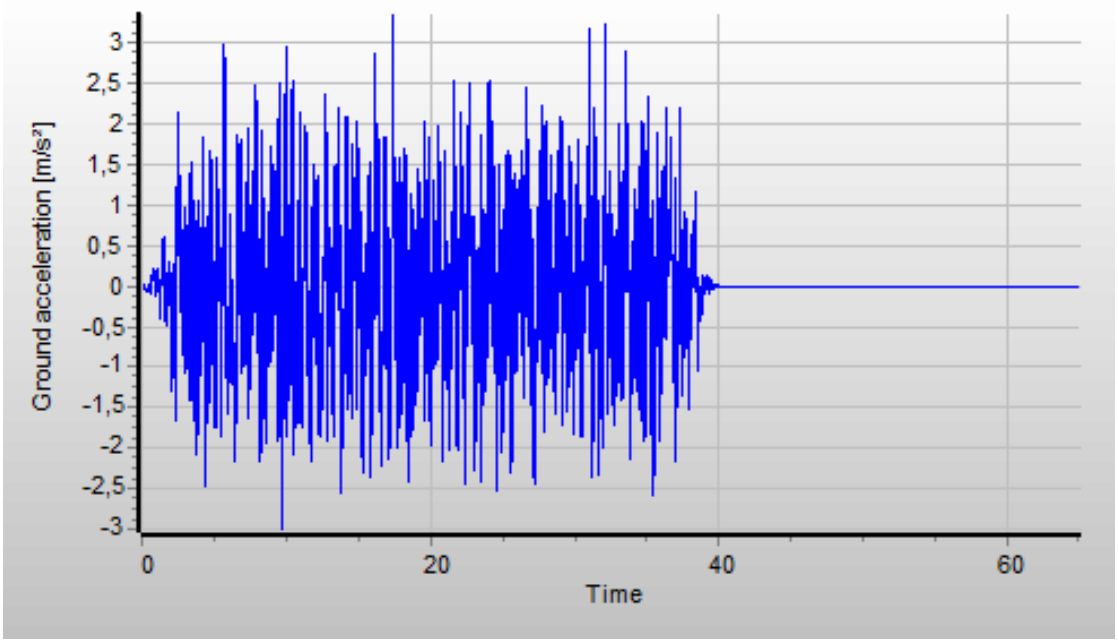

Figure 8.17: Serie 6.

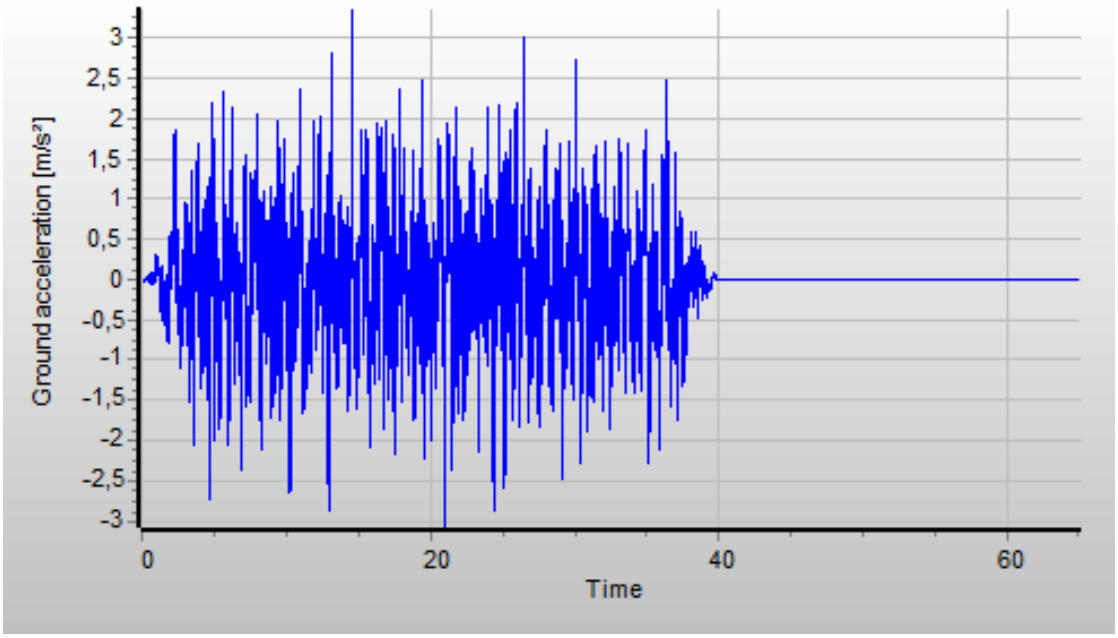

Figure 8.18: Serie 7.

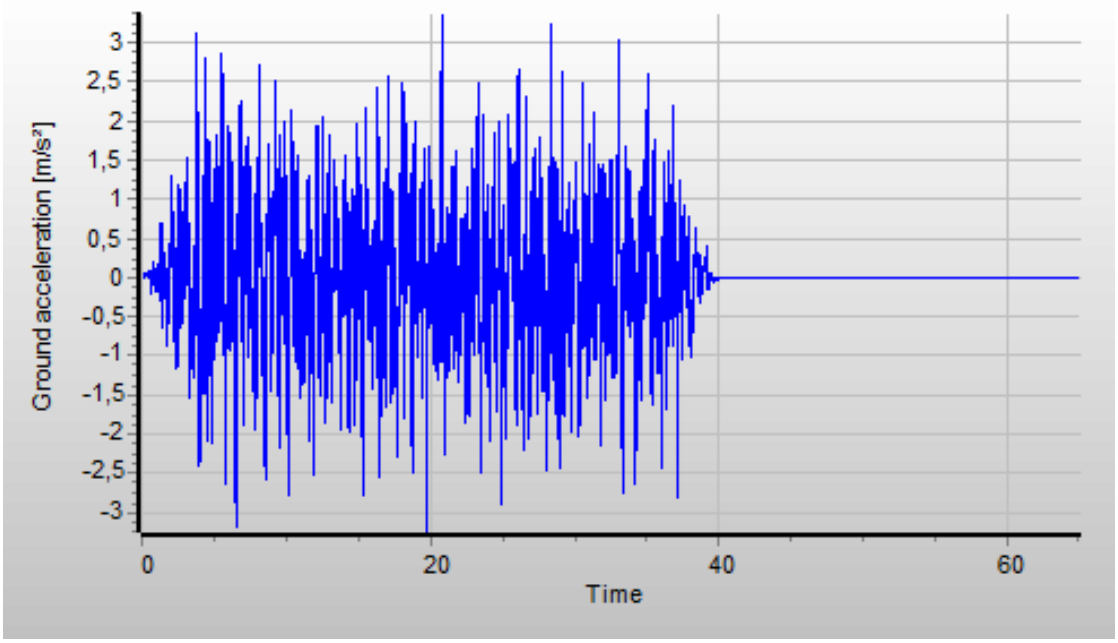

Figure 8.19: Serie 8.

F Mode shapes of Model 4 and Model 6 compared with the experimental results

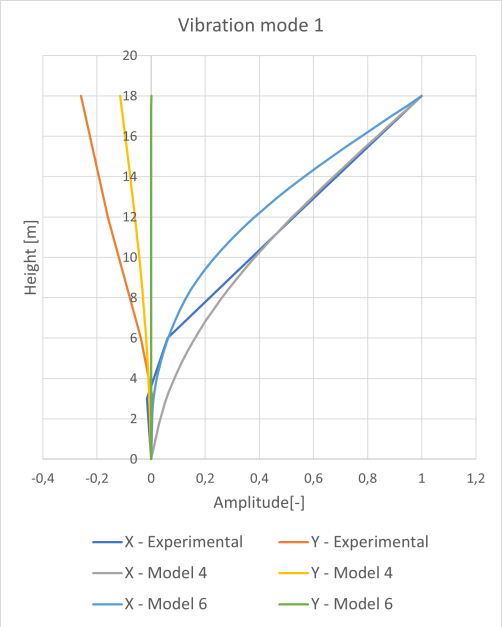

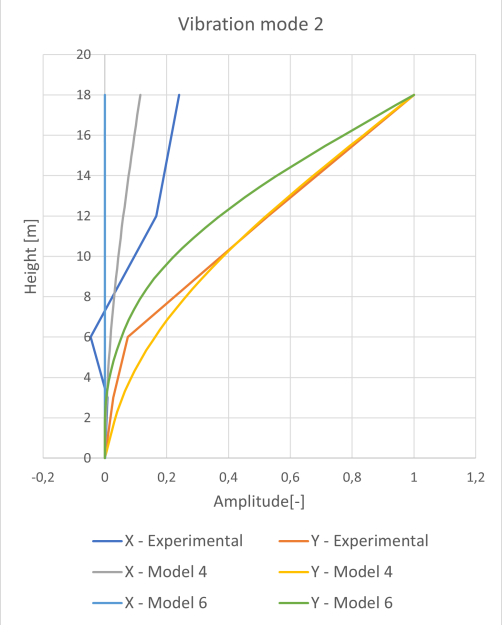

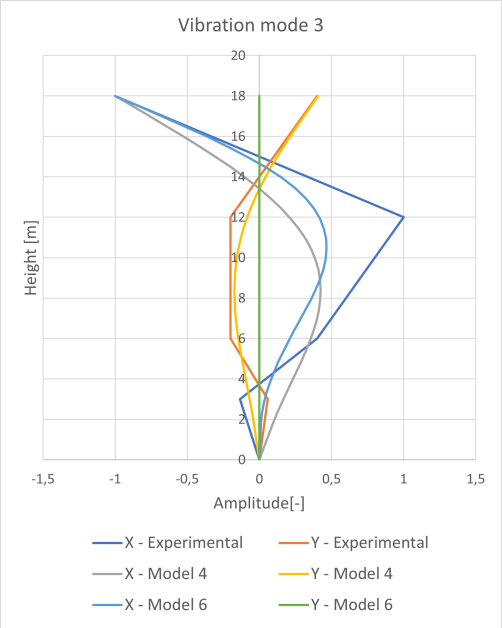
Vibration mode 3
Height [m]
20
18
16
14
12
10
8
6
4
2
0
-1,5
-1
-0,5
0
0,5
1
1,5
Amplitude[-]
X - Experimental
Y - Experimental
X - Model 4
Y - Model 4
X - Model 6
Y - Model 6

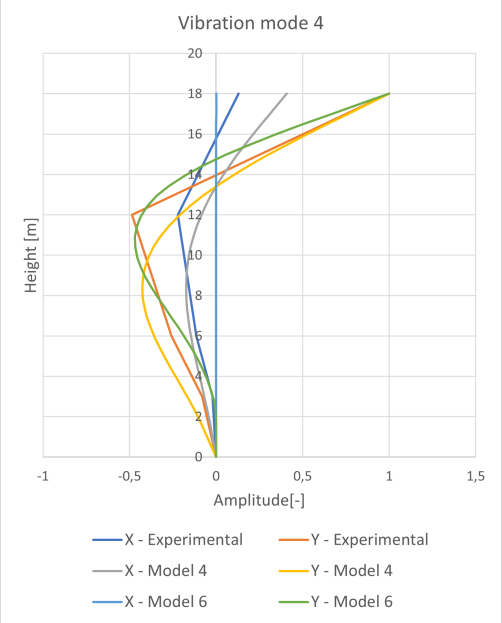
Vibration mode 4
Height [m]
20
18
16
14
12
10
8
6
4
2
0
-1
-0,5
0
0,5
1
1,5
Amplitude[-]
X - Experimental
Y - Experimental
X - Model 4
Y - Model 4
X - Model 6
Y - Model 6

UNIVERSITÉ CATHOLIQUE DE LOUVAIN
École polytechnique de Louvain
Rue Archimède, 1 bte L6.11.01, 1348 Louvain-la-Neuve, Belgique | **www.uclouvain.be/epl**